The Thesis Committee for Matthew Taylor Montgomery
Certifies that this is the approved version of the following thesis:

Development of Fast Pneumatic System for the Study of 14 MeV Fission Product Yields

APPROVED BY
SUPERVISING COMMITTEE:

Supervisor:

Steven Biegalski

Sheldon Landsberger

Development of Fast Pneumatic System for the Study of 14 MeV Fission Product Yields

by

Matthew Taylor Montgomery, B.S.M.E.

THESIS

Presented to the Faculty of the Graduate School of

The University of Texas at Austin

in Partial Fulfillment

of the Requirements

for the Degree of

MASTER OF SCIENCE IN ENGINEERING

The University of Texas at Austin

May 2014

Acknowledgements

I would like to thank Dr. Steve Biegalski for his insight and support on this work, and for believing in me and allowing me to further my education in the Nuclear and Radiation Engineering graduate program here at the University of Texas. His assurances on the experimental portion of my work really got me through—being reminded it's all "six one way or a half dozen the other" is very important when trying to rapidly prototype or find a solution to a problem.

I'd also like to thank Dr. Sheldon Landsberger, who has also been of paramount importance. He introduced me to this project and provided me with a comfortable migration into it—he explained his expectations, and I did everything I could to fulfill them.

Furthermore, I'd like to thank my fellow students—particularly Michael Yoho and Chris Johnson. With Yoho, it was all the long night nights soldering circuits and drilling into concrete walls, thinking up new experiments and ways to improve existing ones. With Chris, it was all the long days, taking every class together and always being there for one another.

Lastly, a big thank you to the amazing staff at the Nuclear Engineering Teaching Laboratory, including Tracy Tipping, Mike Krause, and Larry Welch.

Thank all of you for helping me get here.

Abstract

Development of Fast Pneumatic System for the Study of 14 MeV Fission Product Yields

Matthew Taylor Montgomery, M.S.E.

The University of Texas at Austin, 2014

Supervisor: Steven Biegalski

The use of fission product yield data is pervasive among nuclear calculations, particularly in the realm of nuclear forensics and active interrogation for special nuclear material. The capital source of fission product yield data is the work of T.R. England and B.F. Rider, of Los Alamos National Laboratory, in the early 1990s. Though their work was certainly substantial, a great deal of data was generated computationally, in lieu of done empirically—particularly with low-yield, short-lived progeny. Due to this, relative uncertainties in the measurements can be as high as 64%, and vary wildly from database to database (oft times not even within one standard deviation of one another).

The purpose of this work is to build a pneumatic system capable of cyclic irradiation coupled to a D-T neutron source, in order to cumulate proper counting statistics, by which one can backcalculate independent and cumulative fission yields. Beyond the design and control parameters of the pneumatic system, a precise flux characterization of the facility is presented, and finally, proof-of-concept is demonstrated by causing 14 MeV neutron-induced fission and identifying every observed fission product photopeak.

Table of Contents

List of Tables

List of Figures

Chapter 1: Introduction

MOTIVATION

In every experiment that induces fission, it is of paramount importance to understand what fission products are present post-irradiation. This has implications in nearly all aspects nuclear science: from reactor burnup & operation, spent fuel storage, and radiation safety to nuclear forensics elements such as non-proliferation treaty verification, active interrogation, and many more.

The last major contribution to the field lies in the work of England & Rider of Los Alamos National Laboratory in the mid-90s, which represents the majority of the yield data present in the American Evaluated Nuclear Data File (ENDF) in its current revision (ENDF-B/VII.1) [1][2]. Though the database is extensive, with over 1200 isotopes with independent and cumulative yields identified in several bands of energy, the error on these measurements is extraordinary, with 51% of all cumulative yield data and 75% of all independent yield data for ^{235}U having a relative error greater than 60% [3]. This error propagates, if used as an input anywhere in a calculation, as a linear or compounded error in the output—which presents itself as large unaddressed problem with real consequences in our national nuclear data set.

Furthermore, migrating to another nuclear data set, such as Europe's JEFF or the Japanese JENDL, these yields can differ by an order of magnitude, and their variances oft times do not even overlap each other, within several standard deviations [4][5].

This states a real need for the fission product yield data to be revisited and revised, particularly in a world where nuclear forensics is a growing concern for national security.

FISSION

Fission occurs when a nucleus can better reach stability by shedding a large amount of energy at once and is permitted by the decreasing binding energy of nuclei per nucleon with atomic mass numbers greater than 50; this is largely due to the repulsive force due to Coloumbic interactions overtaking the binding force of the strong nuclear force in larger nuceli [6]. The nucleus sheds this large amount of energy by physically separating into two smaller nuclei, typically asymmetrically at a 1:1.3 atomic mass ratio, as shown in Figure 1.1.

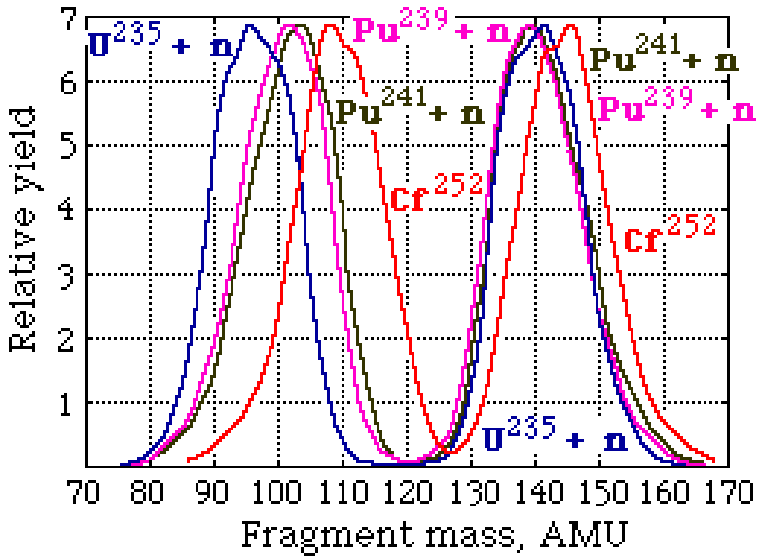

Figure 1.1: A qualitative plot of yield versus atomic mass for several fissile species, demonstrating asymmetric fission (the "double-hump" curve). [7]

Fission can be described as either induced or spontaneous, which is defined by whether or not a specific isotope fissions in the absence of a catalyst, such as an incident neutron. Generally, spontaneous fission is more prevalent in the heavier species, such as ^{252}Cf; this work concentrates on fast neutron-induced fission. To "induce" fission is to supply the nucleus with enough energy that it deforms in such a way to overcome the

attraction between is nucleons, said to be the "critical energy of fission", demonstrated in Figure 1.2 as E_f.

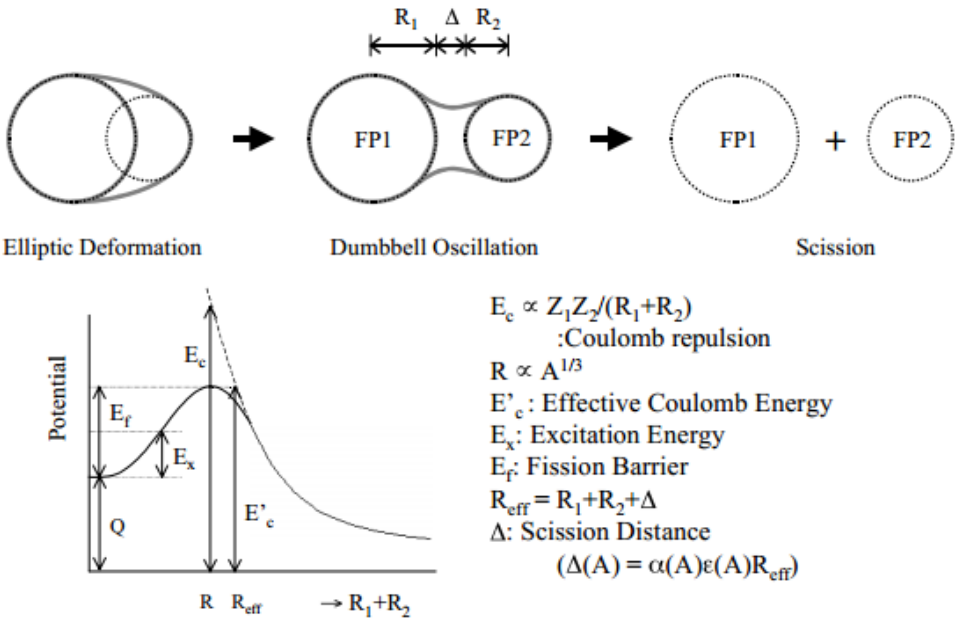

Figure 1.2: A depiction of atomic deformation with changing electric potential. [8]

For example, ^{236}U's critical energy of fission is 5.3 MeV. To demonstrate that ^{235}U is fissile with the addition of a neutron with no additional energy, one would evaluate a Q-value for the reaction:

$$^{235}_{92}U + ^{1}_{0}n \rightarrow ^{236}_{92}U \tag{1.1}$$

$$Q = [M(reactants) - M(products)]c^2 \tag{1.2}$$

$$Q = (235.04392 + 1.008665 - 236.04556)amu * 931.494\frac{MeV}{amu}$$

$$Q = 6.544\ MeV$$

Since Q, 6.544 MeV, is greater than the critical energy of fission, 5.3 MeV, ^{235}U is a fissile species that needs only the introduction of a neutron with no additional energy to fission.

Fission yields are quantities that describe the fractional abundance of a particular isotope after a fission event, expressed as either "independent" or "cumulative" [9]. An independent fission yield is the probability that a radionuclide will appear as the immediate product of a fission event, while a cumulative fission yield is the probability that a radionuclide will appear at some point after a fission event as a fission product progeny. Hence, a given cumulative yield for a radionuclide is representative as the sum of the full decay chain's independent yields leading to that radionuclide.

D-T NEUTRON GENERATOR

Figure 1.3: The commercially-available Thermo MP320 neutron source. [10]

Neutrons may be produced in many ways. Isotopic sources provide a continuous flux by either utilizing an alpha-emitter coupled with an isotope with a large (α,n) cross-section (such as AmBe, PuBe, or RaBe sources), or alternatively using a spontaneous fission source, such as ^{252}Cf. Though the flux is continuous, it is generally below the threshold to see many activation reactions. Furthermore, these sources present unique obstacles in terms of shielding, given they can be never be "turned off", nor can they be pulsed.

The most common form of "neutron generator" creates deuterium ions and accelerates them into a tritium target. This "neutron generator", such as the Thermo MP320 shown in Figure 1.3 and used at the University of Texas, utilizes the "D-T" reaction, as:

$$ {}_1^2D + {}_1^3D \rightarrow {}_2^4He + {}_0^1n \tag{1.3} $$

$$ Q = (2.0141018 + 3.0160493 - 4.002603254 - 1.008665)\ amu * 931.494\ \frac{MeV}{amu} $$

$$ Q = 17.5893\ MeV $$

The neutron then carries, by kinematics, 14 MeV of the Q-value, and the alpha particle carries the remaining 3.6 MeV.

D-D interactions in the source are minimized, as this would require the ionized gas of deuterium to interact with itself, which is highly improbable—furthermore, the neutron yield for the D-T reaction is 100 times higher at the source's standard operating conditions, and D-D neutrons are emitted with a forward bias, along the axis of the beam (which conflicts with the geometry of the fast pneumatic system design). Hence, interactions from 2.5 MeV D-D neutrons are negligible.

The neutron generator itself is a sealed tube neutron source containing an ion source, ion optics, and an accelerator target, shown in Figure 1.4 [11]. This tube is then placed in the "accelerator head", a metal housing filled with dielectric media to shield the high voltage elements within from the surroundings.

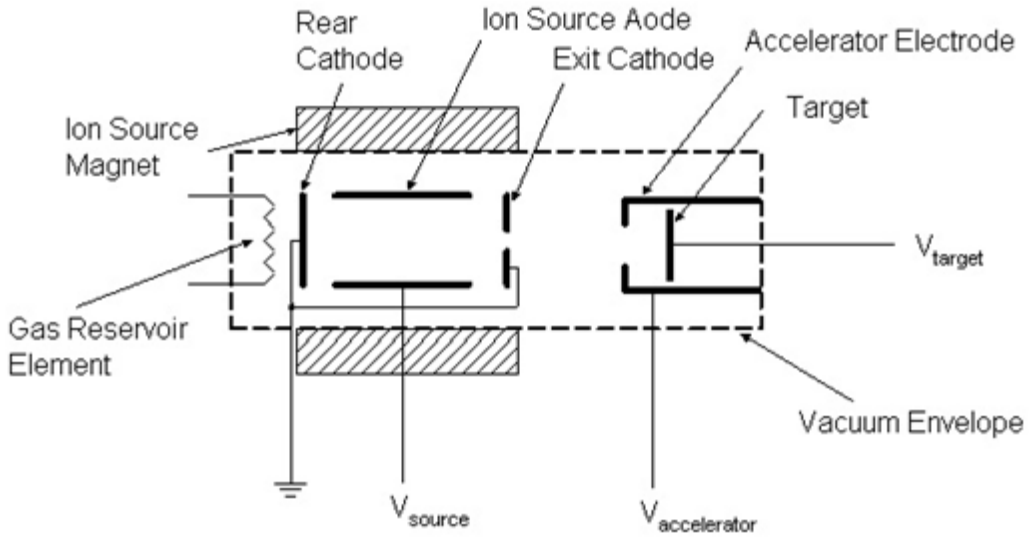

Figure 1.4: A schematic of a general neutron tube source. [12]

Essentially, the neutron source generates deuterium gas by heating the gas reservoir element. Heating and cooling this element changes deuterium gas pressure in the vacuum tube. The tube then utilizes a Penning ion source—a mesh of crossed electric (generated by V_{source} in Figure 1.4) and magnetic fields from a permanent magnet ("ion source magnet" in Figure 1.4). A plasma is formed that then ionizes the gas, which is then accelerated towards the target by utilizing a bias difference between the exit cathode and the accelerator electrode. The target is a thin titanium hydride with a high purity of tritium, allowing for the D-T reaction.

PNEUMATIC SYSTEM

It should be mentioned that the mechanical components utilized to establish the Fast Pneumatic Cyclic Irradiation Facility at NETL were designed by a team of undergraduate mechanical engineering students headed by Dr. Sheldon Landsberger as their final component necessary to complete their degree. The students – Kendall Burns, Janet Fuchs, Jason Guidry, and Michael Yoho – have their work summed up in the document "Automatic Transfer System for Neutron Irradiation Test Bed" as part of the Mechanical Engineering Design Projects Program at the University of Texas at Austin [13]. This document presents the reasons why they pursued the design of the diverter and sample loader cast against competing alternatives; attached in the appendix the reader will find mechanical drawings for these components taken from this paper.

AIM OF WORK

The aim of this work can be described succinctly: to build and describe an apparatus by which experimenters can improve fast fission product yield data and to conduct neutron activation analysis in a controlled, automated, cyclic manner using a 14 MeV D-T neutron source. After designing and building the apparatus, one must verify the integrity of the 14 MeV flux at the sample annulus. Lastly, the project would be complete with fission product identification being demonstrated using the apparatus.

Chapter 2: Fast Pneumatic Cyclic Irradiation Facility

DESCRIPTION OF OPERATION

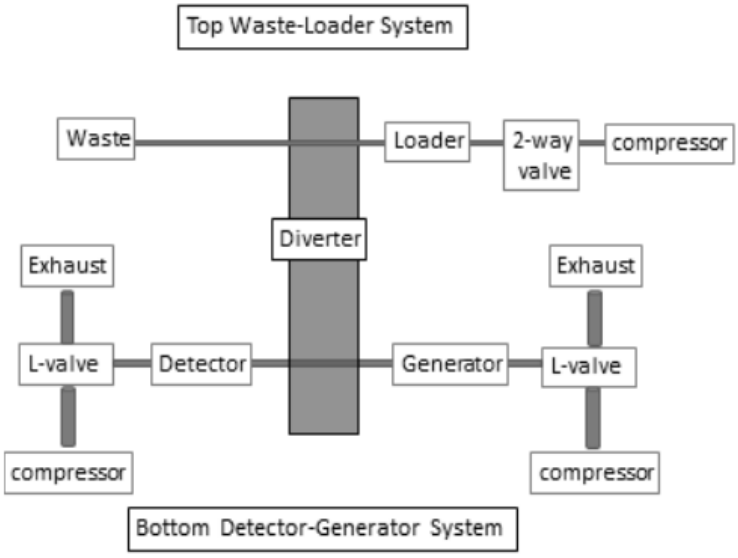

Figure 2.1: A schematic representation of the integration of the components of the fast pneumatic system. [13]

The fast pneumatic cyclic irradiation facility at the University of Texas at Austin allows a user to load a sample in the form of a 'rabbit' vial at a safe operating position, actuate a linear valve to move the sample to a 'diverter', which can be moved vertically to allow the user to have an obstructed or unobstructed pathway. Once the sample has been moved to an unobstructed pathway between irradiation & detection, the sample can be automatically cycled between the two with hardware-trigged acquisition. Once cycles have been completed, the sample can be placed back at the diverter, which can be raised to the "obstructed" pathway between waste and loading, and fired to waste. A second sample may then be loaded and the procedure may begin again. The integration of these individual components in summed up in Figure 2.1.

SAMPLE LOADER

The sample loader is essentially a 'hopper' which contains up to twenty *rabbit* vials in an aluminum enclosure. The base of the enclosure is actually a machined piece sitting on the driveshaft of a stepper motor (Animatics Corporation SM17205D), which may be rotated using a serial signal from the control computer [14]. An exploded view of the device is presented in Figure 2.2, and the permanently mounted sample loader is shown in Figure 2.3. Once rotated, a single sample is loaded in the sample tube below the stepper motor, which is connected to a pneumatic line that may be pressurized, pushing the sample up and over the 20' tall by 3' thick concrete wall between the user and the neutron generator.

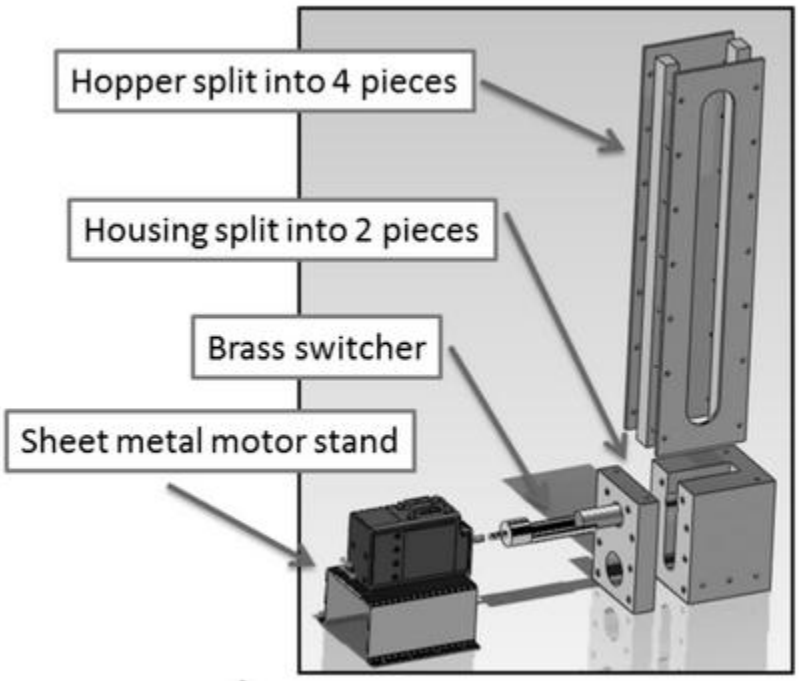

Figure 2.2: The initial design of the sample loader. [13]

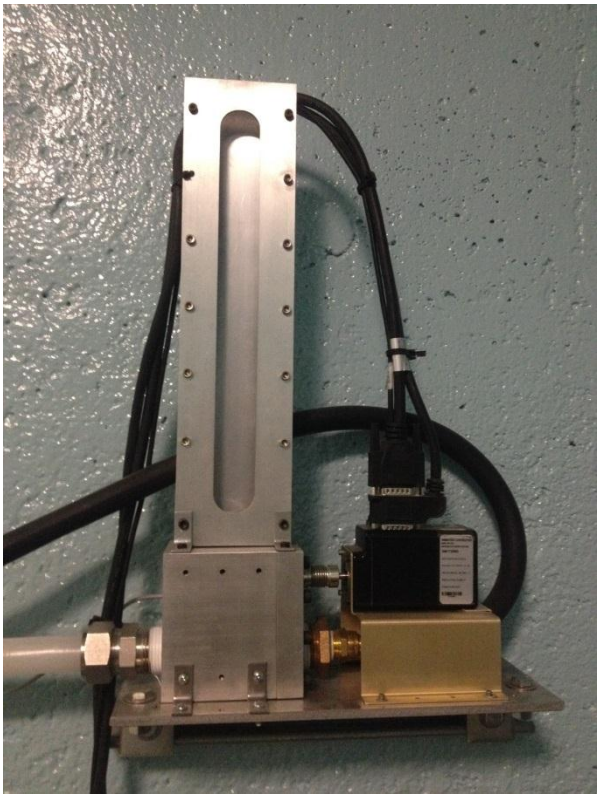

Figure 2.3: The permanent mounted sample loader.

The motor driveshaft may be rotated manually by sending the serial signal "\81EIGN(2)\s\81EIGN(3)\s\81ZS\s\81ADT=42\s\81VT=16000\s\81PRT=-4000\s\81G\s" to the stepper motor, or alternatively, using "load a sample.vi", which is a modified form of the LabView standard "basic_serial_write_and_read.vi" example VI to use the above command [15]. Though the stepper motor is serial-controlled, a serial-to-USB converter is used to drive it with the host computer, which has no serial port and instead emulates one as "COMM3".

DIVERTER

The diverter is a large aluminum assembly consisting of a piston-cylinder arrangement driven by a Parker ETH032M10 electric actuator and an Animatics SM23165DT-BRK motor, shown as designed in Figure 2.4 and as mounted in Figure 2.5 [16][17]. This is the transport hub of the fast pneumatic system, as the 'piston' has two channels in it; the top channel is obstructed, but allows air movement (allowing the sample to 'stop'), while the bottom channel is unobstructed (allowing the sample to move freely).

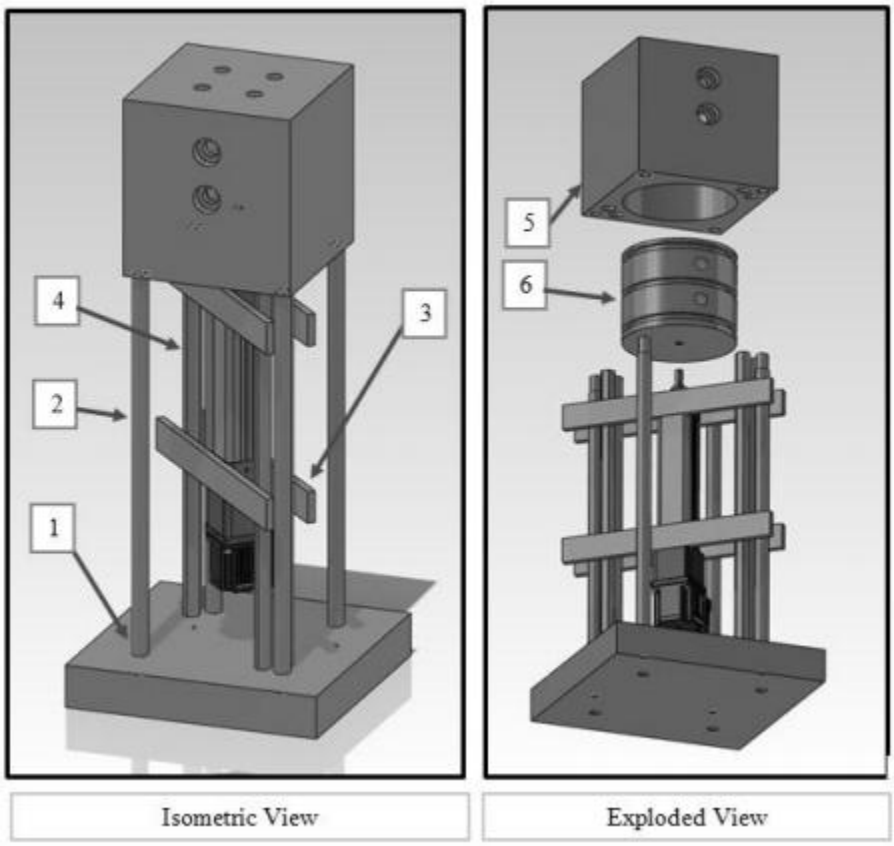

Figure 2.4: The design of the diverter. Labeled: 1: the structural base; 2: support rails for the 'cylinder'; 3: transverse guiderails for the 'piston'; 4: support rails for the 'piston'; 5: the 'cylinder'; 6: the 'piston'. [13]

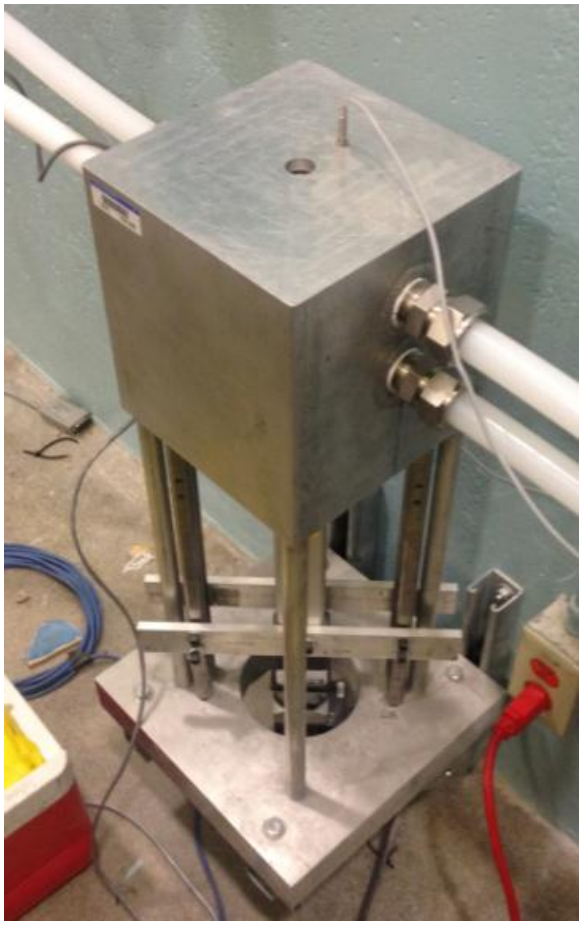

Figure 2.5: The mounted, permanent diverter.

Maintenance of the diverter should include annual lubrication of the piston O-ring, which can be done by disassembling the gearbox from the cylinder and pushing the cylinder out using a dowel pressed into the cavity at the top of the diverter. Like the stepper motor, the diverter is controlled via serial commands, which are emulated via USB on the host computer. To lower the diverter, you may send the command "\82EIGN(2)\s\82EIGN(3)\s\82ZS\s\82ADT=100\s\82VT=22000000\s\82PRT=-230000\s\82G\s"; alternatively, to raise the diverter, you may send the command

"\82EIGN(2)\s\82EIGN(3)\s\82ZS\s\82ADT=100\s\82VT=22000000\s\82PRT=230000\s\82G\s". Note the difference in the two commands: the negative sign preceding the "PRT" in the lower command and it not existing in the raise command. This implies that the diverter's gearbox has no memory of where it is at any given time, and simply translates up and down a given amount. For this reason, if you're unsure of the position of the diverter, never arbitrarily raise or lower it—you could possibly damage it, or commit to re-aligning it manually. The "diverter" sensor will be illuminated in the LabView GUI if it is in the up position—do not attempt to raise it. If the "diverter" sensor is not illuminated and the electronics control box has power, assume it is in the lower position.

SENSORS

There are six total sensors in use with the system, five of which are mounted directly to the sample transfer tube. They are all AutomationDirect diffuse photoelectric sensors, 5mm in diameter, PNP type, with 50mm of sensing distance (model C5D-AP-1A) [18]. They are capable of a switching frequency of 250 Hz, which makes them ideal for a sample transfer of approximately 10-15 ft per second.

The locations of the sensors are: at the sample loading terminal to verify a sample has been dropped into the transfer tube; the 'wall' sensor to ensure it has made it over the wall to the diverter; mounted to the top of the diverter, to report if the piston is in the "up" position; located at both ends of the irradiation cycle (at the detector and at the neutron generator); and finally, at the waste line to ensure the sample was properly evacuated from the fast pneumatic system.

The sensors are mounted to the sample travel lines with a "clamp" jig; essentially, a 6-7mm hole in drilled into the sample tube, and two mating faces surround the sample

line and are held together with four hex head cap screws. One side of the clamp has a threaded hole where the sensor can be placed, threaded until it is in such a position to not hinder sample travel but detect it reliably. As the sample passes in front of a sensor, the location indicator will illuminate on the control panel.

PNEUMATIC MANIFOLD & VALVES

Figure 2.6: The manifold and valve assembly. The major components pictured are the three valves (left, top, and center), a dial pressure gauge (right), and a manual emergency cut-off valve (bottom right).

The three valves are all Banjo model EV3100s, two of which (seen left in Figure 2.5) are operated as L-valves, while the third (seen top right in Figure 2.5) is operated as a linear valve [19]. Their operation is best described schematically in Figure 2.7.

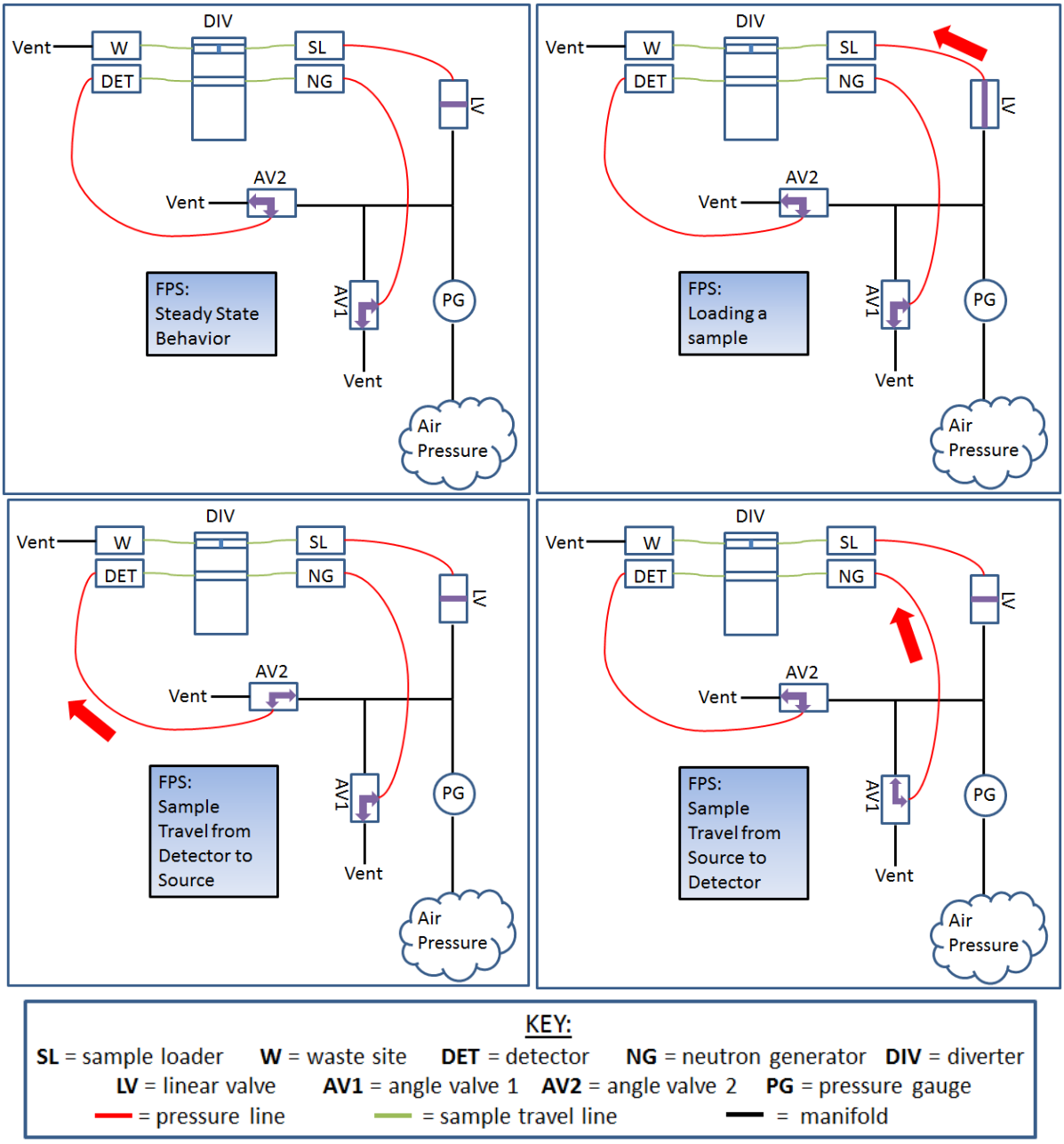

Figure 2.7: The four basic valve positions used to control the fast pneumatic system.

The steady-state operation (the top-left pane of Figure 2.6) has the manifold pressurized (based on the pressure rating of the pressure gauge, “PG”, as well as the emergency manual valve being closed). All three valves are in an unenergized state and all pressure lines are vented to atmosphere.

After loading a sample (top-right pane of Figure 2.6), the linear valve (“LV”) is opened, flooding the pressure line behind the sample loader (“SL”) while the far side, at the waste site (“W”), is vented to atmosphere. The sample vial will accordingly transfer from the sample loader to the obstructed top channel of the diverter (“DIV”).

At this point, the diverter will move downward, and the user will open angle valve 2 (“AV2”), which floods the detector (“DET”) pressure line while the neutron generator (“NG”) is vented to atmosphere. This translates the sample from the diverter to the neutron generator. Then, the diverter is raised, to allow a clear path between detector & irradiator.

The sample may now be moved cyclically between the detector and irradiation site by energized the two angle valves, as depicted in the bottom two panes of Figure 2.6.

WIRING AND ELECTRONICS

The wiring and electronics necessary to integrate the valves and sensors to LabView required intermediate circuitry, which was coupled into a panel box mounted adjacent to the manifold system.

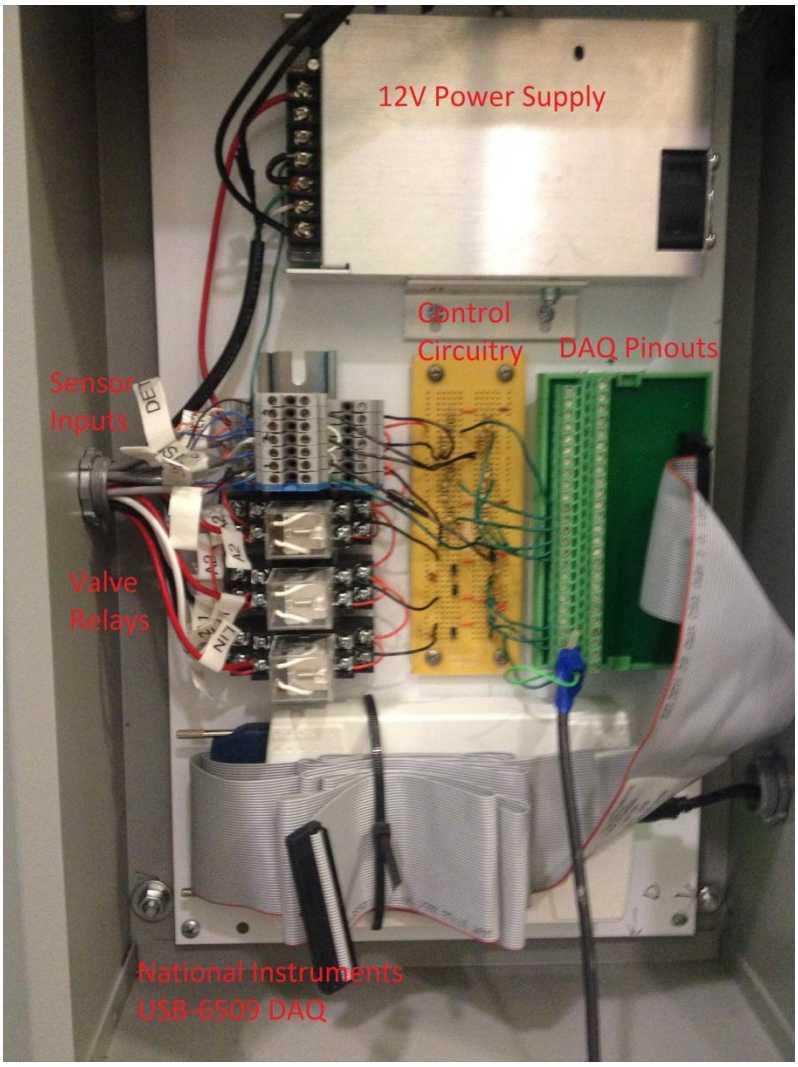

Figure 2.8: The electronic circuitry within the panel box necessary to control the fast pneumatic system.

The box's contents, shown in Figure 2.8, include a 12V power supply (top), a rail supporting the sensor wiring and three relays (left), the relevant relay-transistor and voltage divider circuits (middle), the LabView DAQ pinouts (right), and the LabView DAQ itself (bottom). A more complete wiring schematic is shown in Figure 2.9.

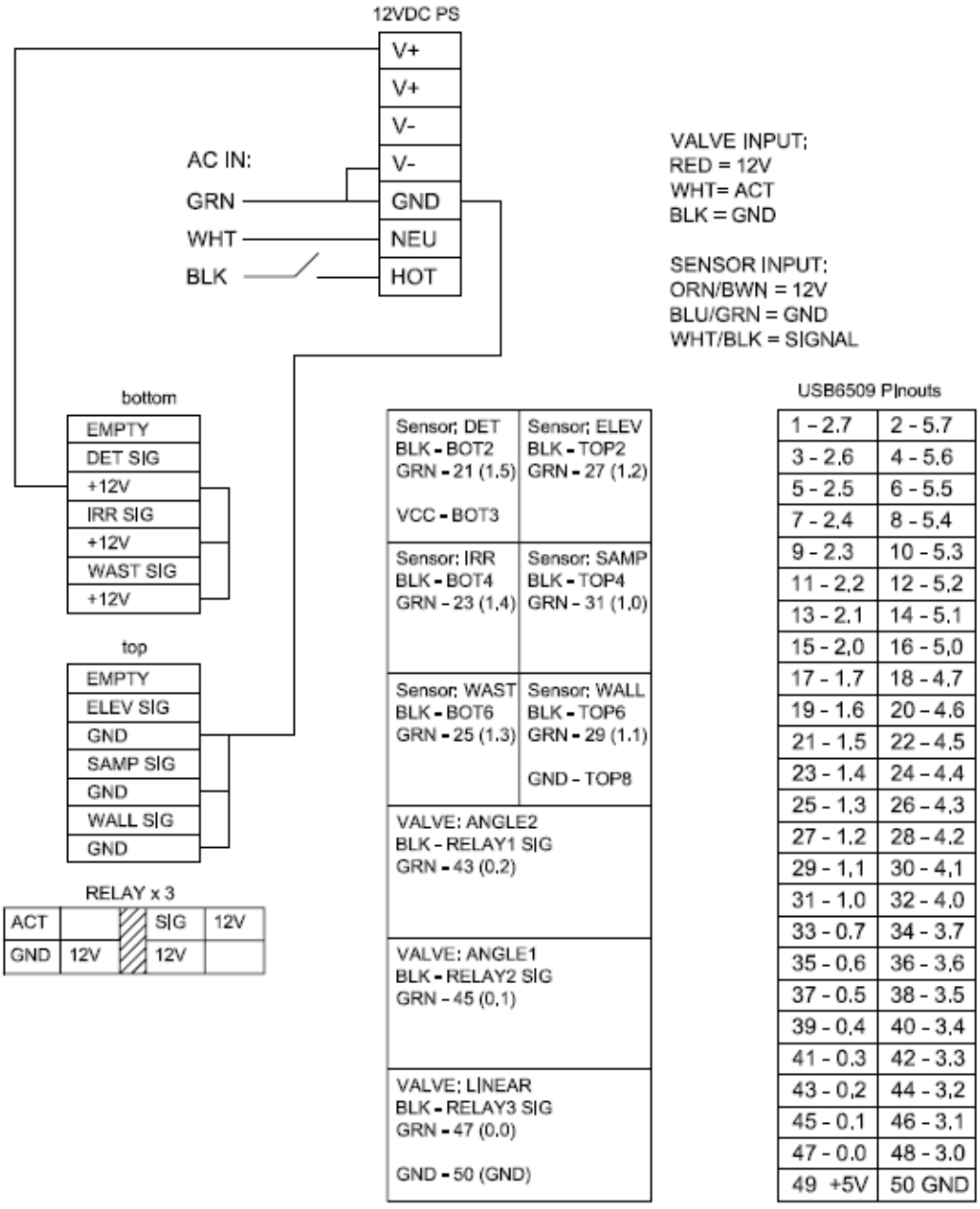

Figure 2.9: A wiring schematic detailing the wiring of the panel box, laid out analogous to the actual positions of the components (power supply at top, sensor & relay rail at left, circuitry middle, DAQ pinouts right).

Voltage dividers were required for use with the sensors, given that the operating voltage for the model of sensor used was 10 – 30VDC, while the operating current needed to be stepped down to less than 100 mA, and the signal needed to be provided to the LabView DAQ, which is a TTL device (5V). 150Ω and 47Ω resistors were readily available, which stepped the current down to approximately 60 mA, and passed 2.9V to the DAQ (which reads as a logical true). This voltage divider, with the proper wiring from the sensor outputs, is described in Figure 2.10, below.

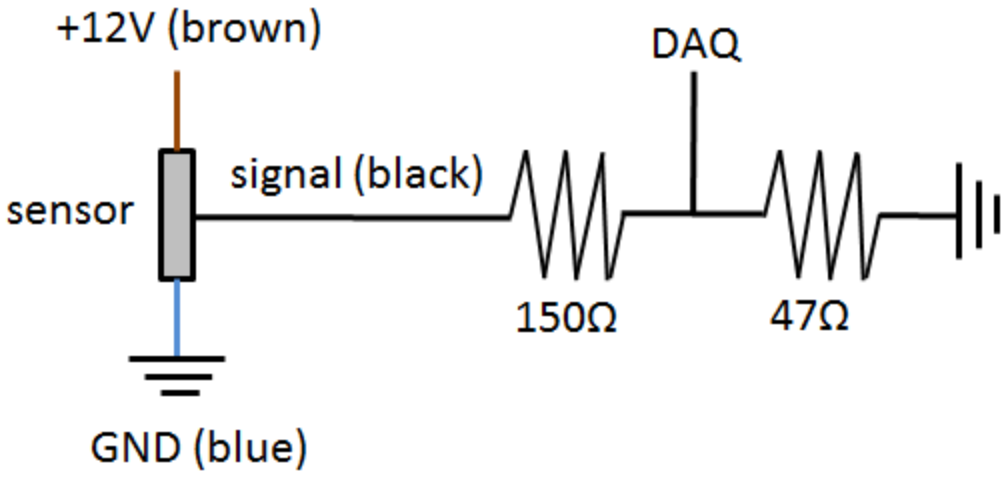

Figure 2.10: Voltage divider used to step both the current and voltage down to ensure safe operation of the sensor and to pass the signal to the LabView DAQ. Six of these circuits are used in the middle board in the panel box, for each sensor, and mapped to individual pinouts on the LabView DAQ.

The valves differ and are slightly more difficult electronically than the sensors, given they are transistor-relay circuits. Given we want to control a relatively high voltage device (the valve) with a low voltage, low current device (the DAQ), we must have an intermediate relay to trigger a connection between the power supply and the valve. The relays themselves are NTE Electronics R14-11D10-12 DC-operated DPDT with an internal resistance of 160 ohms, meaning they have a saturation current to pull the coil in of 75 mA [20]. The 2N2222A resistor has a DC current gain minimum of 75, meaning we need ~ 1 mA from the DAQ. To ensure it completely saturates, a 3.3 kΩ resistor was used, to pass 1.5 mA. This circuit is modeled in Figure 2.11, below.

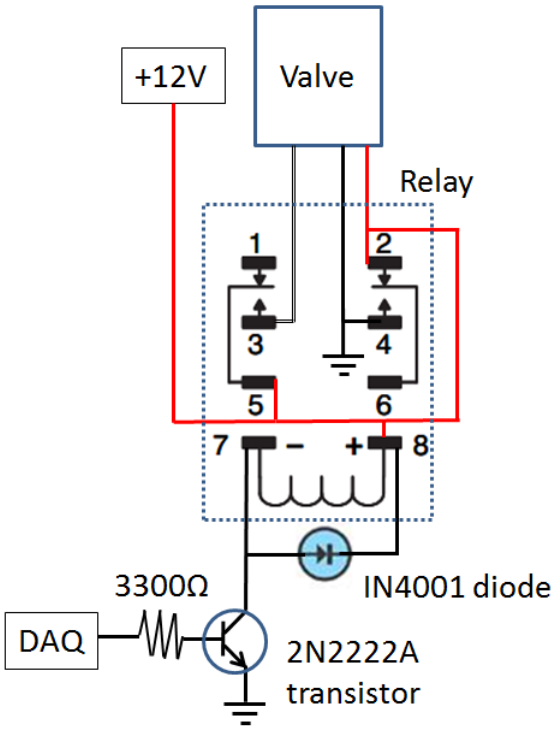

Figure 2.11: The NPN transistor-relay driver circuit used to drive a valve. Three of these circuits are incorporated onto the middle board in the panel box.

DETECTOR INTEGRATION

Figure 2.12: The detector system, a portable Ortec HPGe SMART detector coupled to a custom-made DSPEC Pro.

The detector used with the fast pneumatic system is an Ortec HPGe SMART detector, alongside a custom-made DSPEC Pro altered such that it may properly gate a quickly varying 5V TTL signal, as seen in Figure 2.12 [21].

Originally, the detector was to be run in the same room as the 100% duty cycle neutron generator. Shielding the detector properly from the 14 MeV neutrons, as well as the prompt and delayed activation gamma, while managing a one second travel time proved difficult, and ultimately, the detector was moved to sit near the user, with six feet of concrete between the detector and source to minimize background. Prior to this, however, steps were taken to keep the detector proximate to the source, and eliminate

prompt background in the signal using the detector's pulsed mode (operating at 50% duty cycle) and a T-flip-flop circuit. The circuit that would accomplish this is shown in Figure 2.13, below.

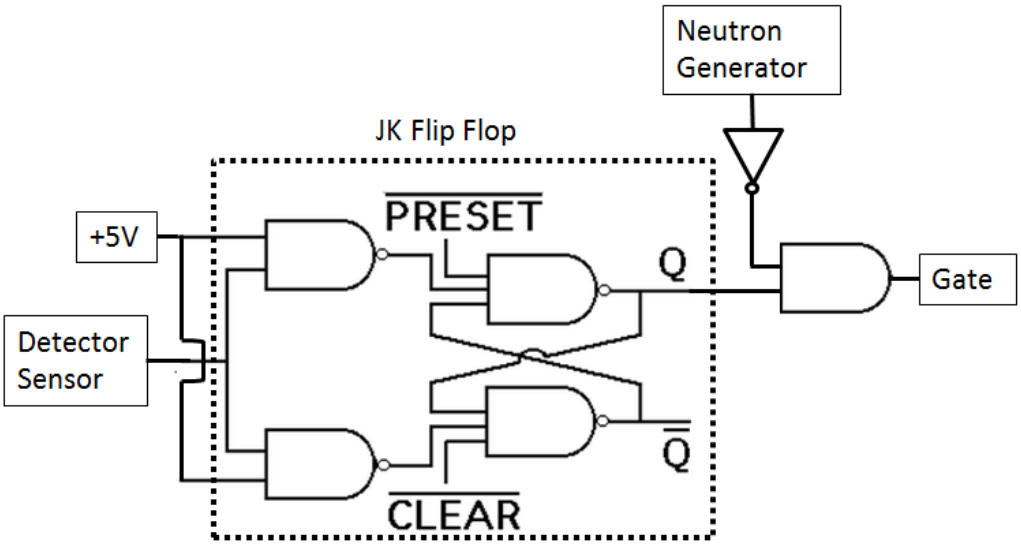

Figure 2.13: Integrated circuit diagram that allows for the reduction of prompt gamma signal when operating in pulsed mode.

A JK flip flop, when both J & K are permanently tied to a logical high as shown in Figure 2.13, swaps the value of Q & Qbar when the clock signal encounters a falling edge [22]. In Figure 2.13, the clock has been replaced with the detector sensor—hence, when the sample is passed in front of the detector sensor, a hardware-timed value flags a logical high, and when the sample passes in front of again (leaving the detector), the value is now flagged a logical low. The function of PRESET and CLEAR allow the user to manually set the condition of the toggle (to state if the sample is present or not, such that it toggles correctly). An AND gate takes the logical sum of the output of the T flip flop (whether or not the sample is present), and the negation of the neutron generator

signal (in pulsed mode, this would flag true if the neutron generator was off), hence passing a TTL signal of true when the sample is present and the neutron generator is off.

This hardware can be made with three low-power Schottky DIP TTL ICs (7476, 7404, and 7408), prototyped in Figure 2.14, below [23][24][25].

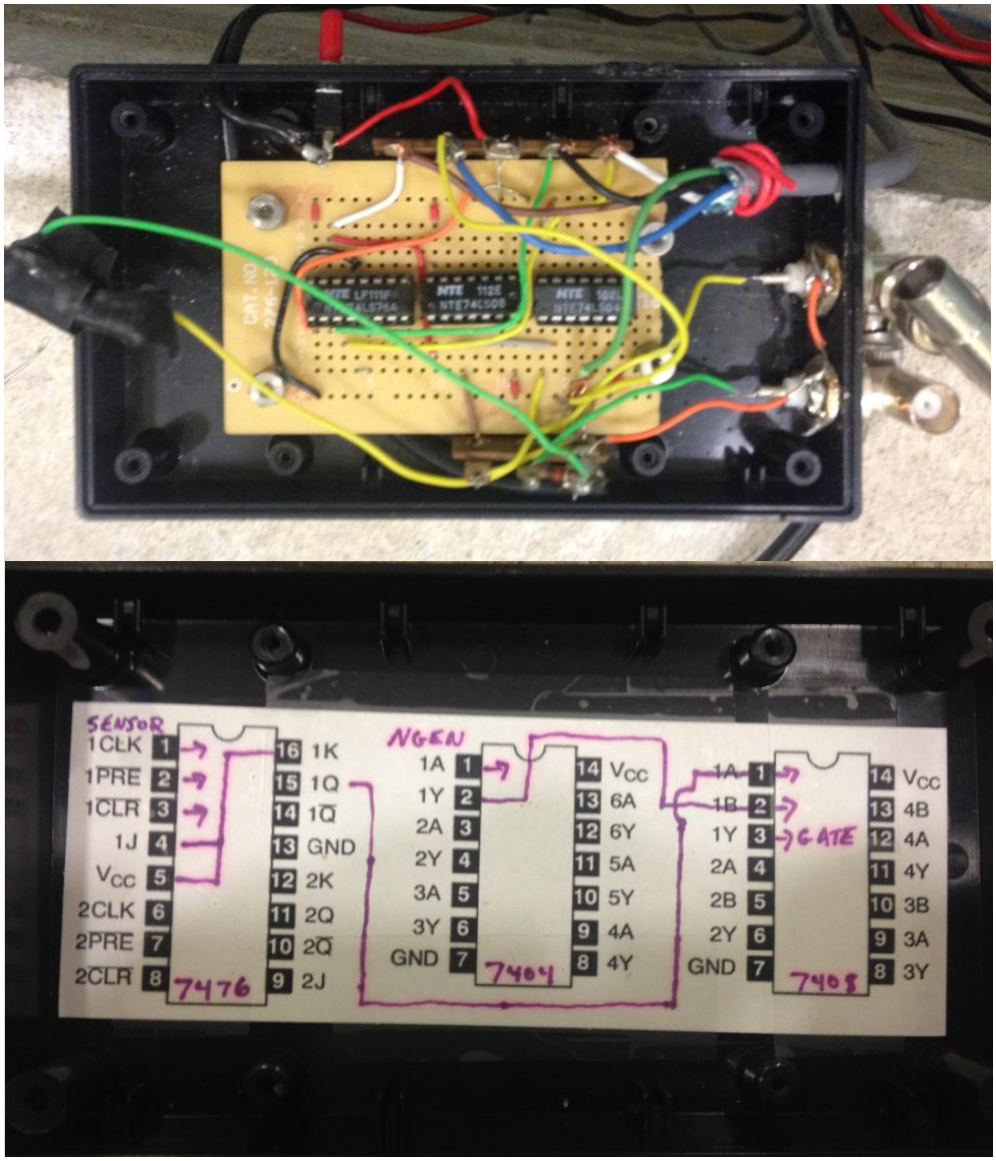

Figure 2.14: Prototype circuit allowing for the reduction of prompt gamma signal.

As aforementioned, the DSPEC Pro is custom-made such that the “READY IN” signal on the back is no longer utilized as a sample changer, but instead, now bins data to one channel if “READY IN” sees a logical high and bins to a separate channel if “READY IN” sees a logical low. This would thereby be connected to the “GATE” of the preceding circuit.

Figure 2.15: DSPEC Pro being gated using a standard RG-56 coaxial cable from the prompt gamma reduction prototype circuit.

Operating the neutron generator at 50% duty cycle with an extension of 1 microsecond allowed for a drastic reduction of the prompt gamma signal using this technique, but the delayed gamma signal – the neutron activation of the material in the room, as well as the shielding and detector itself-- was dwarfing the signal otherwise, and

the decision was made to relocate the detector. In relocating the detector, the gate was still used to trigger the acquisition to the proper channel, but done through LabView in lieu of the prototype circuit. The LabView acquisition is done in the same way a valve is fired: a 5V TTL signal is 'written' to a channel's register in a certain pin as described by Figure 2.8. In the case of a valve, the 5V TTL signal is written for approximately two seconds (the time it takes to push the sample between two points in the system, with a factor of safety to ensure it arrives); in the case of the detector, the 5V signal is written to a channel's register in a certain pin if the detector sensor has been flagged high and the current register of the pin is low (to indicate the sample wasn't previously at the detector, and is now); otherwise, the 5V signal on the pin is cleared (to indicate the sample has left the detector for irradiation).

CONTROLS

With the mechanical components and electronics well-described, the last major element that needs to be emphasized is what's happening under the hood in LabView to make the system functional [26]. To that end, change detection (the operation by which the sensor input is captured with hardware timing) and how individual pins are written/cleared will be discussed here, given I've already discussed how the motors are translated and rotated (serial commands issued via the LabView stock VI "basic_serial_write_and_read.vi").

The National Instruments USB-6509 DAQ has 96 total pins capable of I/O (4 pins are dedicated as voltage and ground connections) [27]. It is capable of onboard timing such that, if a specified pin undergoes a rising or falling edge, it reports the new status of the register to the host computer. This is known as "change detection" and can be harnessed within LabView using code featured in Figure 2.16.

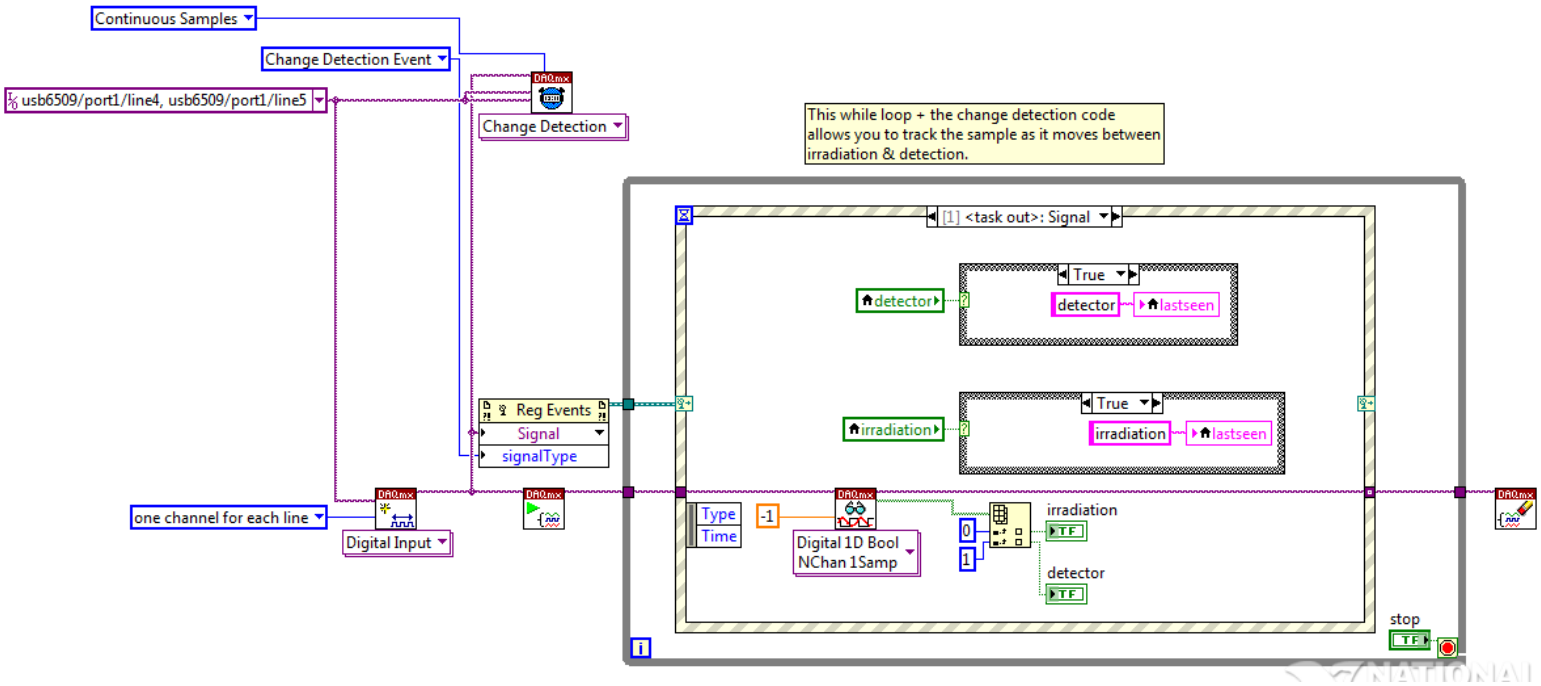

Figure 2.16: An example of how change detection is used in the automated cyclic VI. The code constantly poll the two sensor inputs, connected to port 1, lines 4 & 5 of the DAQ. If a change detection event occurs, the signal is registered as an event LabView can respond unto, which it does, by reading the current value of the detected signal and outputting the value to a box on the front panel informing the user where the sample was last seen.

It should be of note that this isn't "pure" hardware timing, like the prototype circuit capable of discerning prompt gamma removal. This requires the computer to see a pin 'high' and respond by writing another pin 'high' or 'low', hence, the reaction speed is inherent to the host computer speed. Whereas the prompt gamma removal circuit could achieve timing operations limited by the DIP ICs (approximately microseconds), the timing of the USB bus, the attenuation in the wiring, and the fact that LabView is far from optimized lead to a response speed on the order of milliseconds. It is thereby ill-advised to use change detection control with a pulsed neutron generator operating above 250 Hz, and a more appropriate solution would be to use a more costly DAQ with onboard hardware timing or fabricate the timing circuitry yourself.

As aforementioned, the valves and detector are controlled similarly, with most of the heavy lifting having been done circuitry-side. Essentially, all that needs to be done in order to force a count or a valve actuate is to write a 5V signal to a pin and then ground the pin when the operation is completed. This is presented schematically in the following two figures, Figs. 2.17 & 2.18.

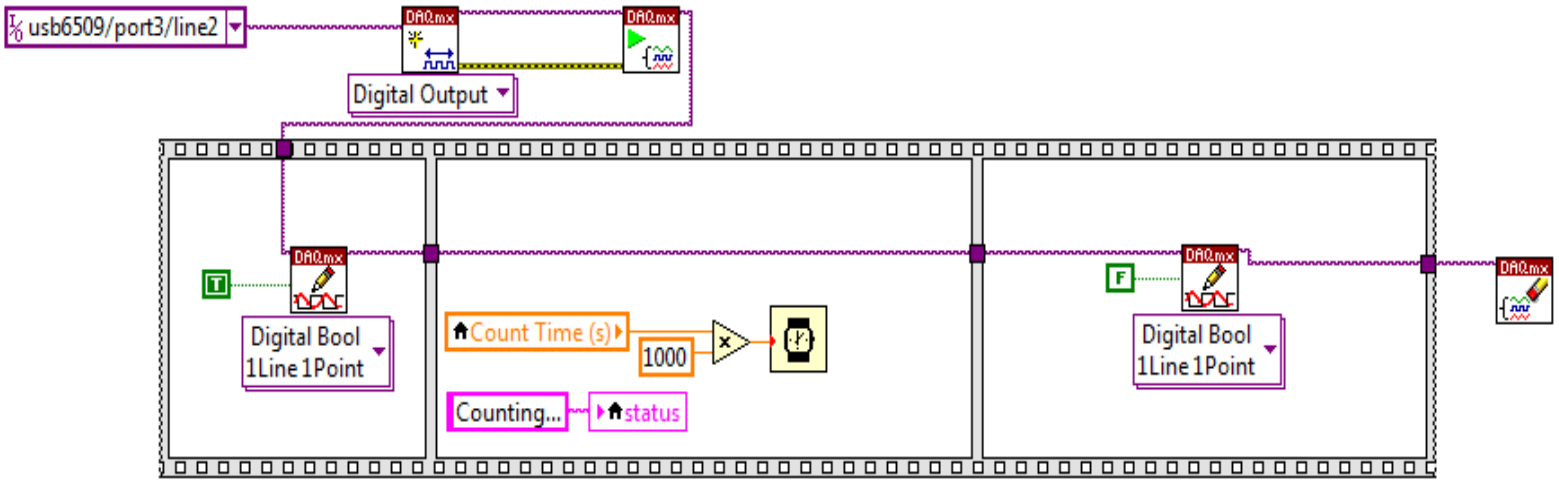

Figure 2.17: An example of how a count is initiated on the detector. The detector's pin (in this case, port3, line2 on the DAQ) is initialized as a Digital Output, and a sequential structure is initiated. The first pane writes the digital Boolean signal to the pin with a value of 'true'; the second pane has the software wait until the user inputted time has elapsed; the third pane concludes the count by writing a digital Boolean signal to the pin with a value of 'false'. The task is then cleared from memory.

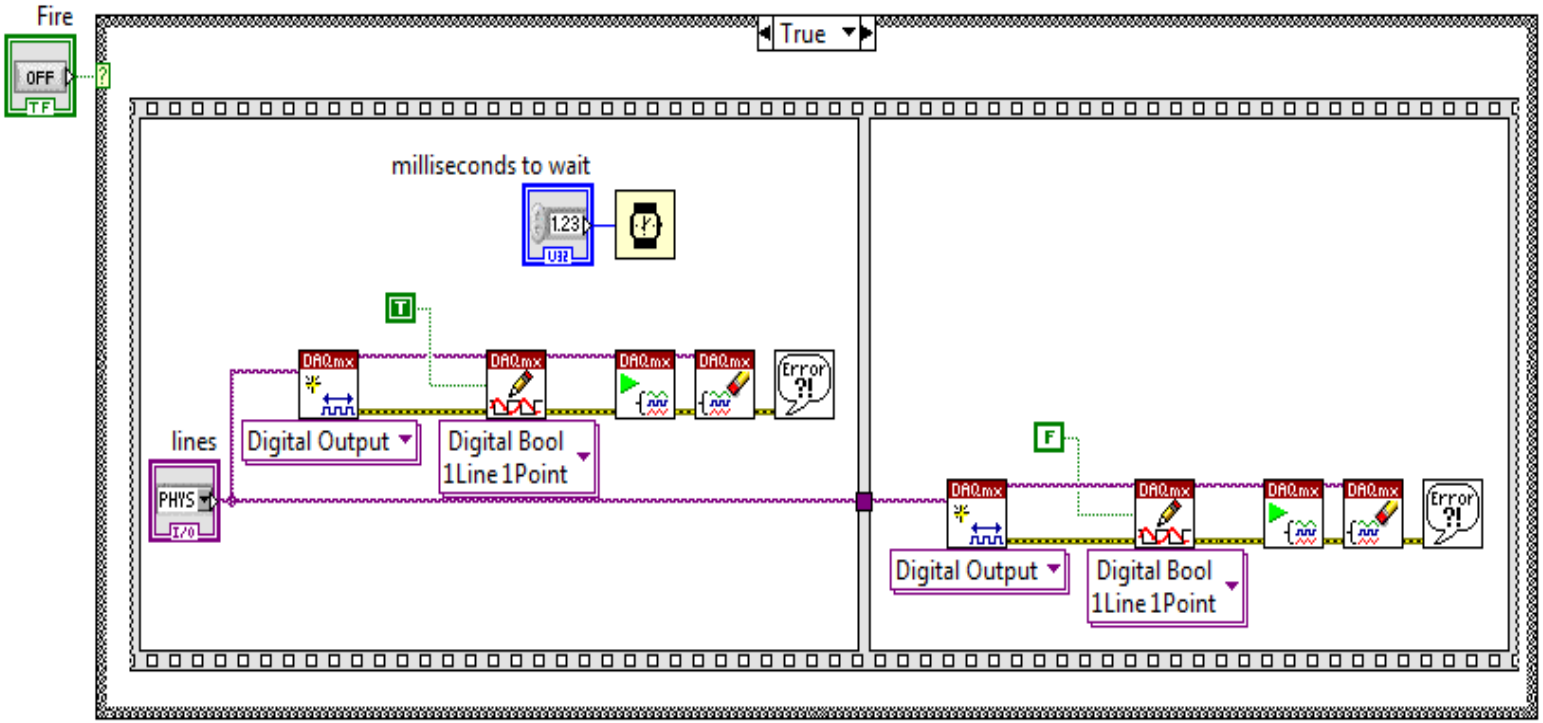

Figure 2.18: An example of how a valve is actuated. This is a special type of LabView VI that enforces a non-reentrant execution, allowing for generic inputs from any of the three valves and not being able to open more than one valve at once. The user inputs the number of milliseconds to wait and the valve pin he wishes to open. When the hits the Boolean input, the case structure evaluates as true, the logical high is written to the valve, and it actuates. After waiting a prescribed amount of time, the 'low' signal is written to the valve, shutting it.

STANDARD OPERATING PROCEDURE

The typical operating procedure using the fast pneumatic cyclic irradiation facility at the University of Texas at Austin is as follows:

1. Ensure the switch on the wall-mounted electronics box (adjacent to the proton recoil scintillator-Los Alamos [PRESCILA] detector) is on (in the "Up" position), the air compressor is energized, the manifold pressure regulator is set to 40 psig, and the power supply to the motors (near the detector) is on.
2. Load a sample into the wall-mounted sample loader at the facility's control computer.
3. Using the LabView interface, hit "Load a sample", which rotates the shaft of a stepper motor and drops the sample into the sample tube.
4. Hit the "linear valve" button in Labview, which actuates a valve and causes the pneumatic line behind the sample to pressurize, pushing the sample up and over the wall intermediate to you and the neutron generator.
5. The sample arrives at the diverter. Hit the "Lower the diverter" button in LabView to force the sample into the irradiation/detection channel, instead of the waste/loading channel.
6. Hit the "angle valve 1" button in Labview, which pushes the sample from the diverter to the detector.
7. Hit the "Raise the diverter" button in LabView to place the diverter in a position where there is no obstruction between the detector and irradiation site.

8. For manual irradiations, you can now proceed to power up the MP320 Neutron Generator on the sister control computer and hit “angle valve 2” to open the air flow behind the sample at the detector, pushing it to the 14 MeV neutron source. When you have achieved a desired fluence into the sample, hit “angle valve 1” to return the sample to the detector, where you may initiate a count manually within Maestro.
9. For automated cyclic irradiations, a second LabView VI has been provided. Using the manual controls, ensure the sample has been placed at the detector and the detector/irradiation path is clear (the diverter is in the upright position); furthermore, ensure the loose RG-56 Coaxial cable is connected to the “SAMPLE IN” connection on the DSpec-PRO, which controls the detector. Close “FPS.vi” and load “FPS-AUTO.vi”. Start the detector acquisition. This VI takes a user-input number of cycles, irradiation time, and count time, and will automatically actuate the valves to move the sample between the detector and irradiation; in the case the sample does not make it to its destination, the valve is re-actuated. If the sample travel is critical (irradiation -> detector), it will not log a count if it did not reach the detector on its very first attempt, and will wait the count-time and re-initiate a new cycle. Once the cycles are completed, the sample will be resting at the detector; the onus is on the user to end the detector acquisition. The data will be split between two channels – one which is indicative of a background (all events when the activated sample was not present), and the other will be all acquisition that occurred with the sample present.

10. When the manual/automated irradiations have been completed, reload "FPS.vi" to assume manual control of the facility, move the sample to the irradiation site by hitting the "angle valve 2" button, if the sample is currently sitting at the detector. Once the sample arrives at the irradiation site, lower the diverter by pressing the "lower the diverter" button. Fire the sample towards the detector using the "angle valve 1" button; it will stop at the diverter, which you can discern by listening. Raise the diverter by hitting the "raise the diverter" button, placing the sample back into the obstructed waste/loading pathway. Actuate the linear valve by hitting the "linear valve" button, firing the sample to waste.
11. Either repeat steps 1-10 for additional samples, or power the neutron generator down, evacuate the air compressor, and power down the controls & motors.

Chapter 3: Neutron Generator Flux Characterization

MOTIVATION

Given the experimental arrangement of the neutron generator (shown in Figure 3.1), as well as the stainless steel terminal that holds the sample during irradiation and attenuation due to the sample vial itself, a flux measurement and energy characterization was in order to verify that the flux wasn't too far perturbed from the 'pure' 14 MeV flux the generator produces. This is important to document, as verification that a pure 14 MeV flux allows you the capability of modeling irradiation trials using only 14 MeV cross-sections, removing the need to unfold a more complicated flux spectrum (which, in turn, would further increase relative error on any and all measurements conducted).

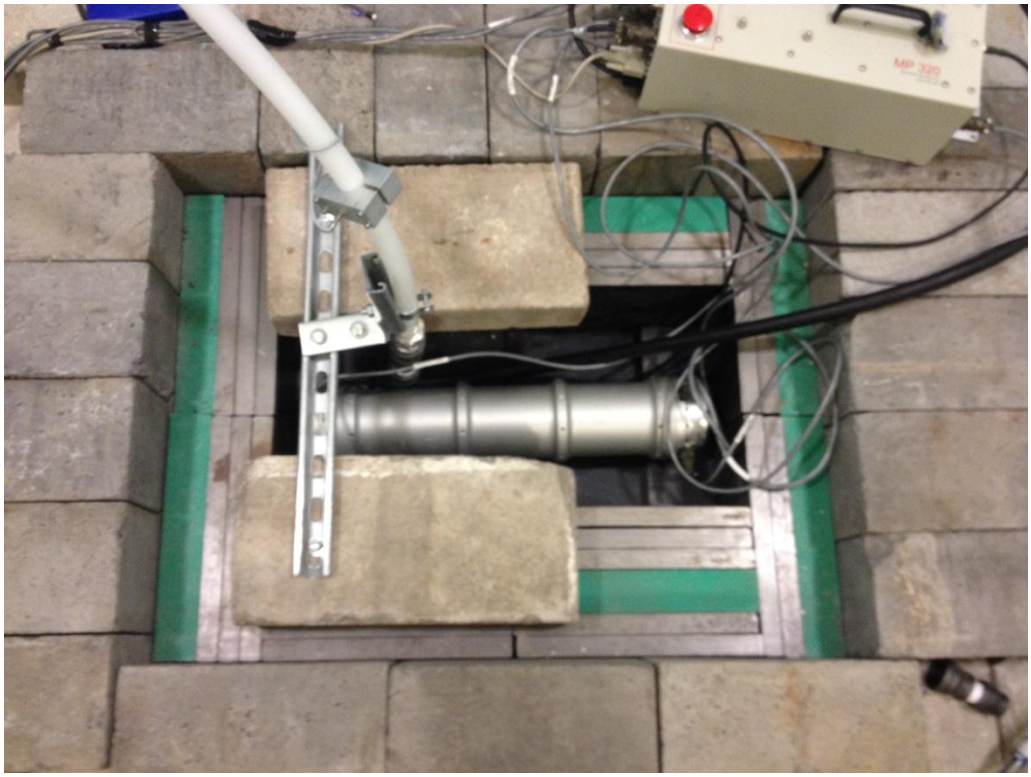

Figure 3.1: Neutron generator from above; note surrounding stainless steel plates (silver), borated polyethylene (green), and leaded concrete.

To solve for an expected flux, the crude approximation can be made that the neutron generator is a point source in a vacuum. The falloff due to geometric attenuation alone is defined as:

$$\phi = \frac{S}{4\pi r^2} \tag{3.1}$$

The source strength, per the manufacturer Thermo Electron Corporation of the MP320 Neutron Generator, is "~10^8 neutrons/s" (see Appendix A). The metal body of the neutron generator is approximately 4" in diameter, while the sample holder sits at its perimeter, 1.5" wide, shown in Figure 3.2.

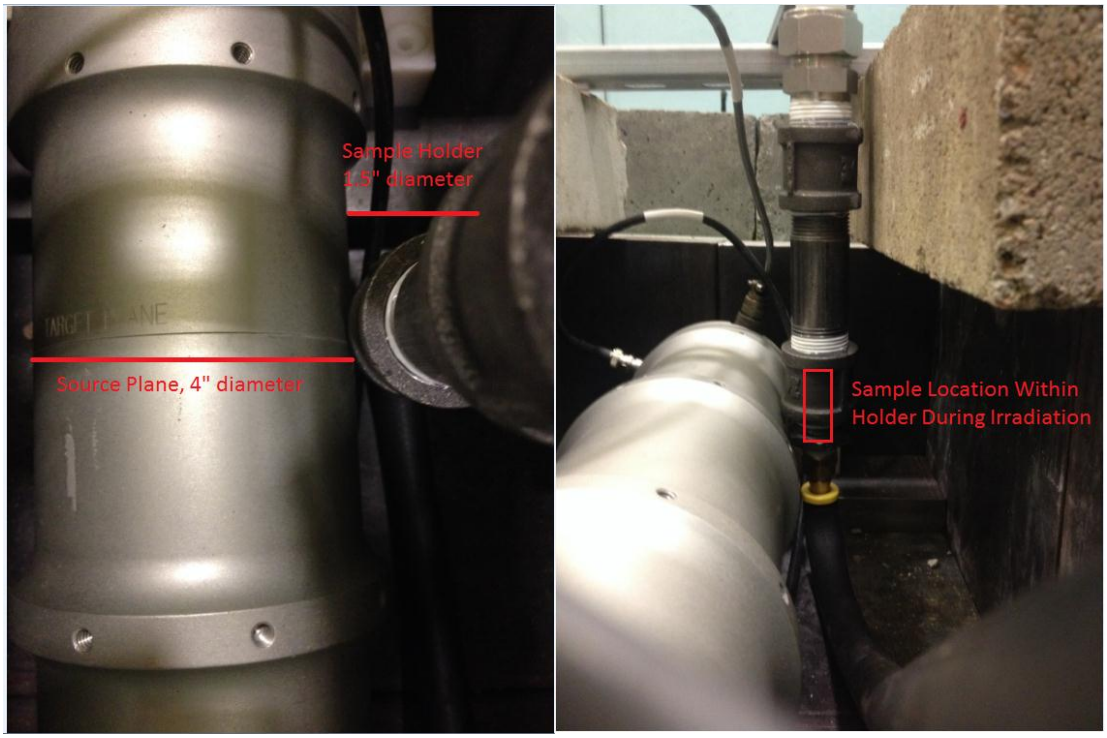

Figure 3.2: Orientation & location of sample during irradiation. The sample is held 2.75" from the center of the plane of irradiation; samples were prepared such that the target material was at the bottom of the irradiation vial to ensure orthogonality between the neutron generator & target.

Hence, as a first-order approximation of the flux, one may evaluate the source-strength falloff due to geometric attenuation alone at 100% duty cycle, or:

$$\phi = \frac{S}{4\pi r^2} = \frac{1E8\ n/s}{4\pi(6.985cm)^2} = 1.63E5\frac{n}{cm^2 * s} \tag{3.2}$$

THEORETICAL APPROACH TO REFINE THE FLUX CHARACTERIZATION

Due to the plethora of materials around the neutron generator that allow for the downscattering or elastic scattering of neutrons, it would be foolish to directly use a flux ascribed only to geometric attenuation in any precise computation; instead, a more desirable approach would be to perform neutron activation analysis with known reference materials and observe the decay of the activation products.

For a typical irradiation, decay, and count procedure, one may derive the total counts expected as follows:

During irradiation, a quantity of atoms N ingrown due to the irradiation of target atoms n with interaction probability σ, flux ϕ, and decay constant λ:

$$\frac{dN_i}{dt} = n\sigma\phi - \lambda N_i \tag{3.3}$$

$$\frac{dN_i}{dt} + \lambda N_i = n\sigma\phi \tag{3.4}$$

$$\left[\frac{dN_i}{dt} + \lambda N_i\right] e^{\lambda t} = n\sigma\phi e^{\lambda t} \tag{3.5}$$

$$\frac{d\{N_i e^{\lambda t}\}}{dt} = n\sigma\phi e^{\lambda t} \tag{3.6}$$

$$N_i e^{\lambda t} = \frac{n\sigma\phi e^{\lambda t}}{\lambda} + K \tag{3.7}$$

$$N_i = \frac{n\sigma\phi e^{\lambda t}}{\lambda} + Ke^{-\lambda t} \tag{3.8}$$

Under the assumption that the sample begins unactivated, the initial activity is zero:

$$N_i(0) = \frac{n\sigma\phi}{\lambda} + K = 0 \quad \rightarrow \quad K = -\frac{n\sigma\phi}{\lambda} \tag{3.9}$$

$$N_i(t) = \frac{n\sigma\phi}{\lambda}\left(1 - e^{-\lambda t}\right) \tag{3.10}$$

While the sample is in transit to the detector, the sample experiences only decay:

$$\frac{dN_d}{dt} = -\lambda N_d \tag{3.11}$$

$$\frac{dN_d}{N_d} = -\lambda\, dt \tag{3.12}$$

$$N_d = De^{-\lambda t} \tag{3.13}$$

If the beginning of the decay coincides with the end of irradiation, these two functions much match at their interface, or:

$$N_i(t_i) = \frac{n\sigma\phi}{\lambda}\left(1 - e^{-\lambda t_i}\right) = N_d(0) = D \tag{3.14}$$

$$N_d = \frac{n\sigma\phi}{\lambda}\left(1 - e^{-\lambda t_i}\right)e^{-\lambda t} \tag{3.15}$$

Once the sample has made it to the detector, the sample still experiences only decay:

$$\frac{dN_c}{dt} = -\lambda N_c \tag{3.16}$$

$$\frac{dN_c}{N_c} = -\lambda\, dt \tag{3.17}$$

$$N_c = Ee^{-\lambda t} \tag{3.18}$$

And again, matching interface conditions:

$$N_d(t_d) = \frac{n\sigma\phi}{\lambda}\left(1 - e^{-\lambda t_i}\right)e^{-\lambda t_d} = N_c(0) = E \tag{3.19}$$

$$N_c = \frac{n\sigma\phi}{\lambda}\left(1 - e^{-\lambda t_i}\right)e^{-\lambda t_d}e^{-\lambda t} \tag{3.20}$$

Finally, to find the expected number of decays in a counting interval, integrate the activity over a specified time window:

$$A = \lambda N_c = n\sigma\phi\left(1 - e^{-\lambda t_i}\right)e^{-\lambda t_d}e^{-\lambda t} \tag{3.21}$$

$$\int_0^{t_c} A\, dt = \int_0^{t_c} \lambda N_c\, dt = n\sigma\phi\left(1 - e^{-\lambda t_i}\right)e^{-\lambda t_d}\int_0^{t_c} e^{-\lambda t}\, dt \tag{3.22}$$

$$decays = n\sigma\phi\left(1 - e^{-\lambda t_i}\right)e^{-\lambda t_d}\left[\frac{-e^{-\lambda t}}{\lambda}\right]_0^{t_c} \tag{3.23}$$

$$decays = \frac{n\sigma\phi}{\lambda}\left(1 - e^{-\lambda t_i}\right)e^{-\lambda t_d}\left(1 - e^{-\lambda t_c}\right) \tag{3.24}$$

Lastly, given we are working from detector data and not raw counts, multiply by detector efficiency for a given photopeak and its respective yield to arrive at the familiar expression for total counts:

$$C = \frac{N\sigma\phi\varepsilon\gamma}{\lambda}\left(1 - e^{-\lambda t_i}\right)e^{-\lambda t_d}\left(1 - e^{-\lambda t_c}\right) \tag{3.25}$$

with: C = total counts observed (counts)

N = total number of target atoms (atoms)

σ = cross-section for the evaluated reaction (cm^{-2})

ϕ = neutron flux ($ncm^{-2}s^{-1}$)

ε = efficiency of the detector for the given photopeak energy (fractional)

γ = absolute intensity of given photopeak (fractional)

λ = decay constant [ln(2) / half-life] ($seconds^{-1}$)

t_i = irradiation time (seconds)

t_d = decay time (seconds)

t_c = count time (seconds)

Rewriting this expression for our unknowns, we create our response function, the product of the flux and cross-section, attributed to a given photopeak created by a given activation reaction:

$$[\sigma\phi] = \frac{C\lambda}{N\varepsilon\gamma(1 - e^{-\lambda t_i})e^{-\lambda t_d}(1 - e^{-\lambda t_c})} \tag{3.26}$$

Assuming negligible errors on the atomic content, detector efficiency, absolute intensity of the photopeak, and the timing of the irradiation/decay/count cycles, the error in the function is prescribed to the error in fitting a Gaussian when performing the spectral analysis:

$$\Delta[\sigma\phi] = \frac{\Delta C\lambda}{N\varepsilon\gamma(1-e^{-\lambda t_i})e^{-\lambda t_d}(1-e^{-\lambda t_c})} \tag{3.27}$$

In the event that *j* photopeaks correspond to the same activation reaction *i*, the response function for that reaction can be further refined by weighting each of the measurements by the inverse of the variance, given they are independent events [28]:

$$w_{i,j} = \frac{1}{\left(\Delta[\sigma\phi]_{i,j}\right)^2} \tag{3.28}$$

$$[\sigma\phi]_i = \frac{\sum_j w_{i,j}[\sigma\phi]_{i,j}}{\sum_j w_{i,j}} \tag{3.29}$$

$$\Delta[\sigma\phi]_i = \sqrt{\frac{1}{\sum_j w_{i,j}}} \tag{3.30}$$

Once a vector of properly weighted responses $[\sigma\phi]$ has been built for all observed reactions, a diagonal matrix of the variances for each reaction W must be built:

$$W = diag\left(\frac{1}{\Delta[\sigma\phi]_i^2}\right) \tag{3.31}$$

Lastly, the cross-section matrix (denoted Σ below) must be built from nuclear data. The easiest way to do this is to use NJOY99 to Doppler broaden and collapse cross-

sections to a prescribed structure, and build a matrix on a row-by-row basis of these cross-sections (see Appendix D).

The problem statement to find the fluxes representative of a prescribed group structure (below, denoted as *l* groups) has now been recast as a constrained (nonnegative, weighted) least squares problem [29]:

$$\min_{\phi \in \mathcal{R}^l} \|W\Sigma\phi - W[\sigma\phi]\|^2 \quad \forall l: \phi_l \geq 0 \tag{3.32}$$

FAST REACTION SCOPING & EXPERIMENTAL PREPARATION

In order to determine which reaction may be relevant given an estimated 14 MeV flux of 2 x 10^5 $ncm^{-2}s^{-1}$, the one-dimensional depletion code ORIGEN2.2 (Oak Ridge Isotope Generation and Depletion Code Version 2.2) was used with unit elemental masses of aluminum, magnesium, molybdenum, scandium, cobalt, zirconium, and iron [30][31].

In order to mimic the 'fast' nature of the neutron flux to the best of ORIGEN2.2's stock capability, the "AMORUUC.LIB" cross-section library was used, originally designed for an Advanced oxide recycle-Pu/U/U/U LMFBR core (library numbers 321, 322, 323), alongside the executable version of ORIGEN2.2 with a fast flux, "O2_FAST.EXE". Though this cross-section set is for a fast fission spectrum, it was used as a first-order scoping tool to gauge ORIGEN2.2's ability before manipulating individual cross-sections.

Using a flux of 2 x 10^5 $ncm^{-2}s^{-1}$, an irradiation time of one hour, and a decay time of two minutes, the results were as follows:

Table 3.1: ORIGEN2.2 predicted activation products associated with a 100g elemental Aluminum sample irradiated at 2 x 10^5 $ncm^{-2}s^{-1}$ for one hour and allowed to decay for two minutes.

Activation Product	Reaction	Activity At End of Sixty Minute Irradiation (Bq)	Activity Two Minutes After Irradiation (Bq)
^{24}Na	$^{27}Al(n,\alpha)$	1.94	1.93
^{27}Mg	$^{27}Al(n,p)$	202	175
^{28}Al	$^{27}Al(n,\gamma)$	117	63

Table 3.2: ORIGEN2.2 predicted activation products associated with a 100g elemental Magnesium sample irradiated at 2 x 10^5 $ncm^{-2}s^{-1}$ for one hour and allowed to decay for two minutes.

Activation Product	Reaction	Activity At End of Sixty Minute Irradiation (Bq)	Activity Two Minutes After Irradiation (Bq)
^{24}Na	$^{24}Mg(n,p)$	3.47	3.47
^{25}Na	$^{25}Mg(n,p)$	14.2	3.53

Table 3.3: ORIGEN2.2 predicted activation products associated with a 100g elemental Molybdenum sample irradiated at 2 x 10^5 $ncm^{-2}s^{-1}$ for one hour and allowed to decay for two minutes.

Activation Product	Reaction	Activity At End of Sixty Minute Irradiation (Bq)	Activity Two Minutes After Irradiation (Bq)
^{101}Mo	$^{100}Mo(n,\gamma)$	823	749
^{101}Tc	^{101}Mo decay	685	694

Table 3.4: ORIGEN2.2 predicted activation products associated with a 100g elemental Scandium sample irradiated at 2 x 10^5 $ncm^{-2}s^{-1}$ for one hour and allowed to decay for two minutes.

Activation Product	Reaction	Activity At End of Sixty Minute Irradiation (Bq)	Activity Two Minutes After Irradiation (Bq)
^{42}K	$^{45}Sc(n,\alpha)$	8.04E-2	8.03E-2
^{46}Sc	$^{45}Sc(n,\gamma)$	1.61	1.61
^{46m}Sc	$^{45}Sc(n,\gamma^*)$	1690	19.7

Table 3.5: ORIGEN2.2 predicted activation products associated with a 100g elemental Cobalt sample irradiated at 2 x 10^5 $ncm^{-2}s^{-1}$ for one hour and allowed to decay for two minutes.

Activation Product	Reaction	Activity At End of Sixty Minute Irradiation (Bq)	Activity Two Minutes After Irradiation (Bq)
^{60m}Co	$^{59}Co(n,\gamma^*)$	12617	11051.9

Table 3.6: ORIGEN2.2 predicted activation products associated with a 100g elemental Zirconium sample irradiated at 2 x 10^5 $ncm^{-2}s^{-1}$ for one hour and allowed to decay for two minutes.

Activation Product	Reaction	Activity At End of Sixty Minute Irradiation (Bq)	Activity Two Minutes After Irradiation (Bq)
^{90}Y	$^{90}Zr(n,p)$	9.89E-2	9.89E-2
^{91}Y	$^{91}Zr(n,p)$	3.03E-4	3.03E-4
^{92}Y	$^{92}Zr(n,p)$	9.47E-2	9.41E-2

Table 3.7: ORIGEN2.2 predicted activation products associated with a 100g elemental Iron sample irradiated at 2 x 10^5 $ncm^{-2}s^{-1}$ for one hour and allowed to decay for two minutes.

Activation Product	Reaction	Activity At End of Sixty Minute Irradiation (Bq)	Activity Two Minutes After Irradiation (Bq)
^{56}Mn	$^{56}Fe(n,p)$	34.4	34.1
^{57}Mn	$^{57}Fe(n,p)$	0.267	0.113

In running the scoping simulations, it should be noted that ORIGEN2.2 did not output a single (n,2n) reaction, which seems to suggest the cross-section library is not indicative of some of the threshold reactions that should be modeled in a 14 MeV flux, but instead a fission spectrum; at first glance, the $^{45}Sc(n,\alpha)^{42}K$ reaction has a cross-section of 53.3 millibarns at 14 MeV and a cross-section of 2.518 millibarns in the fission spectrum, while the $^{45}Sc(n,2n)^{44}Sc$ reaction has a cross-section of 240.0 millibarns at 14 MeV and a 37.9 microbarn cross-section in the fission spectrum [32].

To improve the capability of ORIGEN2.2 in scoping the experiment, the cross-section library employed ("AMORUUC.LIB") was modified. The structure of the cross-section library for an individual activation nuclide is as follows:

NLB NUCLID SNG SN2N SNA SNP SNGX SN2NX YYN

where:

NLB is the numeric identifier of the cross-section set.

NUCLID is a six digit nuclide identification code.

SNG is the cross-section for radioactive capture (barns).

SN2N is the cross-section for the (n,2n) reaction (barns).

SNA is the cross-section for the (n,a) reaction (barns).

SNP is the cross-section for the (n,p) reaction (barns).

SNGX is the cross-section for (n,g'), leaving the product nucleus in the first excited state (barns).

SN2NX is the cross-section for (n,2n'), leaving the product nucleus in the first excited state.

YYN is an identifier such that, if equal to 1, a fission yield card will follow, and if -1, no fission yield card follows.

NJOY99 was used to develop a one-group effective cross-section for an energy band of 12 – 14 MeV Doppler broadened to 25C for the six cross-sections used for activation products, and the original library ("AMORUUC.LIB") was modified on a line-by-line basis to reflect these new cross-sections that are better representative of a 14 MeV neutron source [33][34]. The file and tab locations of the nuclear data used, from ENDF-B/VII.1, are presented in Table 3.8.

Table 3.8: ORIGEN2.2 cross-section to ENDF index equivalence.

ORIGEN2.2 Variable	Reaction	ENDF File	MT Index
SNG	(n,γ)	3	102
SN2N	(n,2n)	3	16
SNA	(n,α)	3	107
SNP	(n,p)	3	103
SNGX	(n, γ*)	9 & 3	102
SN2NX	(n,2n')	3	876

The following cross-sections were modified in the original library, to match the foils under consideration:

```
%% Library is of the form:
%% NLB NUCLID SNG SN2N SNA SNP SNGX SN2NX YYN
%%
%%  Aluminum
321   130270 5.673E-04 2.496E-04 1.221E-01 8.121E-02 0.0 0.0         -1.0

%%  Magnesium
321   120240 6.374E-05 0.0       2.112E-01 2.010E-01 0.0 0.0         -1.0
321   120250 1.270E-05 6.011E-01 1.540E-01 4.692E-02 0.0 0.0         -1.0

%%  Molybdenum
321   420920 1.157E-03 2.352E-02 1.537E-02 1.487E-01 0.0 0.0         -1.0
321   420940 1.080E-03 9.077E-01 1.613E-02 4.336E-02 0.0 0.0         -1.0
321   420950 9.692E-04 1.303     1.192E-02 2.503E-02 0.0 0.0         -1.0
321   420960 1.061E-03 1.139     8.075E-03 1.398E-02 0.0 0.0         -1.0
321   420970 1.040E-03 1.323     4.949E-03 9.409E-03 0.0 0.0         -1.0
321   420980 9.991E-04 1.213     3.385E-03 2.637E-03 0.0 0.0         -1.0
321   421000 1.024E-03 1.405     1.474E-03 7.633E-04 0.0 0.0         -1.0

%%  Scandium
321   210450 2.840E-04 9.408E-02 3.827E-02 7.023E-02 0.0 0.0         -1.0

%%  Cobalt
321   270590 8.205E-04 4.532E-01 2.675E-02 5.068E-02 0.0 0.0         -1.0

%%  Zirconium
321   400900 9.655E-04 1.841E-01 0.0       0.0       0.0 0.0         -1.0
321   400910 6.697E-04 1.101     0.0       0.0       0.0 0.0         -1.0
321   400920 8.446E-04 1.114     0.0       0.0       0.0 0.0         -1.0
321   400940 5.634E-04 1.231     0.0       0.0       0.0 0.0         -1.0
321   400960 4.450E-04 1.273     0.0       0.0       0.0 0.0         -1.0

%%  Iron
321   260540 7.164E-04 1.177E-01 7.780E-02 4.161E-01 0.0 0.0         -1.0
321   260560 5.337E-04 1.834E-01 4.367E-02 1.117E-01 0.0 0.0         -1.0
321   260570 7.164E-04 9.572E-01 2.898E-02 5.038E-02 0.0 0.0         -1.0
321   260580 7.164E-04 6.738E-01 1.799E-02 7.131E-03 0.0 0.0         -1.0
```

Given that the inelastic radiative capture (n, γ*) are represented in ENDF as fractions of radiative capture, it was assumed (particularly given how low the radiative capture cross-sections were) that inelastic radiative capture cross-sections could be considered zero.

The scoping trials were then repeated, with updated cross-sections, and the results tables from the before and after the cross-section substitution were compared:

Table 3.9: ORIGEN2.2 predicted activation products associated with a 100g elemental Aluminum sample irradiated at 2 x 10^5 $ncm^{-2}s^{-1}$ for one hour and allowed to decay for two minutes, before and after the cross-section update.

Product	Reaction	Activity (60m), AMORUUC.lib	Activity (62m), AMORUUC.lib	Activity (60m), modified library	Activity (62m), modified library
^{24}Na	$^{27}Al(n,\alpha)$	1.94	1.93	2461	2457
^{27}Mg	$^{27}Al(n,p)$	202	175	35794	30917
^{28}Al	$^{27}Al(n,\gamma)$	117	63	253	136

Table 3.10: ORIGEN2.2 predicted activation products associated with a 100g elemental Magnesium sample irradiated at 2 x 10^5 $ncm^{-2}s^{-1}$ for one hour and allowed to decay for two minutes, before and after the cross-section update.

Product	Reaction	Activity (60m), AMORUUC.lib	Activity (62m), AMORUUC.lib	Activity (60m), modified library	Activity (62m), modified library
^{24}Na	$^{24}Mg(n,p)$	3.47	3.47	3600	3595
^{25}Na	$^{25}Mg(n,p)$	14.2	3.53	2261	560

Table 3.11: ORIGEN2.2 predicted activation products associated with a 100g elemental Molybdenum sample irradiated at 2 x 10^5 $ncm^{-2}s^{-1}$ for one hour and allowed to decay for two minutes, before and after the cross-section update.

Product	Reaction	Activity (60m), AMORUUC.lib	Activity (62m), AMORUUC.lib	Activity (60m), modified library	Activity (62m), modified library
^{101}Mo	^{100}Mo(n,γ)	823	749	11.19	10.18
^{101}Tc	^{101}Mo decay	685	694	9.31	9.43

Table 3.12: ORIGEN2.2 predicted activation products associated with a 100g elemental Scandium sample irradiated at 2 x 10^5 $ncm^{-2}s^{-1}$ for one hour and allowed to decay for two minutes, before and after the cross-section update.

Product	Reaction	Activity (60m), AMORUUC.lib	Activity (62m), AMORUUC.lib	Activity (60m), modified library	Activity (62m), modified library
^{42}K	^{45}Sc(n,α)	8.04E-2	8.03E-2	559	558
^{46}Sc	^{45}Sc(n,γ)	1.61	1.61	0	0
^{44}Sc	^{45}Sc(n,2n)	0	0	4077	4052

Table 3.13: ORIGEN2.2 predicted activation products associated with a 100g elemental Cobalt sample irradiated at 2 x 10^5 $ncm^{-2}s^{-1}$ for one hour and allowed to decay for two minutes, before and after the cross-section update.

Product	Reaction	Activity (60m), AMORUUC.lib	Activity (62m), AMORUUC.lib	Activity (60m), modified library	Activity (62m), modified library
^{60m}Co	$^{59}Co(n,\gamma^*)$	12617	11051.9	0	0
^{56}Mn	$^{59}Co(n,\alpha)$	0	0	1288	1276
^{59}Fe	$^{59}Co(n,p)$	0	0	6.6	6.6
^{58}Co	$^{59}Co(n,2n)$	0	0	37.8	37.8

Table 3.14: ORIGEN2.2 predicted activation products associated with a 100g elemental Zirconium sample irradiated at 2 x 10^5 $ncm^{-2}s^{-1}$ for one hour and allowed to decay for two minutes, before and after the cross-section update.

Product	Reaction	Activity (60m), AMORUUC.lib	Activity (62m), AMORUUC.lib	Activity (60m), modified library	Activity (62m), modified library
^{90}Y	$^{90}Zr(n,p)$	9.89E-2	9.89E-2	0	0
^{91}Y	$^{91}Zr(n,p)$	3.03E-4	3.03E-4	0	0
^{92}Y	$^{92}Zr(n,p)$	9.47E-2	9.41E-2	0	0

Table 3.15: ORIGEN2.2 predicted activation products associated with a 100g elemental Iron sample irradiated at 2 x 10^5 $ncm^{-2}s^{-1}$ for one hour and allowed to decay for two minutes, before and after the cross-section update.

Product	Reaction	Activity (60m), AMORUUC.lib	Activity (62m), AMORUUC.lib	Activity (60m), modified library	Activity (62m), modified library
^{56}Mn	^{56}Fe(n,p)	34.4	34.1	5199	5150
^{57}Mn	^{57}Fe(n,p)	0.267	0.113	226	95.4

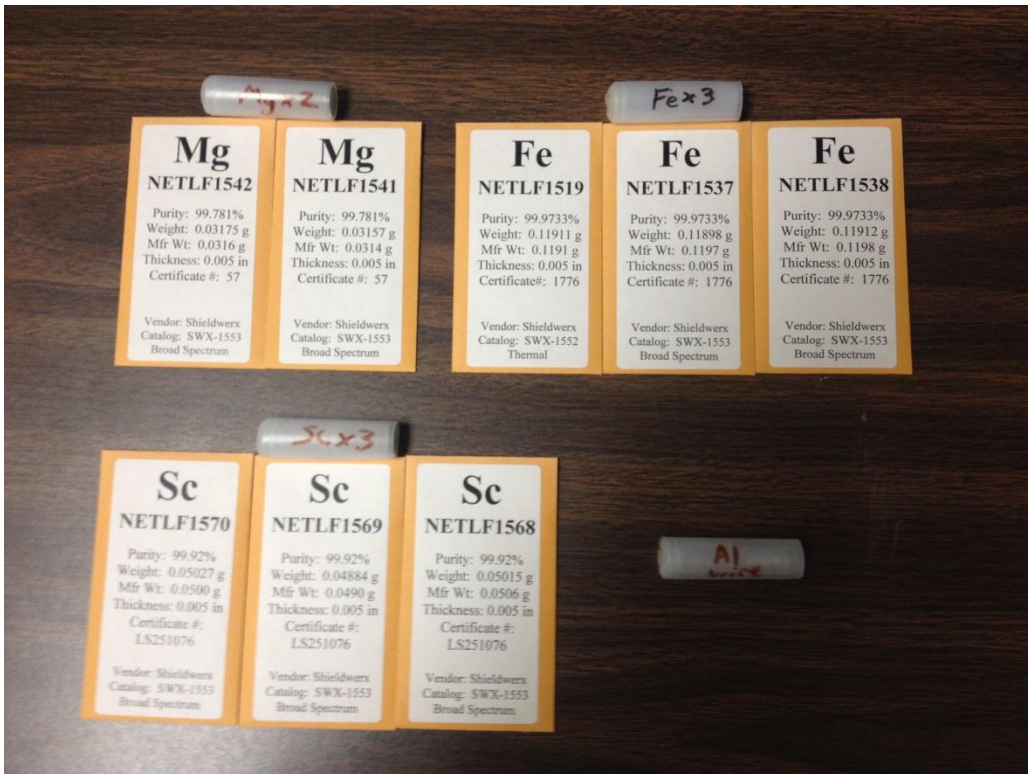

Figure 3.3: The four heat-sealed sample vials: a sample vial containing two magnesium foils, totaling 0.063181g; a sample vial containing three iron foils, totaling 0.357115g; a sample vial containing three scandium foils, totaling 0.149141g; a sample vial containing a small spool of aluminum wire, 0.75455g. The reference standard information is also included, with the exception of aluminum wire, which was referenced as 99.9957% pure.

Based on the Origen2 data using the new cross-section data, and basing a "cutoff" at 3 kBq, four samples were chosen – magnesium, iron, scandium, and aluminum, as shown in Figure 3.3.

Before proceeding with the irradiation trials, an efficiency curve was established for the detector using a mixed gamma radioactive source-- an electroplated point source in tape on a 2" Aluminum Ring (ID# 93098) containing ^{210}Pb, ^{241}Am, ^{109}Cd, ^{57}Co, ^{139}Ce, ^{203}Hg, ^{113}Sn, ^{137}Cs, ^{88}Y, and ^{60}Co. The curve fit was a log-log fifth order polynomial, shown in Figure 3.4.

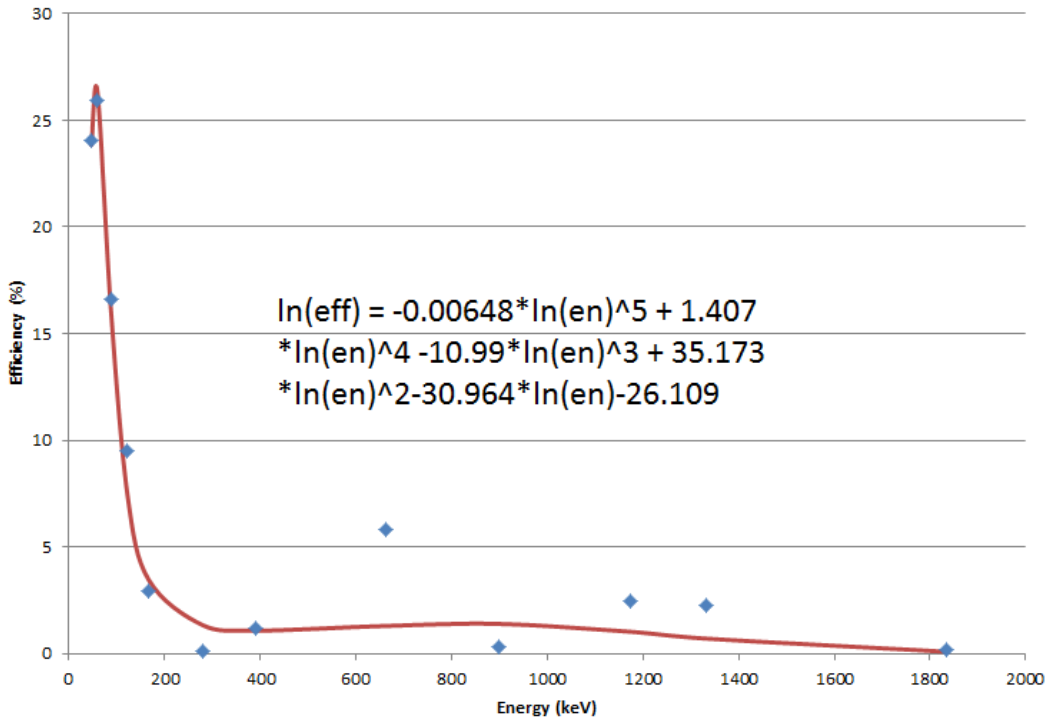

Figure 3.4: The efficiency curve generated by fitting a log-log fifth order polynomial to a one hour count of mixed gamma source standard 93098 prior to beginning irradiation trials.

EXPERIMENTAL DATA & RESULTS

The gamma spectra of the irradiations of the aluminum, iron, magnesium, and scandium are presented in the following four figures, Figs. 3.5, 3.6, 3.7, and 3.8. Their principal activation reactions and emissions are labeled. The irradiation, decay, and count times are presented in Table 3.16.

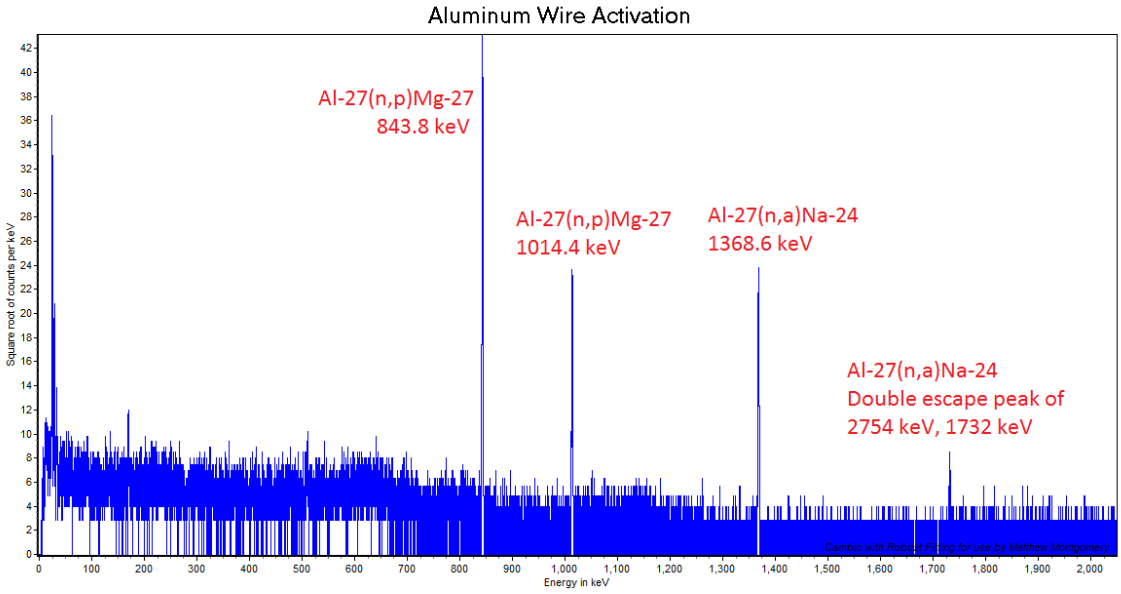

Figure 3.5: The spectral results of the irradiation trial of aluminum.

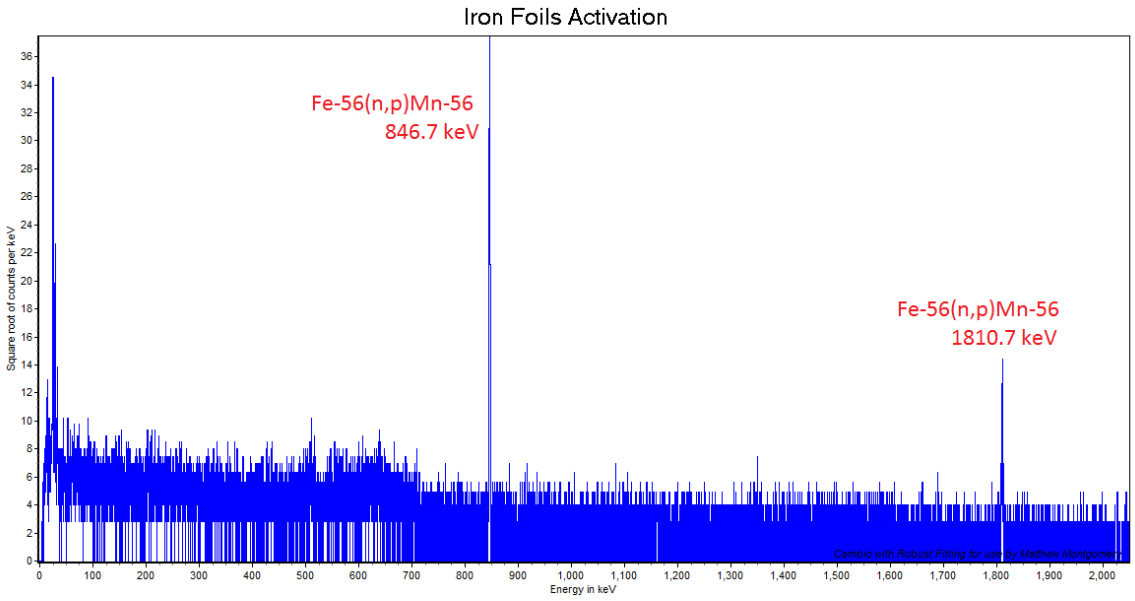

Figure 3.6: The spectral results of the irradiation trial of iron.

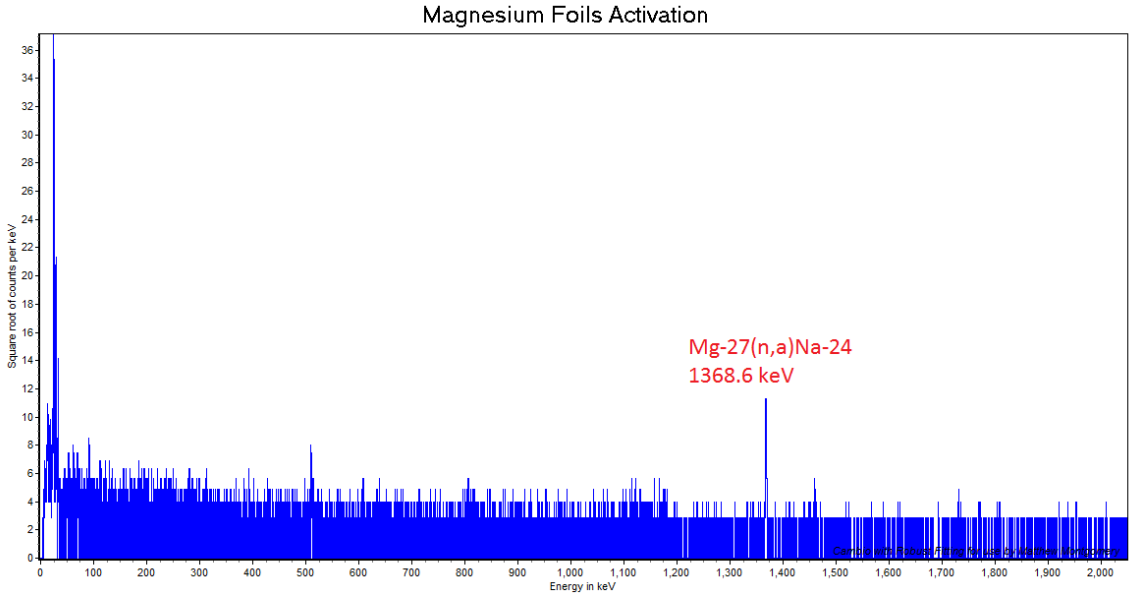

Figure 3.7: The spectral results of the irradiation trial of magnesium.

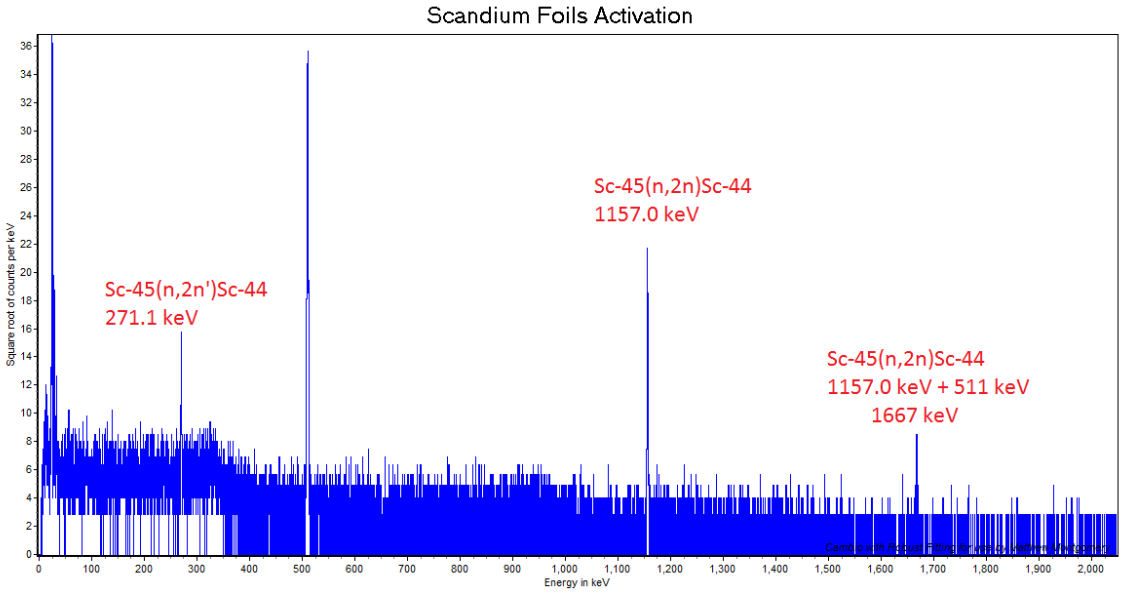

Figure 3.8: The spectral results of the irradiation trial of scandium.

Table 3.16: The irradiation, decay, and count times associated with all four irradiation trials.

Sample	Irradiation Time (s)	Decay Time (s)	Count Time (s)
Aluminum	4006.67	117.65	3600.0
Iron	3616.1	76.9	3600.0
Magnesium	3681.95	71.3	3600.0
Scandium	3922.46	85.76	3600.0

The spectral data was then processed in MAESTRO, and the response functions were extracted in order to unfold the neutron flux spectrum [35]:

Table 3.17: The analysis of the above spectral data developed using MAESTRO, and resolving the response function [σΦ] and its standard deviation for each photopeak.

Reaction	Energy (keV)	Counts	ΔCounts	XS Data?	[σΦ]	Δ [σΦ]
$^{27}Al(n,p)^{27}Mg$	843.8	3060	67	Yes	2.509E-20	5.494E-22
$^{27}Al(n,p)^{27}Mg$	1014.4	1065	60	Yes	2.428E-20	1.368E-21
$^{27}Al(n,a)^{24}Na$	1368.6	1068	57	Yes	5.391E-20	2.877E-21
$^{56}Fe(n,p)^{56}Mn$	846.7	2776	178	Yes	7.370E-20	4.726E-21
$^{56}Fe(n,p)^{56}Mn$	1810.7	363	52	Yes	4.350E-19	6.231E-20
$^{27}Mg(n, \alpha)^{24}Na$	1368.6	257	36	Yes	1.916E-19	2.684E-20
$^{45}Sc(n,2n')^{44}Sc$	271.1	287	51	No	-------	--------
$^{45}Sc(n,2n)^{44}Sc$	1157.0	750	35	Yes	5.955E-20	2.779E-21

Finally, the reaction list was populated by weighting the similar reactions by the inverse of their variance (in the case of $^{27}Al(n,p)^{27}Mg$ and $^{56}Fe(n,p)^{56}Mn$):

Table 3.18: Finalized list of response functions after weighting individual photopeaks towards common reactions (the [σΦ] vector, and the vector used to make the weighting diagonal matrix W).

Reaction	[σΦ]	Δ [σΦ]	ENDF/B-VII.1 MT#
$^{27}Al(n,p)^{27}Mg$	2.49809E-20	5.09850E-22	103
$^{27}Al(n\ \alpha,)^{24}Na$	5.39145E-20	2.87746E-21	107
$^{45}Sc(n,2n)^{44}Sc$	5.95482E-20	2.778982E-21	16
$^{56}Fe(n,p)^{56}Mn$	7.57648E-20	4.71210E-21	103
$^{24}Mg(n,p)^{24}Na$	1.91635E-19	2.68438E-20	103

Investigating the (n,p), (n,a), and (n,2n) reactions seen in the irradiation trials within the evaluated nuclear data file, there were no cross-sections available at thermal energies; these are all threshold reactions. Hence, a group structure was selected adequately spanned fast energies and was overdetermined by the dataset, as seen in Table 3.19.

Table 3.19: Group structure used with the response function to solve for the fast flux associated with the neutron generator.

Group	1	2	3
Energy Band	5 – 10 MeV	10 – 12 MeV	12 – 14 MeV

NJOY99 was then used to build cross-sections for the five reactions of interest using this three group structure, Doppler-broadened to room temperature (25C), as seen in Table 3.20.

Table 3.20: NJOY99 developed cross-sections for the five reactions of interest for each of the three energy groups, Doppler-broadened to 25C (the "Σ" matrix).

Reaction	σ_1 (cm^2)	σ_2 (cm^2)	σ_3 (cm^2)
$^{27}Al(n,p)^{27}Mg$	4.84944000E-26	8.86367000E-26	8.12102000E-26
$^{27}Al(n,\alpha)^{24}Na$	1.24749000E-26	1.02218000E-25	1.22056000E-25
$^{45}Sc(n,2n)^{44}Sc$	0.00000000E+00	6.53984000E-28	9.40837000E-26
$^{56}Fe(n,p)^{56}Mn$	1.80798000E-26	7.98439000E-26	1.11660000E-25
$^{24}Mg(n,p)^{24}Na$	2.95993000E-26	1.64851000E-25	2.01006000E-25

Lastly, the flux is solved for in the three groups with the MATLAB function "lsqnonneg", taking W*Σ and W*[σΦ] as arguments, yielding the results in Table 3.21 [36].

Table 3.21: The unfolding neutron flux spectrum associated with the 14 MeV neutron generator based on five threshold reactions.

Energy Bands	Flux ($ncm^{-2}s^{-1}$)
5 – 10 MeV	0.00E0 +/- 3.66E3
10 – 12 MeV	0.00E0 +/- 2.78E3
12 – 14 MeV	3.09E5 +/- 1.55E3

The flux was verified to be pure in nature, existing entirely in the 12 – 14 MeV energy band; the error band seems to increase with decreasing energy, which seems to suggest the over-determined fit being constrained non-negative was tenuous, yet the relative error when cast against the highest energy group is still minimal.

CONCLUSION

In summary, it was shown that the neutron generator sample position is not greatly impacted by the surrounding shielding material, at least in a negative light. In order to show this, a method was derived that used an "expected total decays" response function alongside a constrained (non-negative, weighted) least squares solution technique. Experimentally, ORIGEN2.2 was used (with custom NJOY99-derived 14MeV

one-group effective cross-sections) to scope possible reactions of interest; once candidates were identified, they were irradiated and the photopeak areas extracted using MAESTRO. After weighting the peaks by the inverse of their variance to combine similar reactions, NJOY99 was used to build cross-section libraries to elucidate on the flux profile across a fast regime (5-10 MeV, 10-12 MeV, and 12-14 MeV). Finally, the constrained least squares problem was solved using MATLAB's lsqnonneg function, returning a value of 3.08×10^5 $ncm^{-2}s^{-1}$.

This measurement is nearly a factor of two larger than the geometric attenuation flux described in the "Motivation" section of this chapter. Further work could be done to clarify as to why—whether or not this discrepancy is due to the surrounding materials working as an elastic reflector or a large variance in the quoted '$\sim 10^8$ neutrons/second' from the neutron generator manual. An enhanced group structure, specifically from 12 – 14 MeV, with many more activation trials would also be an interesting follow-up to this work.

Chapter 4: 14 MeV Fission Product Determination

MOTIVATION

With a functional automated, cyclic fast pneumatic system and a well-characterized flux, the last step that must be conducted prior to cyclic fission studies can occur is a mechanism by which one can predict fission product distributions in an irradiated sample.

Currently, 1247 nuclides exist in the ENDF-B/VII.1 database with fission yields for ^{235}U; for each of these nuclides, there are both independent and cumulative yields, and those specifically are further split into energy bands of thermal (0.0253 ev), fission (500 keV), and fast (14 MeV). When performing gamma spectroscopy on even irradiated pure elemental samples and the difficulty of identifying photopeaks due to sum and escape effects in them, fission product identification is easily a factor of a hundred more difficult due to the sheer number of different isotopics that could form in the sample, as well as their decay chains leading into wholly different isotopics.

Given the possibility of over a thousand isotopes appearing in the fissioned sample, and the possibility that dozens of gamma rays may be attributed to a single isotope, a code must be developed to reliably and efficiently predict what to expect given experimental parameters.

METHOD OF SOLUTION

In order to parse spectra and see specific gamma ray signatures of isotopes, a library of all known gamma rays was built from Nuclear Data Sheets (ENSDF) [37]. Then, this library was parsed to contain only those nuclides with yields described in the Evaluated Nuclear Data File (ENDF-B/VII.1). This new list of gamma rays and their

parent isotopes was then combined with each isotope's respective cumulative and independent yield, for all three energy bands (thermal, fission, and fast). Lastly, the decay constant for each and every possibly fission product is appended into the library. This library now contains all relevant information necessary to solve for an expected counts similar to that used in the flux characterization:

$$C = \frac{N\sigma_f \phi \varepsilon \gamma Y}{\lambda}\left(1 - e^{-\lambda t_i}\right)e^{-\lambda t_d}\left(1 - e^{-\lambda t_c}\right) \tag{4.1}$$

with: C = total counts observed in a given photopeak (counts)

N = total number of fissile ^{235}U atoms (atoms)

σ_f = cross-section for fission (cm^{-2})

ϕ = neutron flux (ncm^{-2}s^{-1})

Ɛ = efficiency of the detector for the given photopeak energy (fractional)

Y = nuclide-specific yield (fractional)

γ = absolute intensity of given photopeak (fractional)

λ = decay constant [ln(2) / half-life] (seconds^{-1})

t_i = irradiation time (seconds)

t_d = decay time (seconds)

t_c = count time (seconds)

The major limitation of applying this equation to fission is that, as described above, it considers each isotope in isolation: there is no production of any isotope outside of creation from fission when, in fact, the mass chains of nearly all the isotopics are coupled systems with streaming in and out. This limitation requires the code to be used as a scoping mechanism and a tool to post-process spectra to identify peaks only. The

possibility does exist, however, to more adequately describe the physics by adding decay chains and branching ratios to the library created, and numerically stepping the differential equation describing the production and decay of isotopes forward in time to solve for the properly coupled isotopes in mass chains. However, to that end, a readily available depletion code such as ORIGEN2.2 or ORIGEN-S could be adapted and the output parsed to calculate gamma ray emission rates.

Given an equation that serves as a first order approximation for the behavior, a python script was written to iterate over the full library and, for each gamma emission, solve for the total counts expected in a given photopeak. The inputs into the code are: target mass, neutron flux energy (coinciding with available yields – 0.0253 eV, 500 keV, or 14 MeV), neutron flux, yield type (cumulative or independent), irradiation time, decay time, count time, a scale factor (for any other constant multiplier correction), and a low level discriminator to filter out photopeaks less than the stated total counts. A high purity germanium detector efficiency is used, but can be edited simply in the code. Depending on the flux energy chosen, a one-group cross-section for fission is automatically used (507 b for 0.0253 eV, 1.5 b for 500 keV, 2 b for 14 MeV). In our case, we would use the 14 MeV cross-section, but the option is available for thermal or epithermal energies. The output consists of three files – the cumulated list of photopeaks sorted by isotope, by energy, or by total size.

Finally, a GUI was constructed in LabView for ease of use, shown in Figs. 4.1 & 4.2.

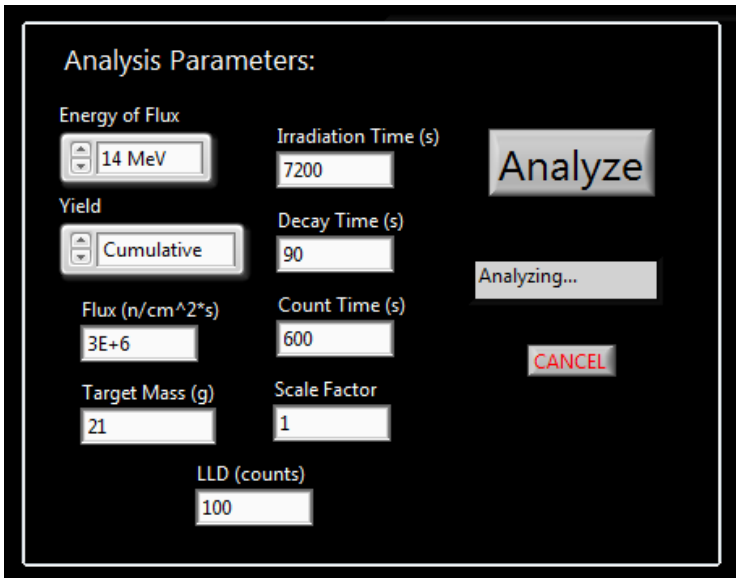

Figure 4.1: LabView GUI (input) to solve for expected counts in photopeaks of fission products.

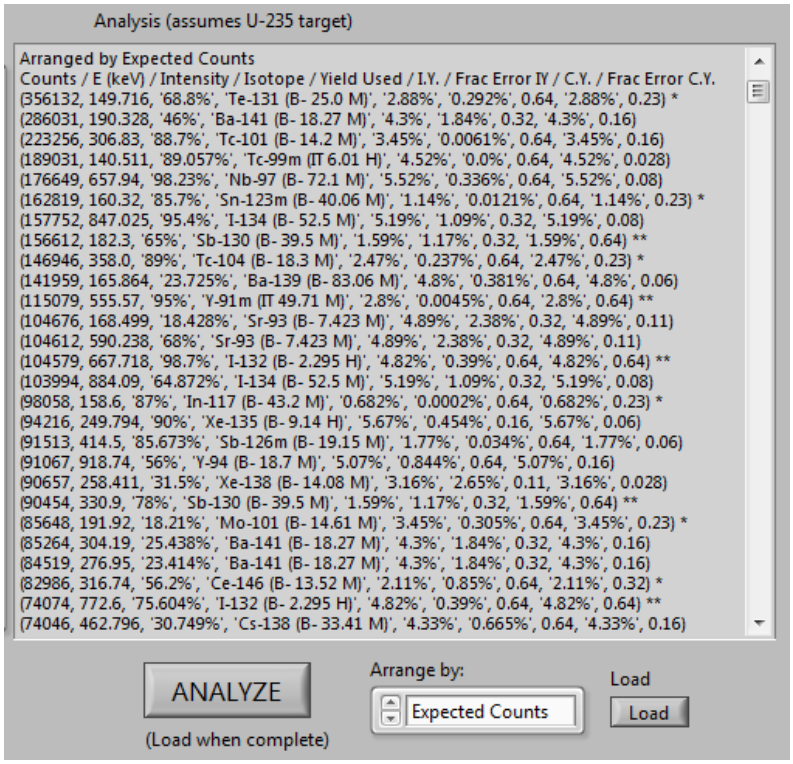

Figure 4.2: LabView GUI (output) to solve for expected counts in photopeaks of fission products.

With the LabView frontend to the Python script that iterates over the full library of gamma emissions for all known fission products available, it is now possible to irradiate a sample of fissile material and solve for every observed photopeak in the spectrum.

EXPERIMENTAL MEASUREMENT OF FISSION PRODUCTS

Figure 4.3: Uranium samples used to determine fission products. Top left, natural uranium ore (U_3O_8) - 0.952g. Middle left, enriched (63%) uranium ore (U_3O_8) - 0.376g. Bottom left, shredded HEU (93%) foil- 0.668g. Right, 4x HEU (93%) foils- 21.122g.

After failing to see fission products with samples of varying ^{235}U content (natural uranium ore, 63% enriched ore, and a 93% enriched HEU foil) all less than 1 g in mass due to a low flux (3 x10^5 ncm^{-2}s^{-1}), a larger quantity of 93% enriched HEU (21.122 g) in

the form of four foils (jarred in Figure 4.3) was used. Table 4.1 sums up the irradiation experiment details.

Table 4.1: Parameters of fission product determination experiment.

Experimental Parameters	
Sample Mass	21.122 grams
Sample Enrichment	93%
Detector Dead Time Pre-Activation	17.01%
Detector Dead Time Post-Activation	26.18%
Estimated 14 MeV Neutron Flux	3E5 $ncm^{-2}s^{-1}$
Irradiation Time	2:12:16.00 (7936.00 seconds)
Decay Time	2:11.79 (131.79 seconds)
Count Time	3802.667 s (live time); 5151.573 s (real time)

The following twelve figures document the results of the irradiation. The first figure is the total unactivated spectrum (red) and the total resultant spectrum (blue), followed by a figure denoting the live-time matched, background subtracted spectrum. The last ten are the resultant activated spectrum (blue) cast against the unactivated spectrum (red), live-time matched, in 200 keV intervals. Given the number of photopeaks native to the unactivated spectrum, this method of comparison was necessary to clearly identify what was created in fission versus what was already present, either in the form of the uranium decay series or prior activations.

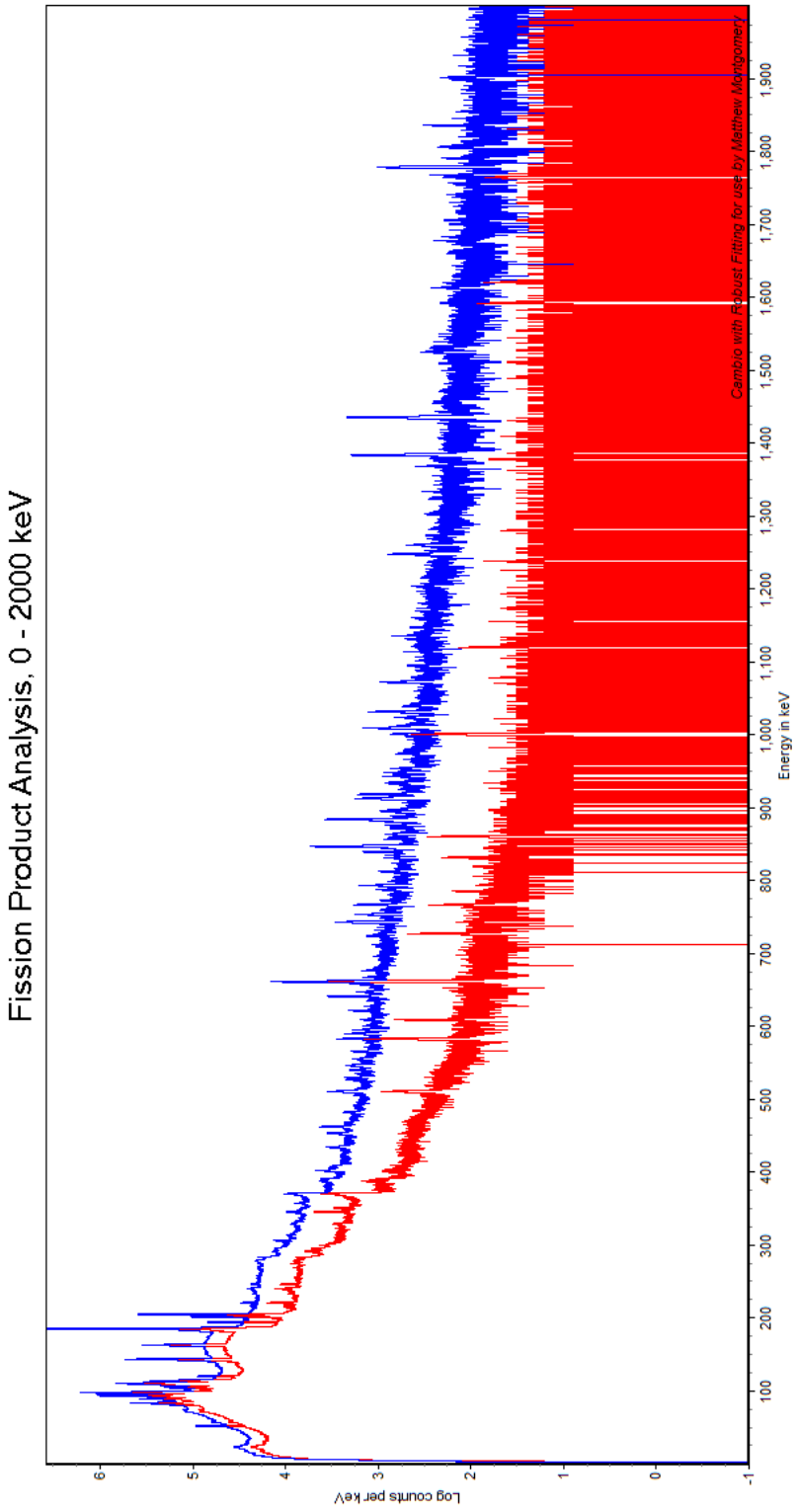

Figure 4.4: Activated (blue) vs. Unactivated (red) HEU spectrum, 0-2000 keV.

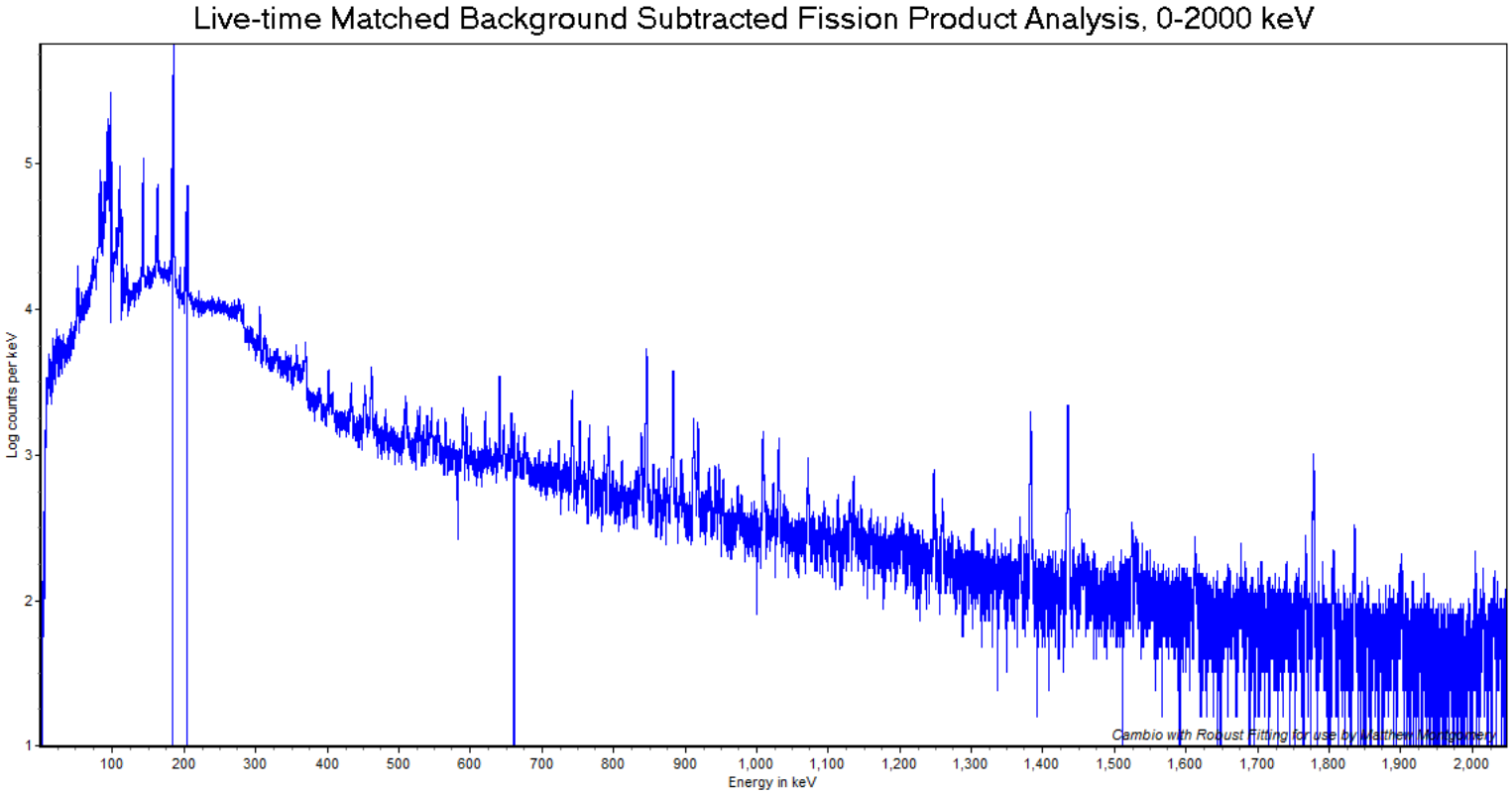

Figure 4.5: Live-time matched, background subtracted fission product spectrum, 0-2000 keV.

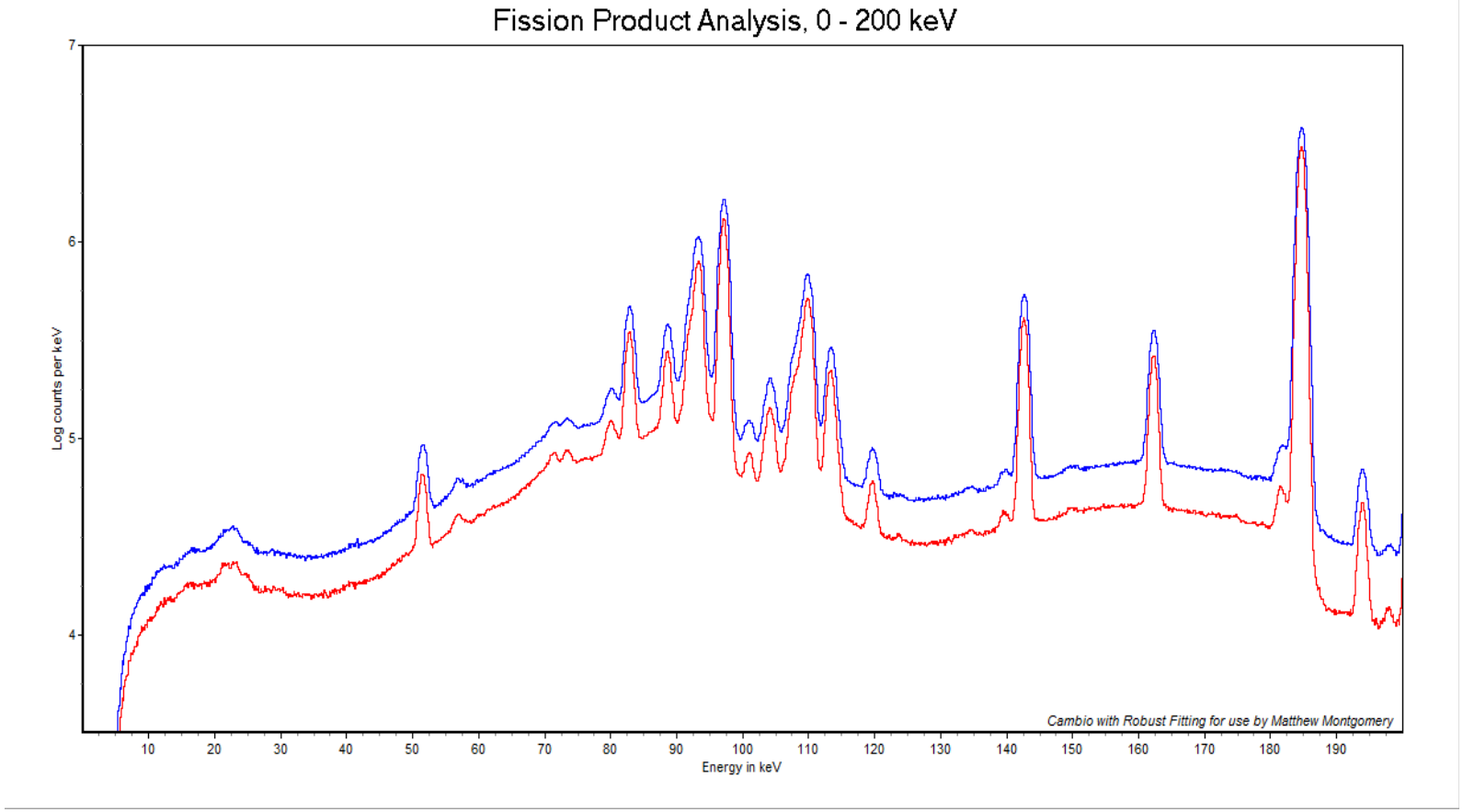

Figure 4.6: Activated (blue) vs. Unactivated (red) HEU spectrum, 0-200 keV.

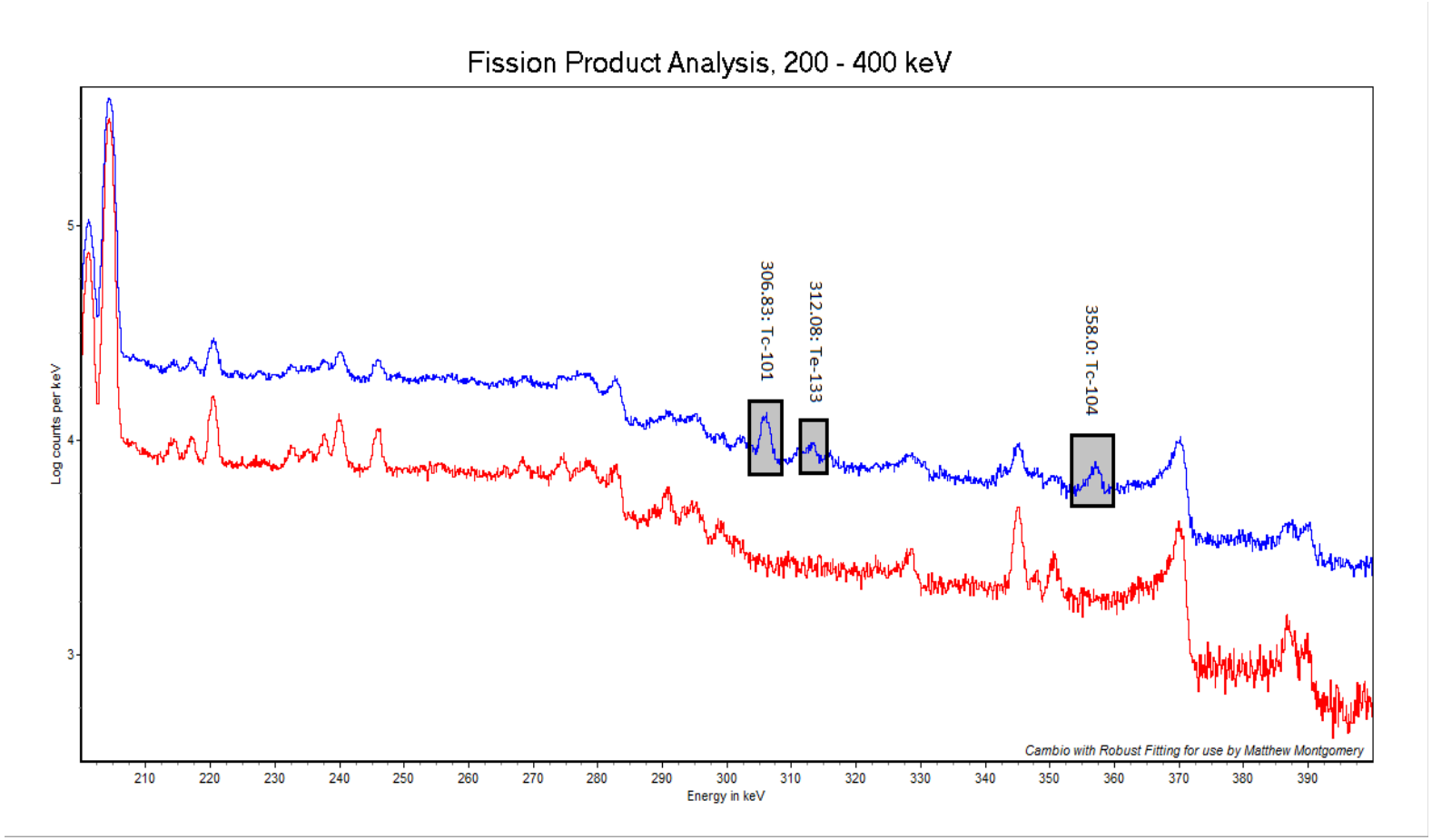

Figure 4.7: Activated (blue) vs. Unactivated (red) HEU spectrum, 200-400 keV.

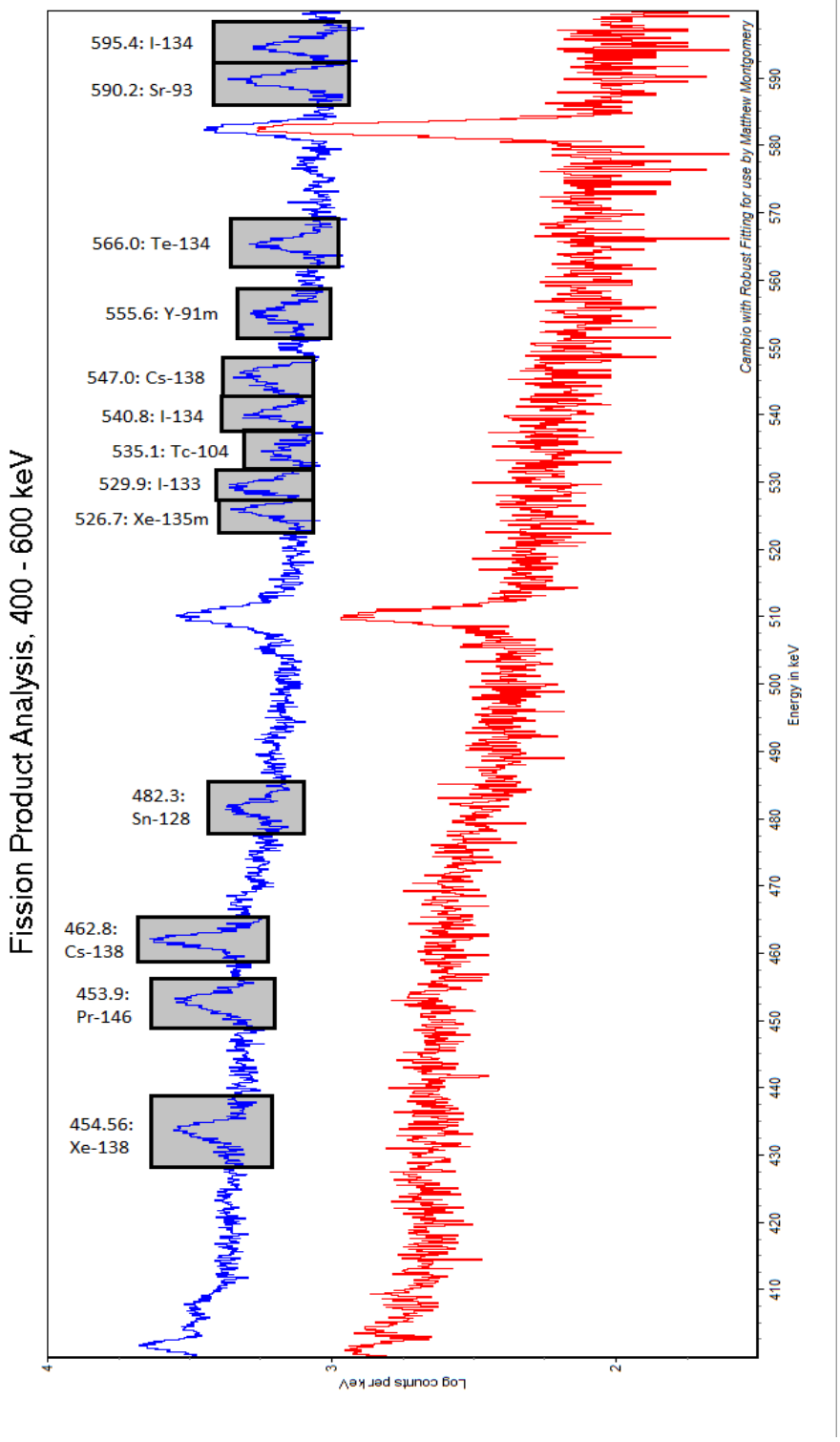

Figure 4.8: Activated (blue) vs. Unactivated (red) HEU spectrum, 400-600 keV.

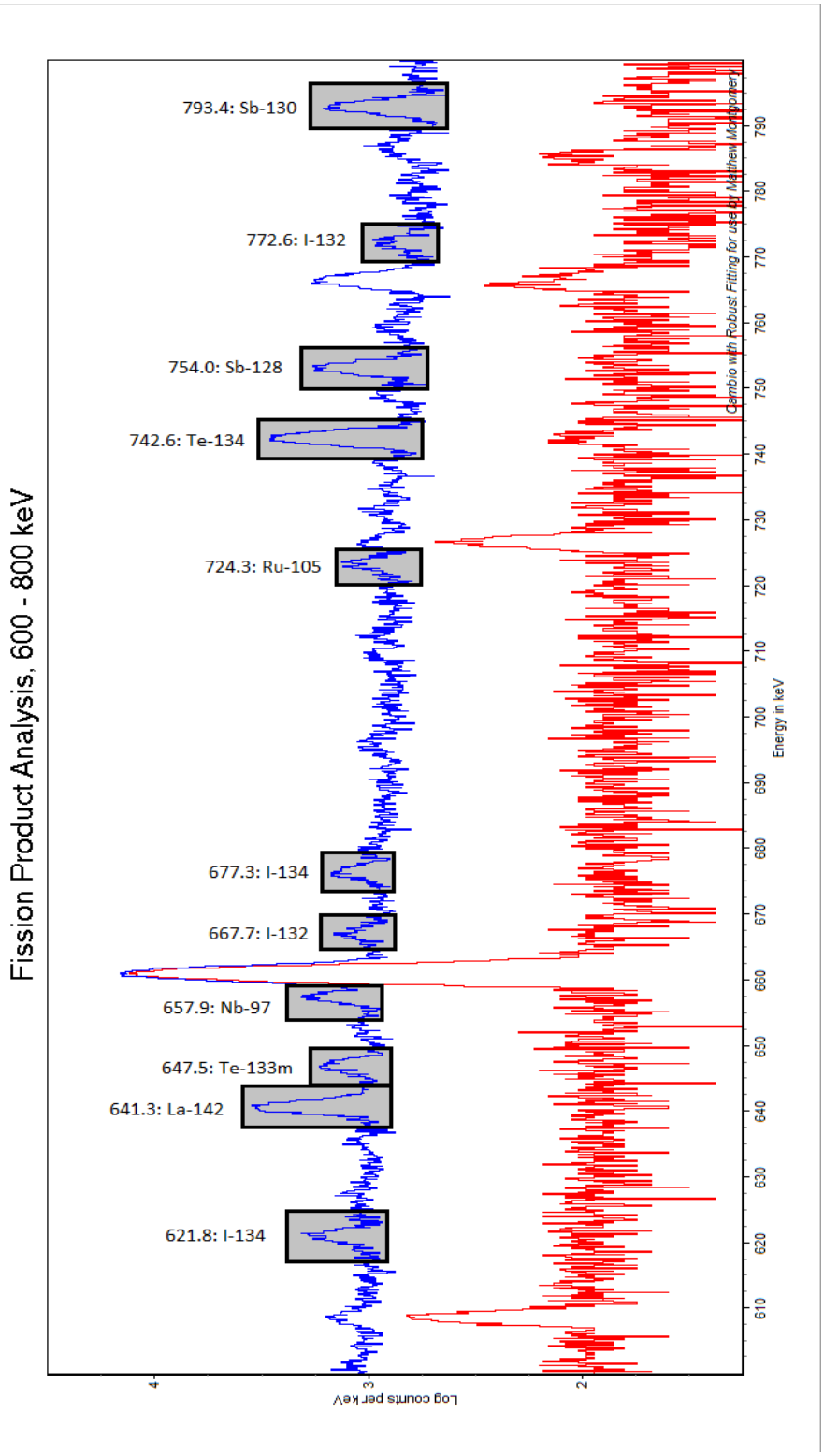

Figure 4.9: Activated (blue) vs. Unactivated (red) HEU spectrum, 600-800 keV.

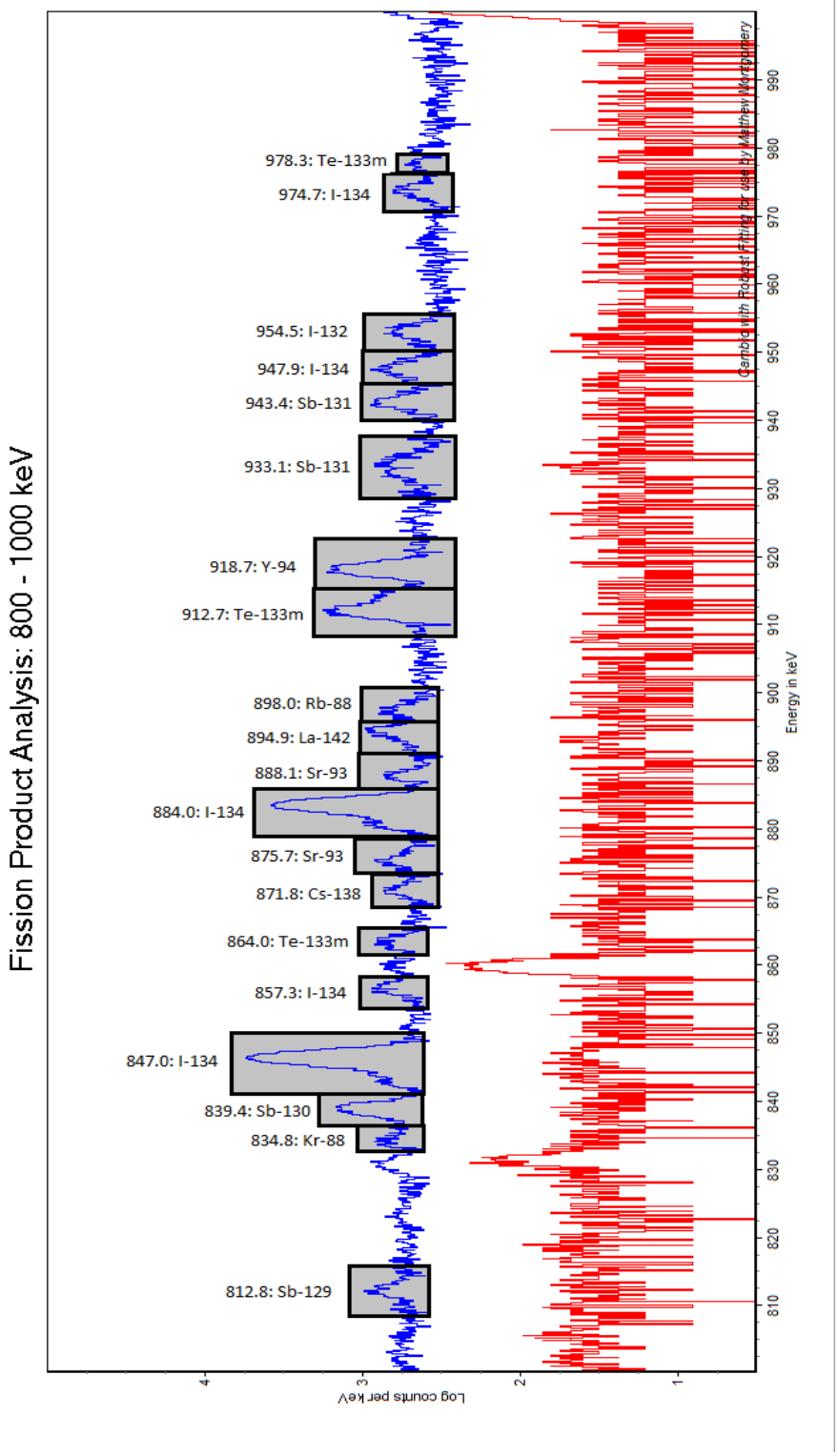

Figure 4.10: Activated (blue) vs. Unactivated (red) HEU spectrum, 800-1000 keV.

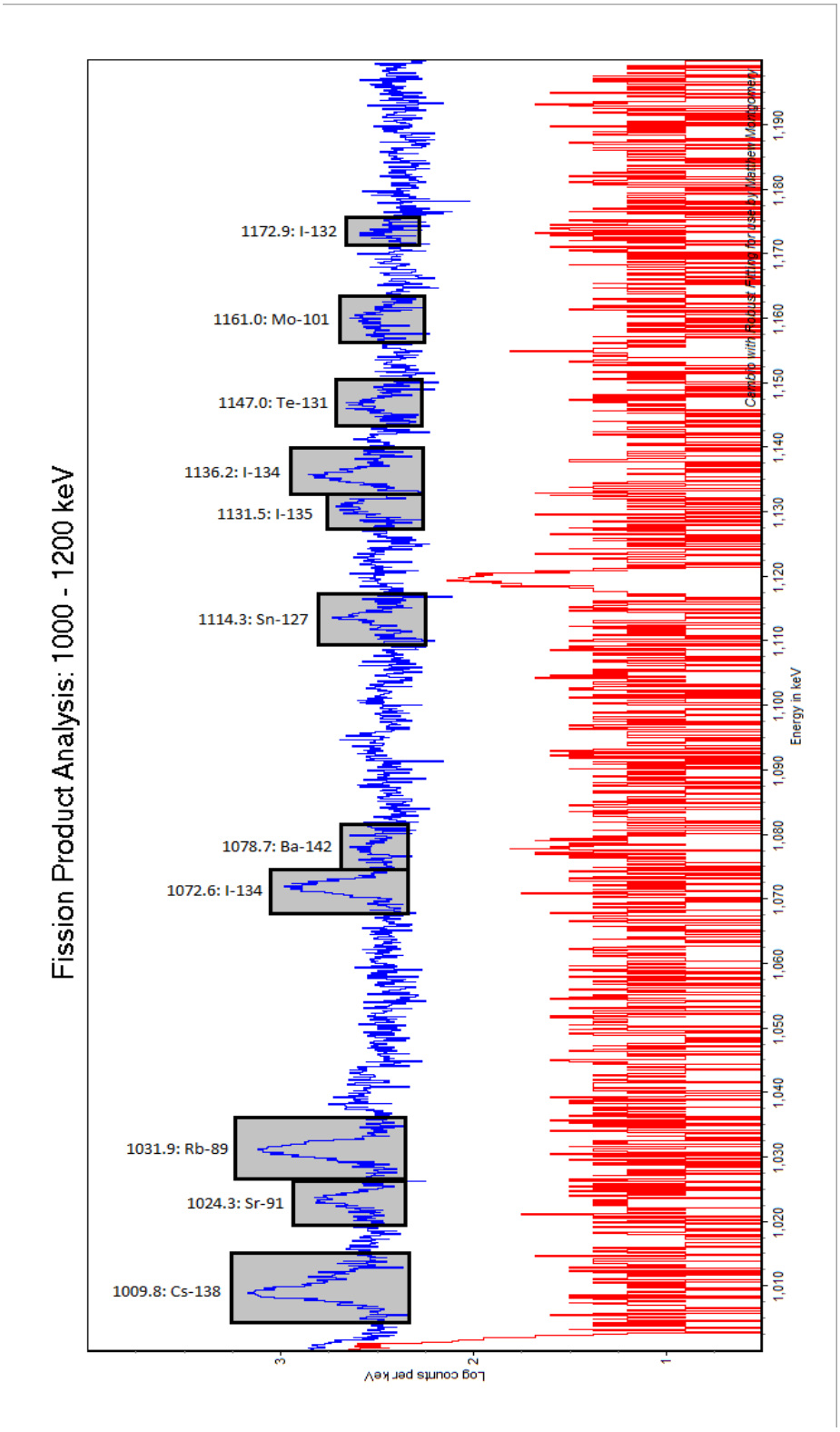

Figure 4.11: Activated (blue) vs. Unactivated (red) HEU spectrum, 1000-1200 keV.

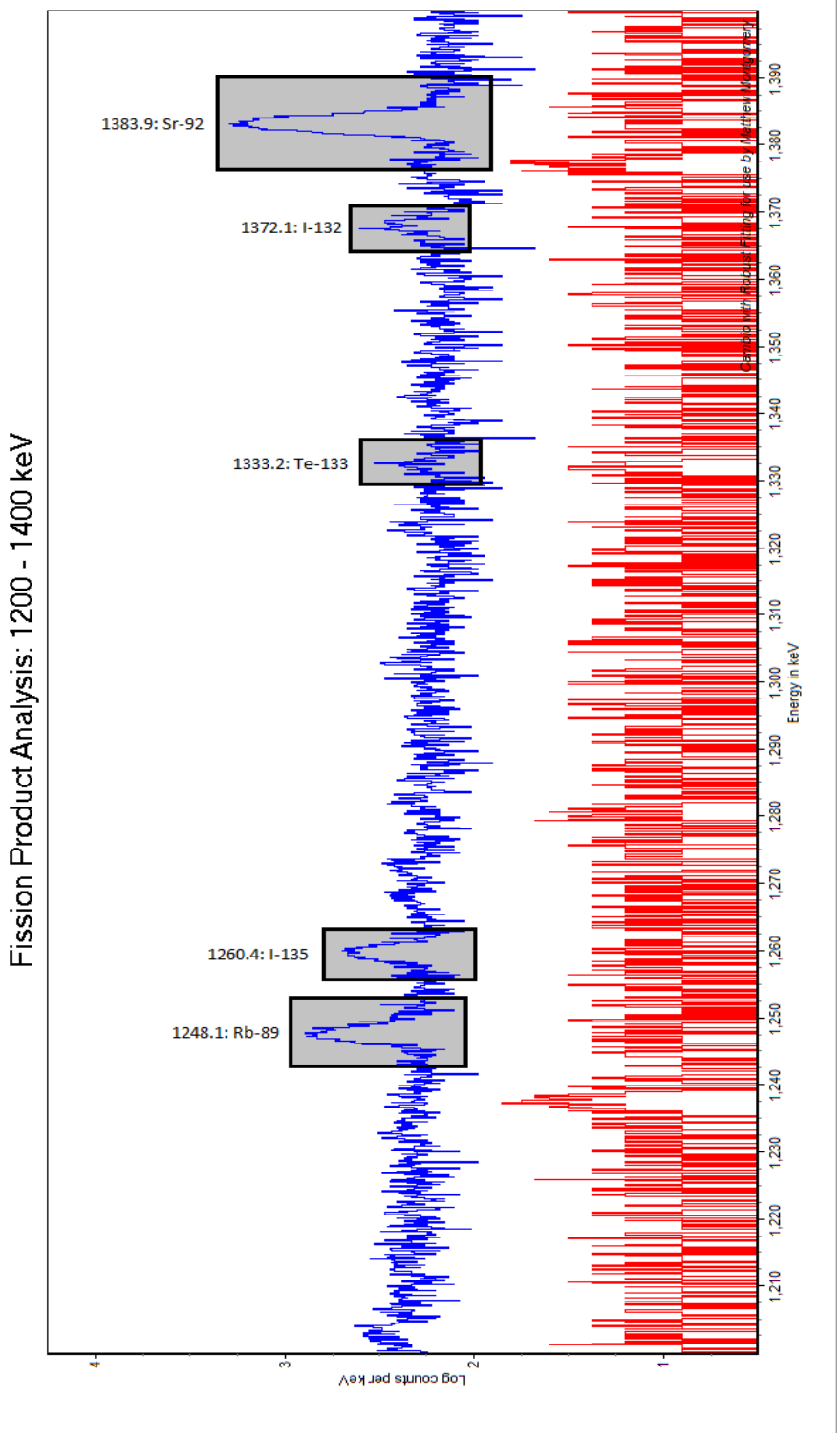

Figure 4.12: Activated (blue) vs. Unactivated (red) HEU spectrum, 1200-1400 keV.

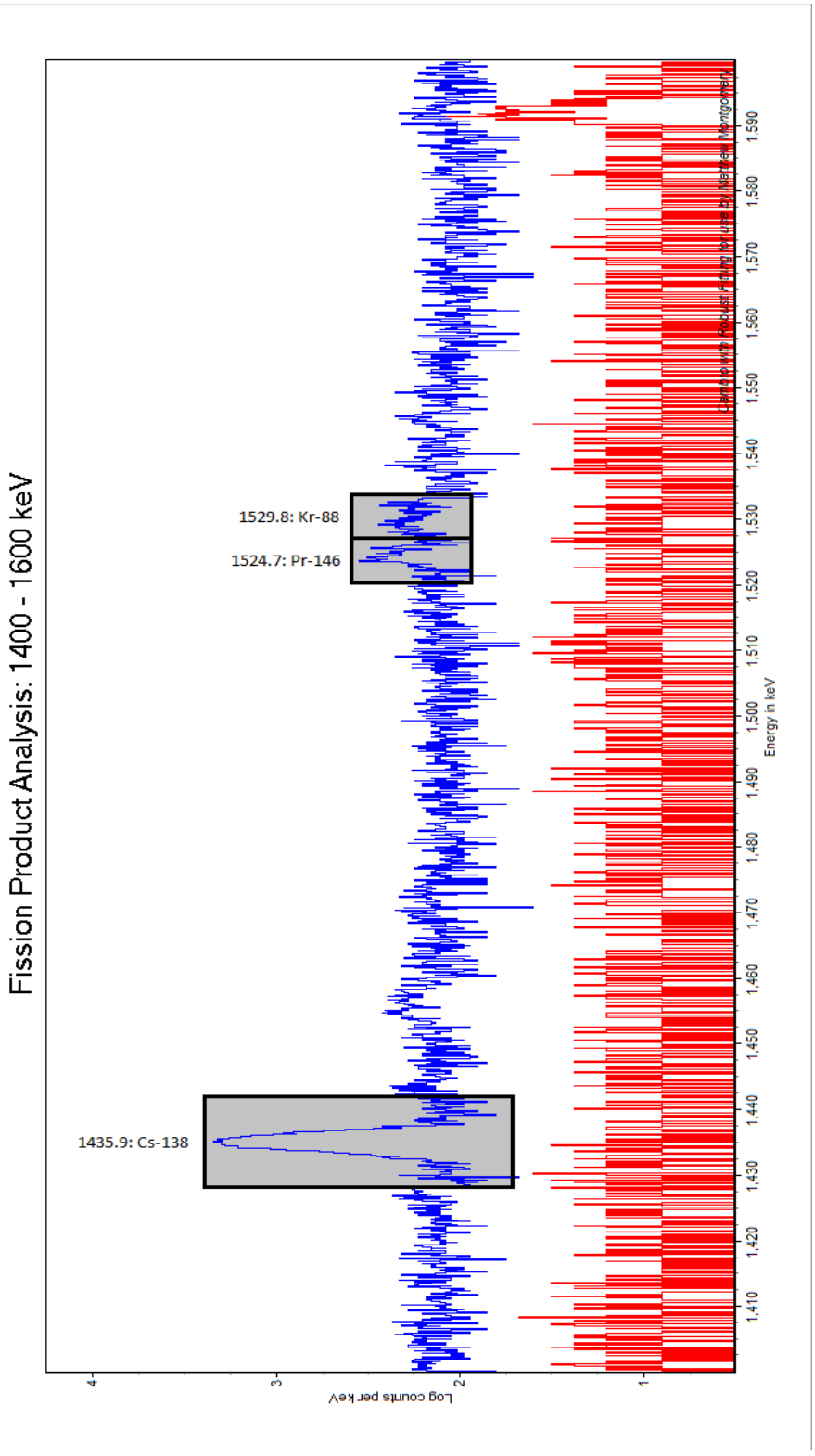

Figure 4.13: Activated (blue) vs. Unactivated (red) HEU spectrum, 1400-1600 keV.

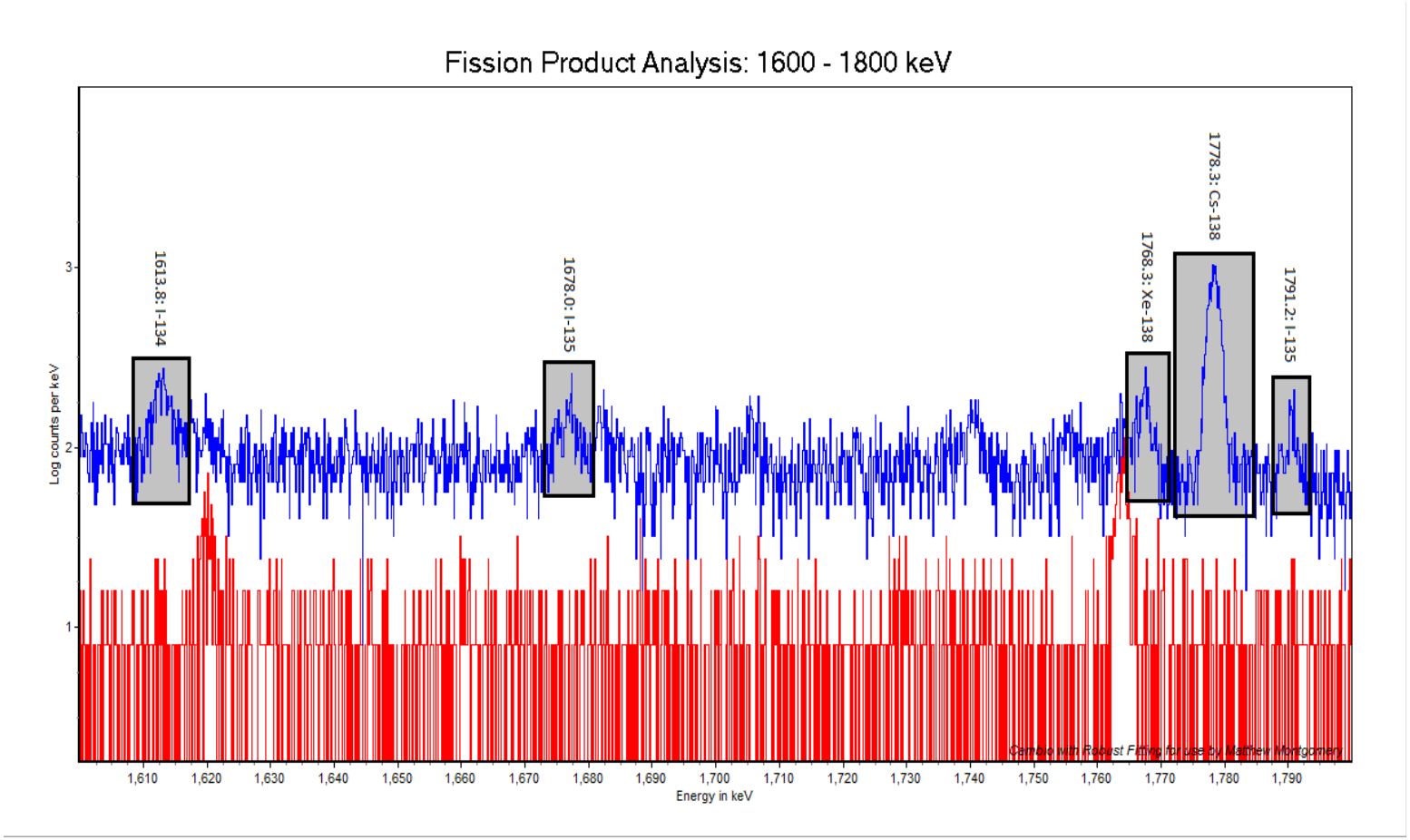

Figure 4.14: Activated (blue) vs. Unactivated (red) HEU spectrum, 1600-1800 keV.

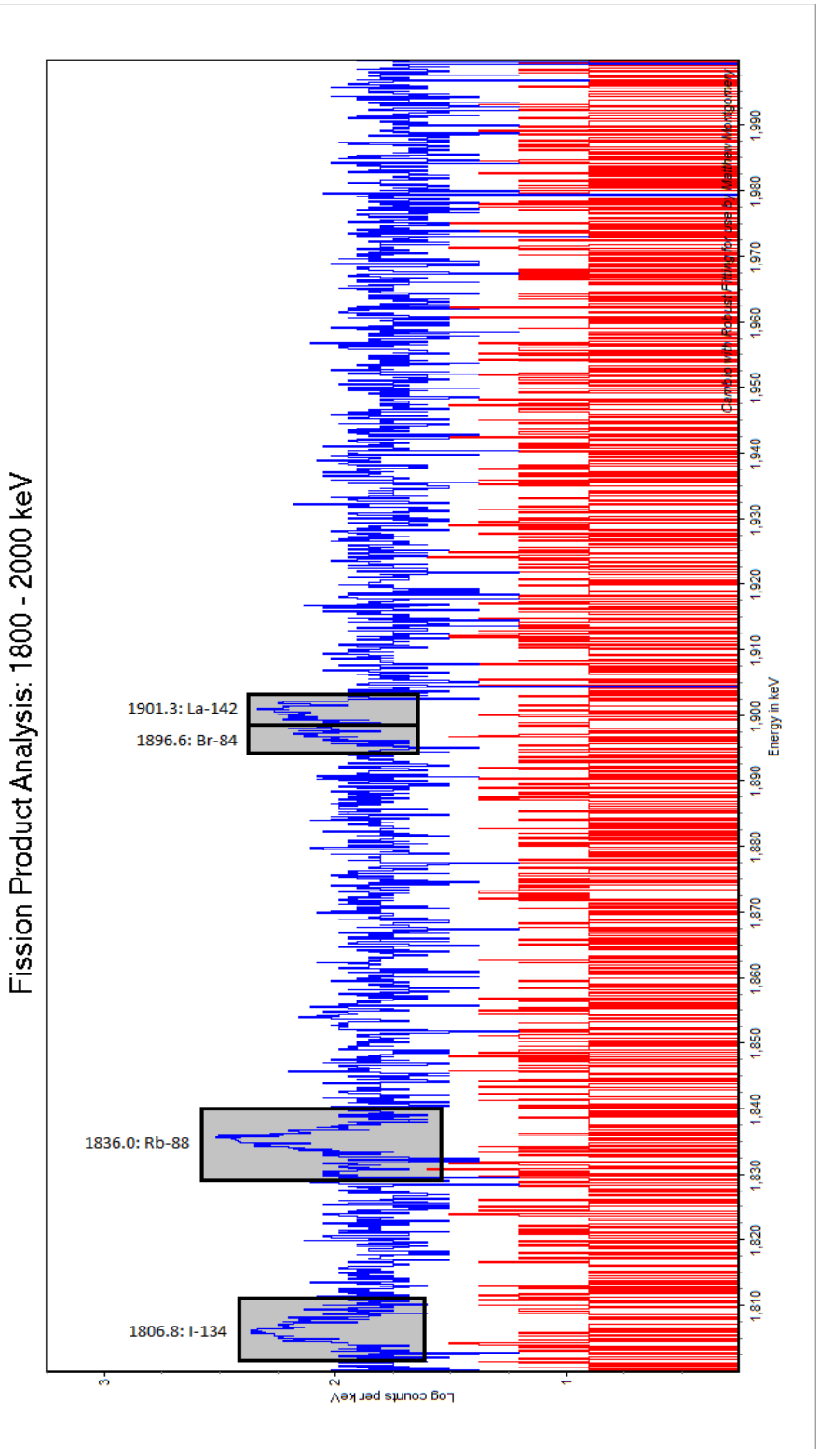

Figure 4.15: Activated (blue) vs. Unactivated (red) HEU spectrum, 1800-2000 keV.

Seventy-four photopeaks were observed, corresponding to thirty-four isotopes:

Table 4.2: Fission products identified after 14 MeV irradiation.

Isotope	Energy (keV)	Isotope	Energy (keV)
^{142}Ba	1078.7	^{130}Sb	793.4, 839.4
^{84}Br	1896.6	^{131}Sb	933.1, 943.4
^{138}Cs	462.8, 547, 871.8, 1009.8, 1435.9, 1778.3	^{127}Sn	1114.3
^{132}I	667.7, 772.6, 954.5, 1172.9, 1372.1	^{128}Sn	482.3
^{133}I	529.9	^{91}Sr	1024.3
^{134}I	540.8, 595.4, 621.8, 677.3, 847, 857.3, 884, 947.9, 1136.2, 1613.8, 1806.8	^{92}Sr	1383.9
^{135}I	1131.5, 1260.4, 1678, 1791.2	^{93}Sr	590.2, 875.7, 888.1
^{88}Kr	834.8, 1529.8	^{101}Tc	306.8
^{142}La	641.3, 894.9, 1901.3	^{104}Tc	358, 535.1
^{101}Mo	1161	^{131}Te	1147
^{97}Nb	657.9	^{133}Te	213.1, 1333.2
^{146}Pr	453.9, 1524.7	^{133m}Te	647.5, 864, 912.7, 978.3
^{88}Rb	898, 1836	^{134}Te	566, 742.6
^{89}Rb	1031.9, 1248.1	^{135m}Xe	526.7
^{105}Ru	724.3	^{138}Xe	454.6, 1768.3
^{128}Sb	754	^{91m}Y	555.6
^{129}Sb	812.8	^{94}Y	918.7

CONCLUSION

The one-dimensional fission product identification code provided a rational solution for every unknown peak above the unactivated spectrum with relatively good fit when examining both the independent and cumulative yields with a given irradiation, decay, and count time, which implies that the isolated 1-D expected total counts expression captures the physics fairly well. It should not be used as a quantitative model, and a matrix exponential approach, such as that taken by ORIGEN2, should be used in a more refined approach.

This experiment showed the definitive creation of fission products using NETL's neutron generator, and thus a proof-of-concept to proceed with a cyclic irradiation / measurement scheme.

Chapter 5: Conclusion

The culmination of the previous three chapters is this:

- Circuitry and control mechanisms were developed in order to create a functional automated, cyclic fast pneumatic system capable of a sub-second transit time to study short-lived neutron-activated isotopics from a mechanical prototype.
- A neutron flux characterization was carried out, first by scoping the experiment with ORIGEN2.2, then by proceeding to irradiate a series of foils and unfolding the flux spectrum using weighted non-negative least squares; this verified a flux of 3×10^5 $ncm^{-2}s^{-1}$ at an energy between 12 & 14 MeV.
- In order to demonstrate applicability to fission product yield calculations, a Python script was written to iterate over all gamma emissions from all fission products and tabulate their likelihood of appearing as counts in an irradiated sample, given yield, efficiency, and decay constant; performing an irradiation of an HEU foil, this script was used to identify each and every photopeak seen in the activated sample.

The fission yields can now be pursued with the automatic, cyclic fast pneumatic system; further work would see them solved for with a high degree of precision. Other work could include the integration of a second detector in order to perform coincidence and the conversion of these two detectors from normal data acquisition to list-mode data acquisition to refine the timing down to hundreds of nanoseconds.

Appendix A: Thermo MP320 D-T Neutron Generator Technical Sheet

The following is the specification sheet taking from "Appendix A: Specifications" of the Thermo Electron Corporation MP320 Neutron Generator user manual.

Parameter	***Spec***	***Comments***
Power		
Input:	24V @ 2-5A or 100-240VAC 50 – 60 Hz	Typically 2-3Amps
Generator		
Neutron Output:	~$1x10^8$ N/s	Typical at 80kV (with 60μA of beam current)
High Voltage	40-90kV	Limited in software to 90kV
Beam Current	20-70μA	Limited in software to 90μA
Turn Off Time	<1μsec	
Temperature	-25C to +50C	
Weight	25 Lbs (Integrated Configuration)	
Source		
Frequency:	250Hz to 20kHz	
Duty Cycle:	5% to continuous (100%)	5uS minimum pulse width
Interlock		
Interlock Current	50mA max	Internally limited to protect operation during short circuit
Neutron Lamp		
Voltage Out	+24V (same as input)	Protected to take continuous short circuit
Max Current	2A	
Neutron Lamp Relay – Spare Contacts		
Max Switched Voltage	250VDC,230VAC	
Max Switched Power	60WDC or 120VAC, resistive load	
Max Switched Current	2A	
Tube		
SF6 Pressure	140psi maximum, 120psi nominal, 80psi min.	Software warning at 100psi

Appendix B: Fast Pneumatic System Mechanical Drawings

The following drafted works were created as part of the design phase of the fast pneumatic system by the undergraduate team of Kendall Burns, Janet Fuchs, Jason Guidry, and Michael Yoho.

SAMPLE LOADER

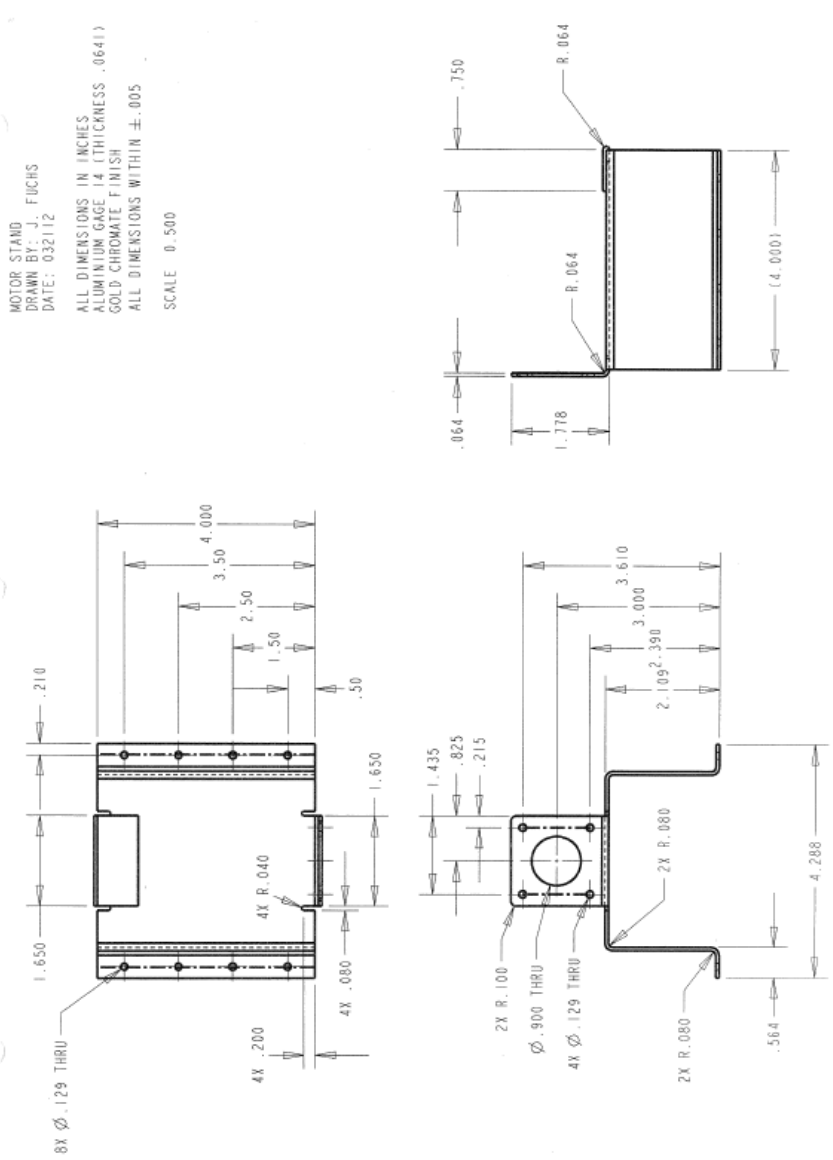

SCALE 1:2
MATERIAL: ALUMINUM 6061

LANL TRANSFER_BASE
Michael D. Yoho
mdyoho@utexas.edu

2 NEEDED

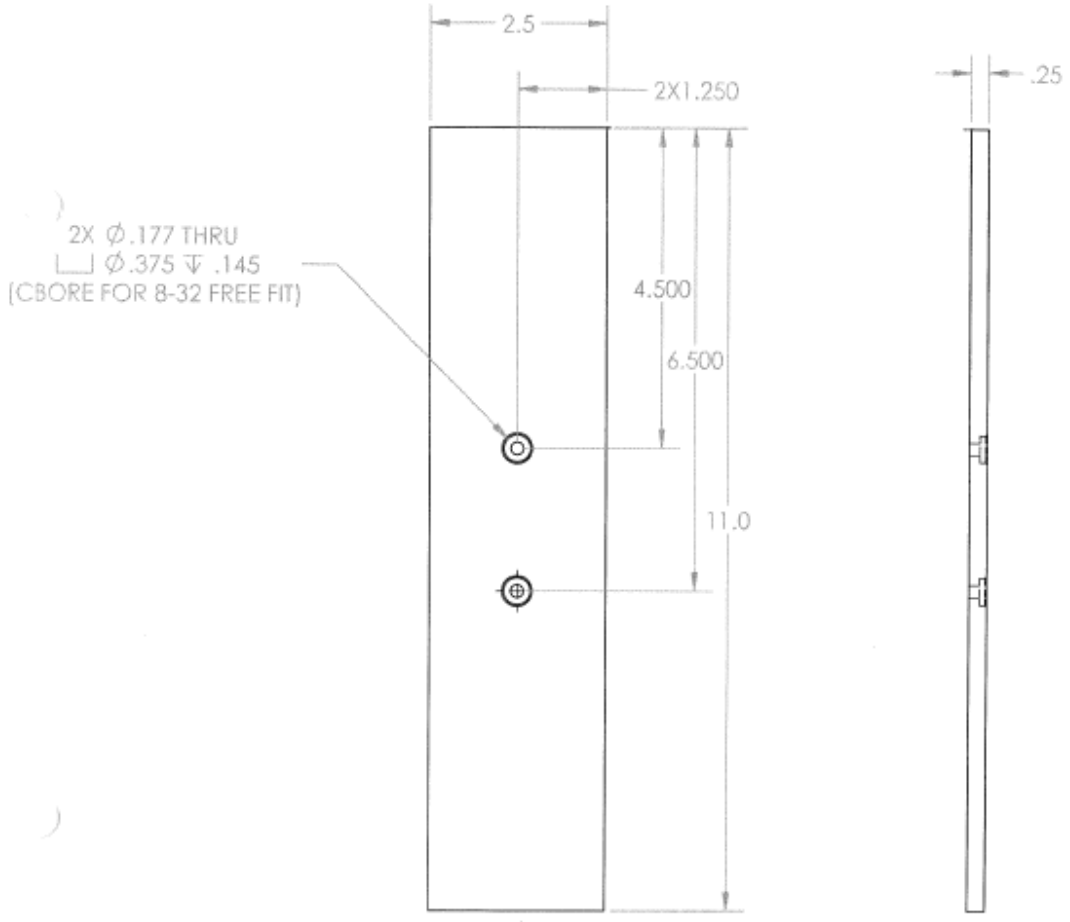

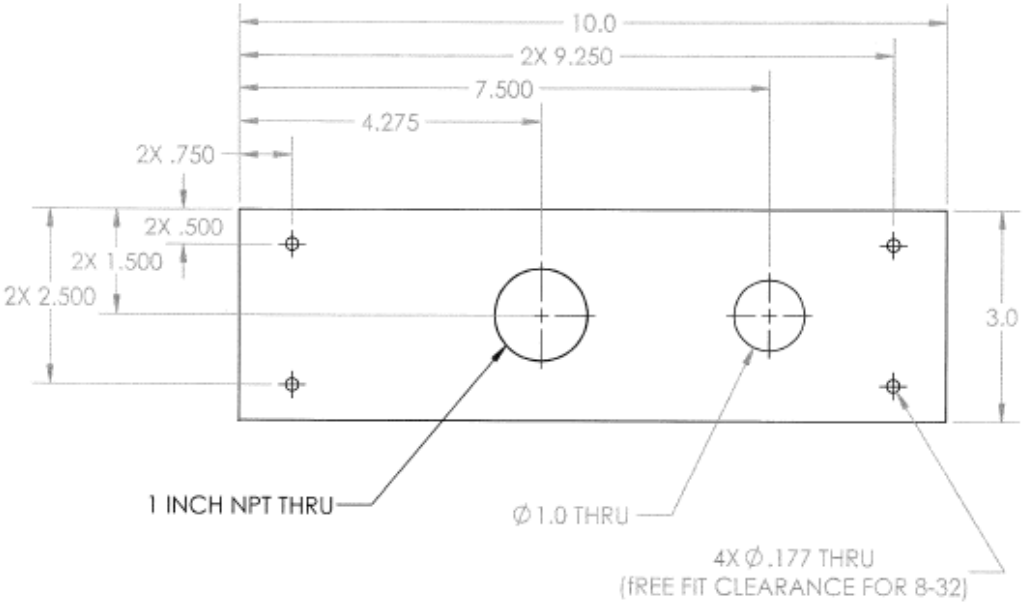

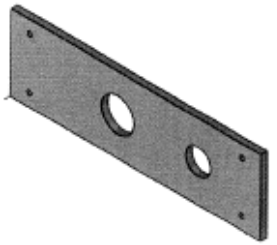

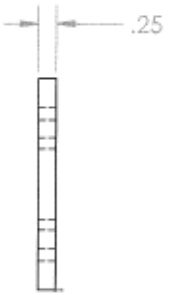

SCALE 1:2
MATERIAL: ALUMINUM 6061

LANL TRANSFER_TOP PLATE
Michael D. Yoho
mdyoho@utexas.edu
910 476 3087

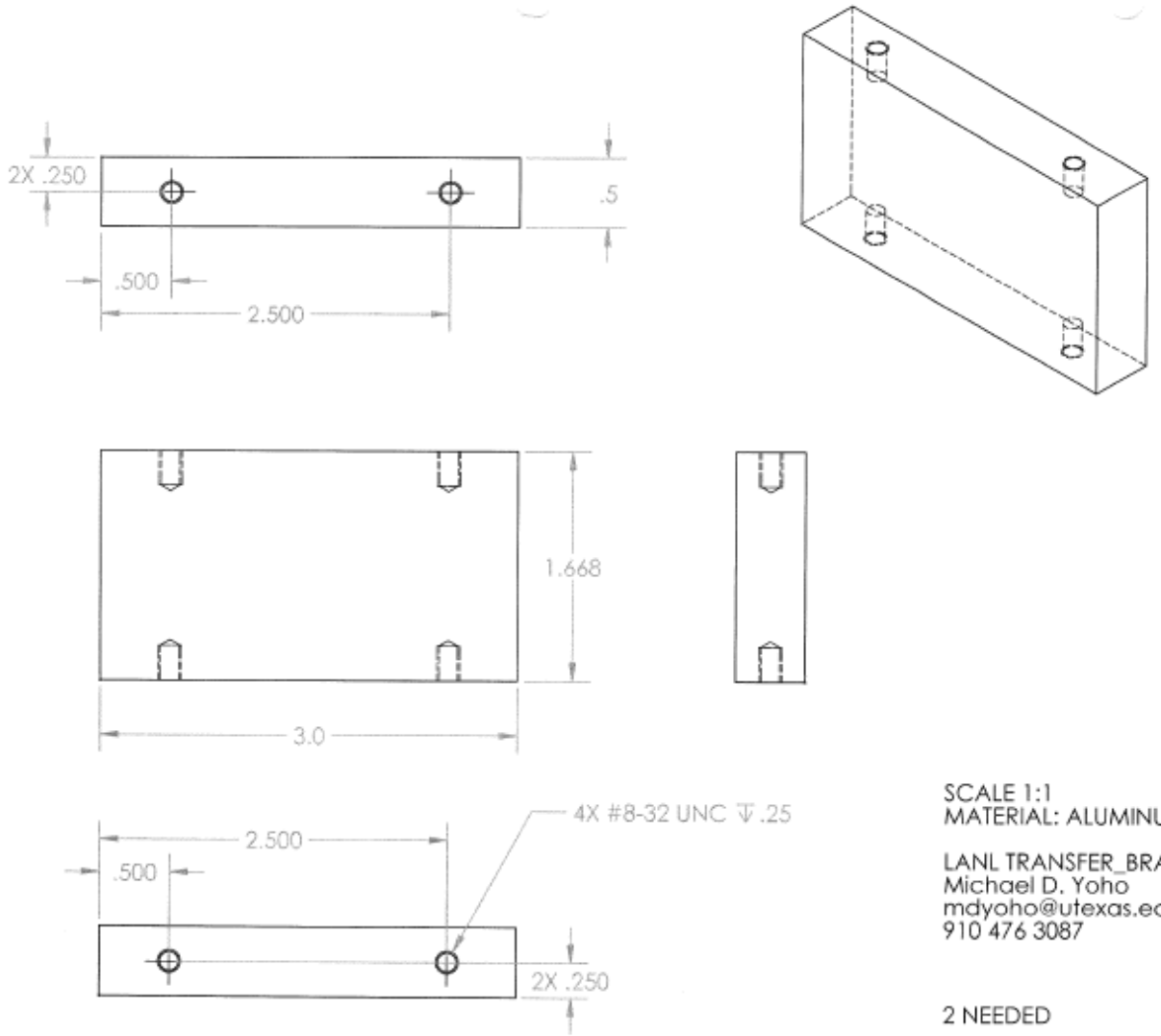

SCALE 1:1
MATERIAL: ALUMINUM 6061

LANL TRANSFER_BRACKET
Michael D. Yoho
mdyoho@utexas.edu
910 476 3087

2 NEEDED

ITEM 3

Front View

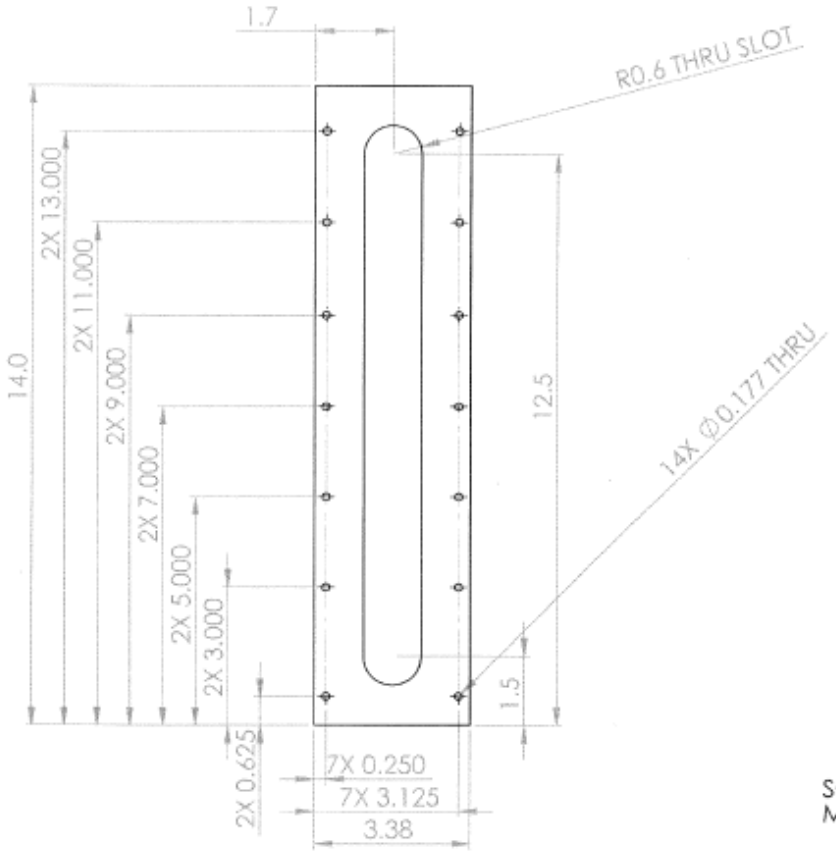

Side View

SCALE: 1:3
MATERIAL: ALUMINUM 6061

K-LANL Transfer_ Hopper Front Plate
Michael D. Yoho 910 476-3087
mdyoho@utexas.edu

ITEM 2
Side view
0.125
SCALE 2:5
MATERIAL: ALUMINUM
K-LANL Transfer_ Hopper Back Plate
Michael D. Yoho 910 476-3087
mdyoho@utexas.edu
Front view
14X Φ.177 THRU
2X 13.000
2X 11.000
2X 9.000
2X 7.000
2X 5.000
2X 3.000
2X 0.625
3.38
7X 3.125
7X 0.250
14.0

Front View

Side View

ITEM: 1
QUANTITY: 2

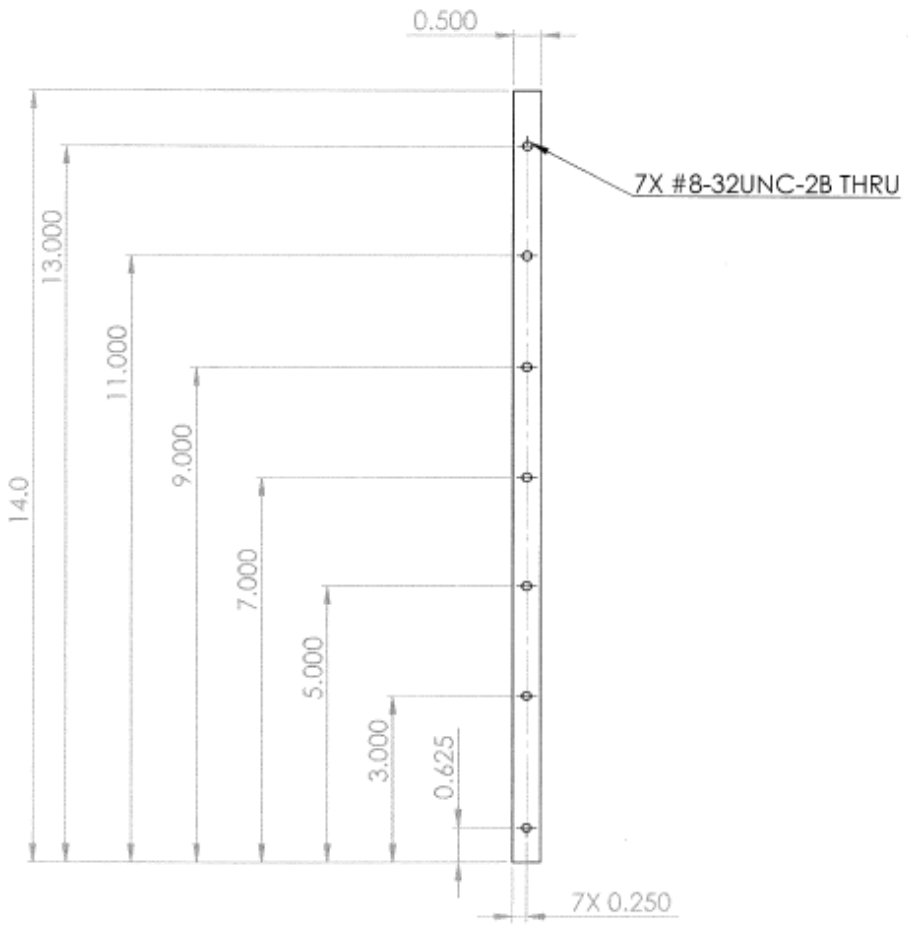

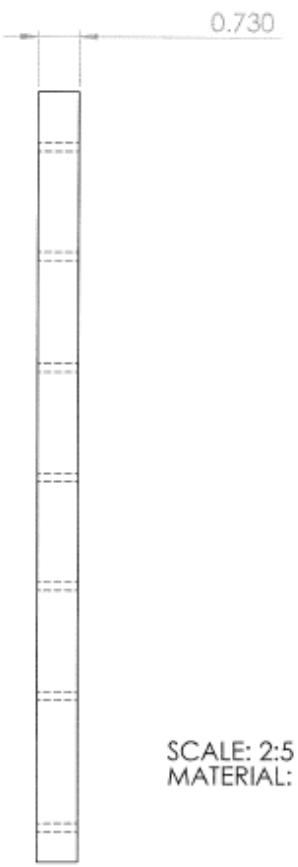

SCALE: 2:5
MATERIAL: ALUMINUM

K-LANL Transfer_ HOPPER BRACE
Michael D. Yoho 910 476-3087
mdyoho@utexas.edu

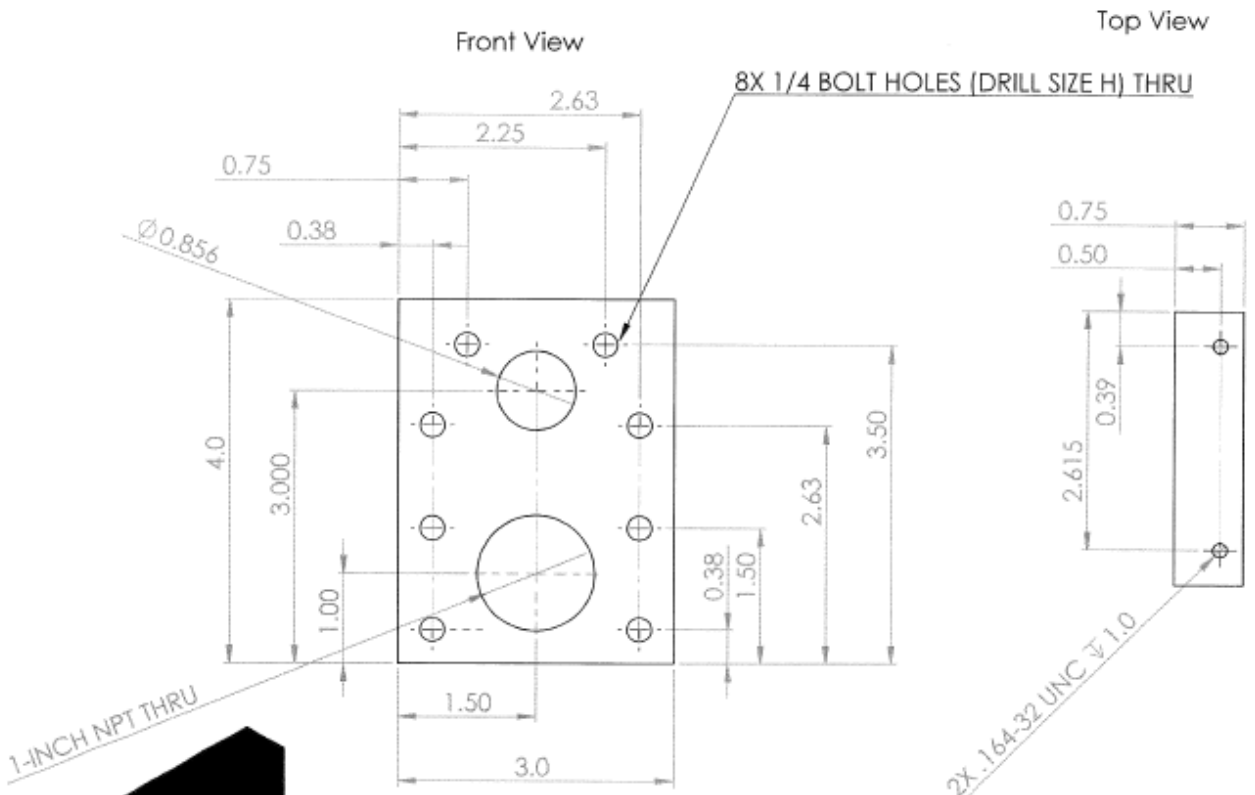

SCALE: 2:3
MATERIAL: ALUMINUM

K-LANL Transfer_ SWITCHER HOUSING FRONT PLATE
Michael D. Yoho 910 476-3087
mdyoho@utexas.edu

ITEM: 6 PAGE 1 OF 2

K-LANL TRANSFER_SWITCHER HOUSING BODY
DRAWN BY: J.FUCHS, 409.739.3358
JANET.FUCHS@UTEXAS.EDU

SCALE 1:2
MATERIAL: ALUMINUM 6061

TOP VIEW

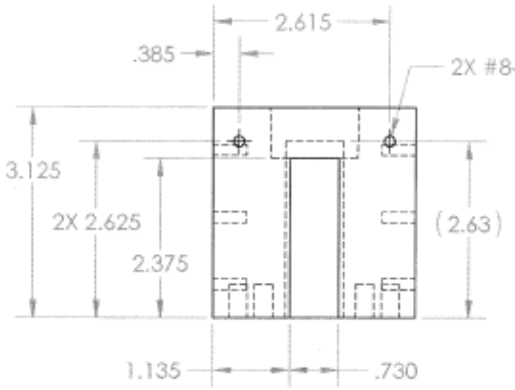

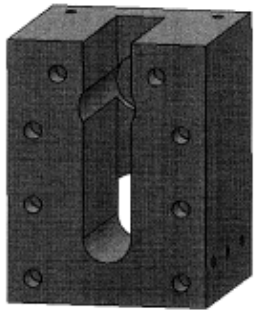

FRONT VIEW

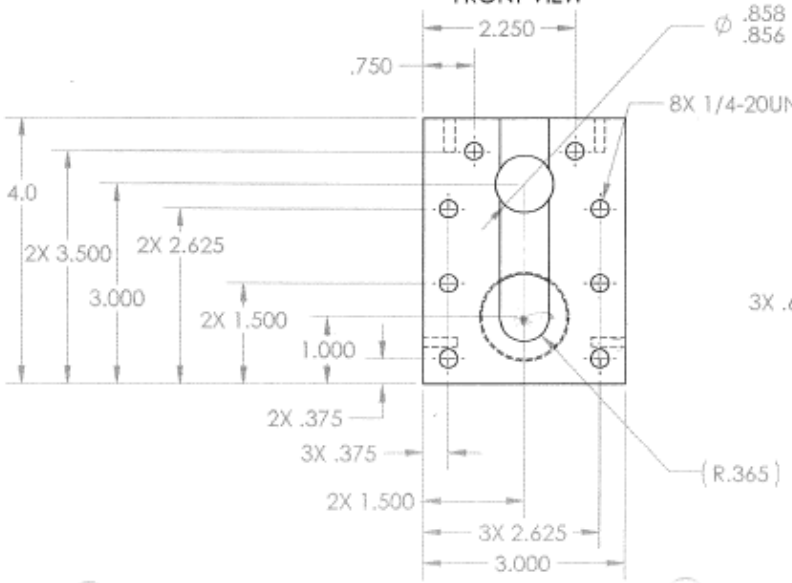

RIGHT SIDE VIEW

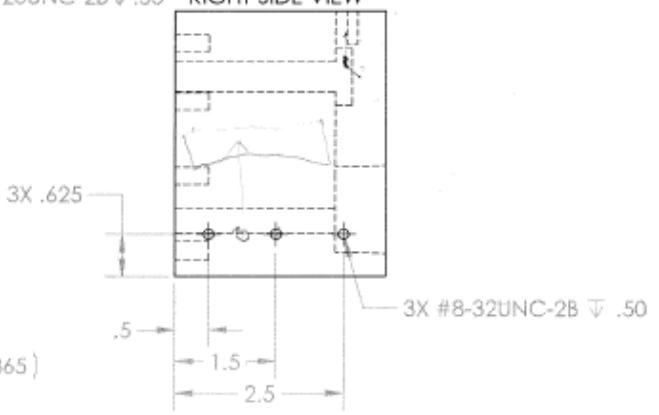

PAGE 2 OF 2

ITEM: 6

REAR ISOMETRIC VIEW

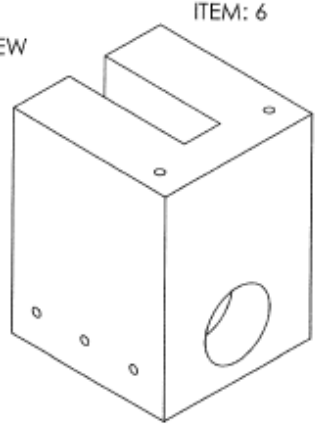

LEFT SIDE VIEW

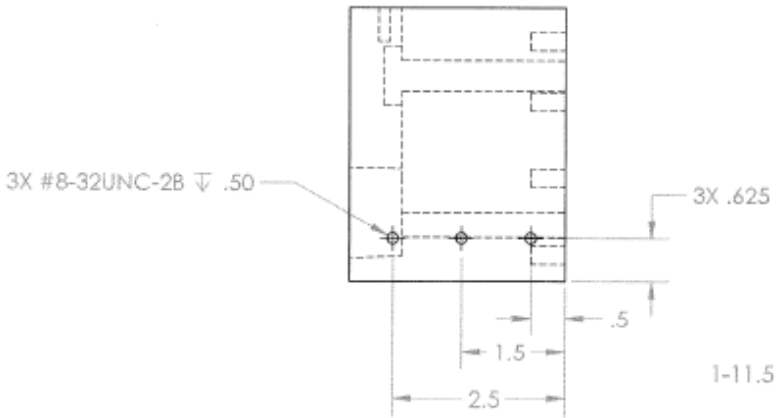

BACK VIEW

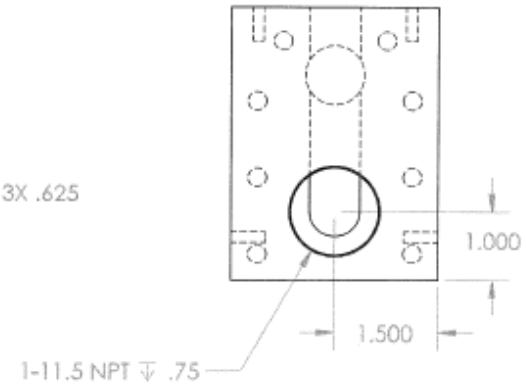

FRONT VIEW

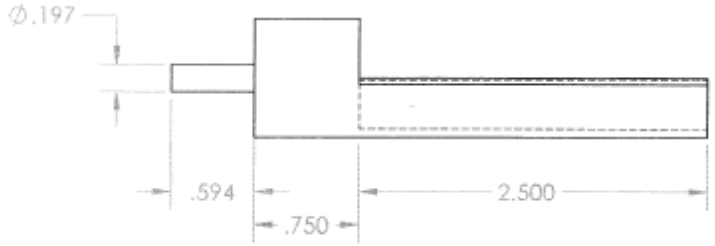

RIGHT SIDE VIEW

ITEM: 4

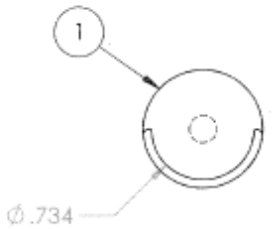

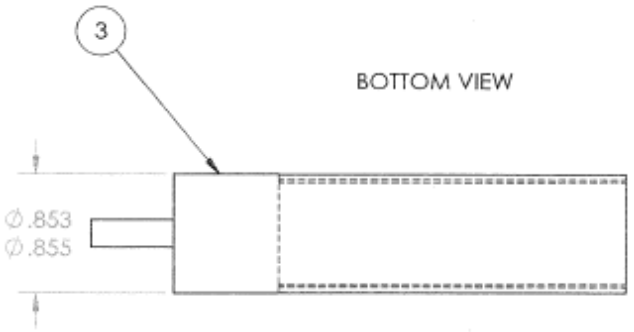

BOTTOM VIEW

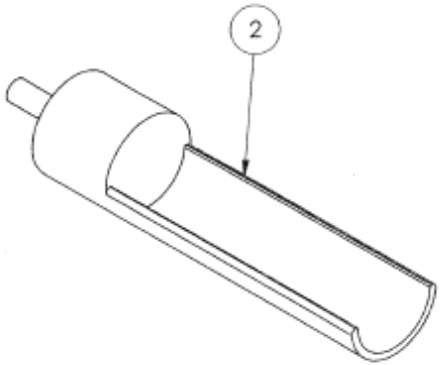

1. EDGES ROUNDED TO MACHINE CAPABILITY
2. CUT TO BE 180 DEGREES TO CREATE SEMI-CIRCLE
3. SWITCHER TO ASSEMBLE INSIDE SWITCHER HOUSING, REFER TO LOADING ASSEMBLY DIAGRAM

SCALE 1:1
MATERIAL: BRASS

K-LANL TRANSFER_SWITCHER
DRAWN BY: MICHAEL YOHO
910 476-3087
mdyoho@utexas.edu

DIVERTER

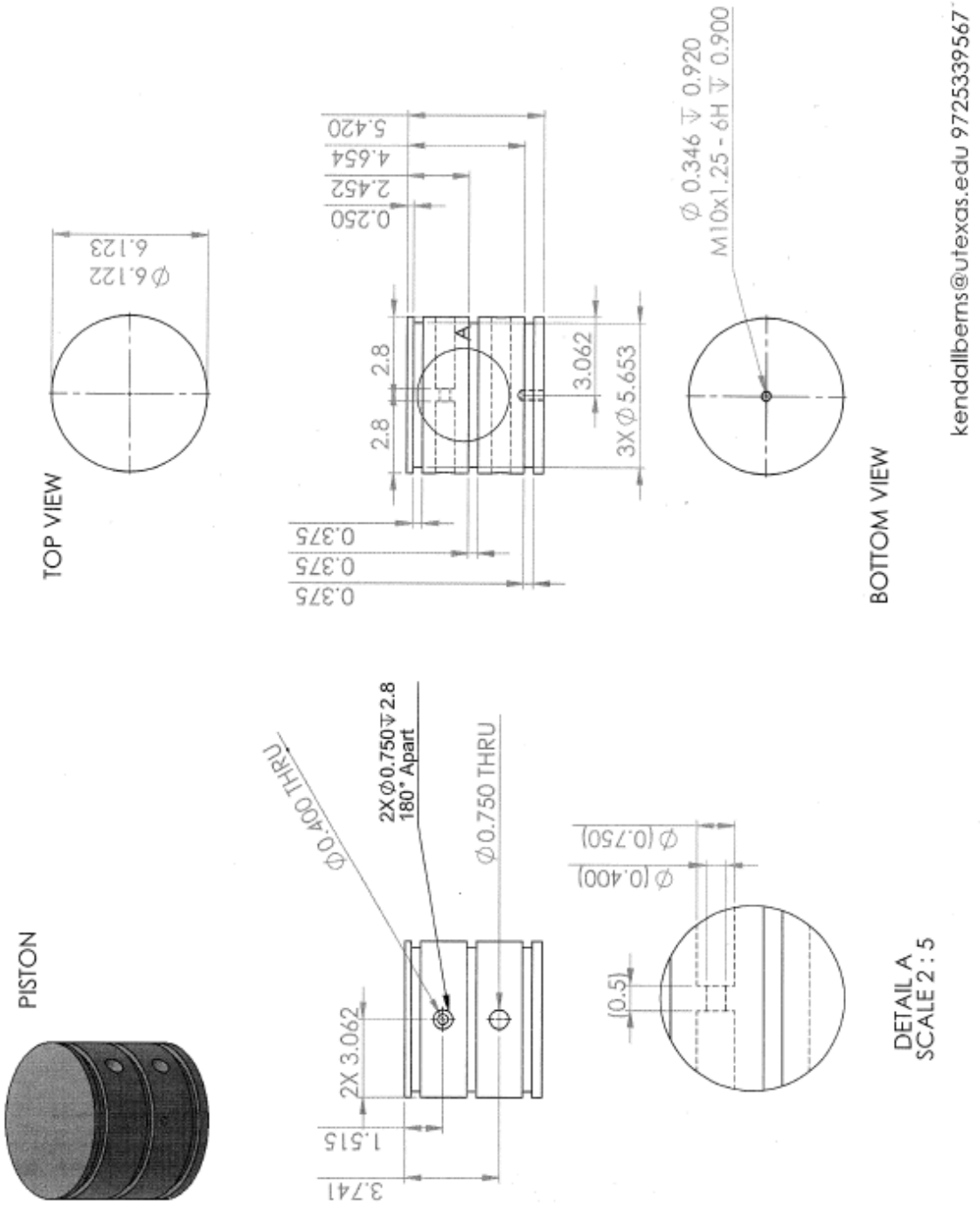
PISTON
TOP VIEW
Ø6.122
6.123
0.375
0.375
0.375
2.8
2.8
A
3.062
3X Ø5.653
0.250
2.452
4.654
5.420
Ø 0.346 ∓ 0.920
M10x1.25 - 6H ∓ 0.900
BOTTOM VIEW
kendallberns@utexas.edu 9725339567
2X Ø0.750∓2.8
180° Apart
Ø0.400 THRU
Ø0.750 THRU
2X 3.062
1.515
3.741
Ø (0.400)
Ø (0.750)
(0.5)
DETAIL A
SCALE 2 : 5

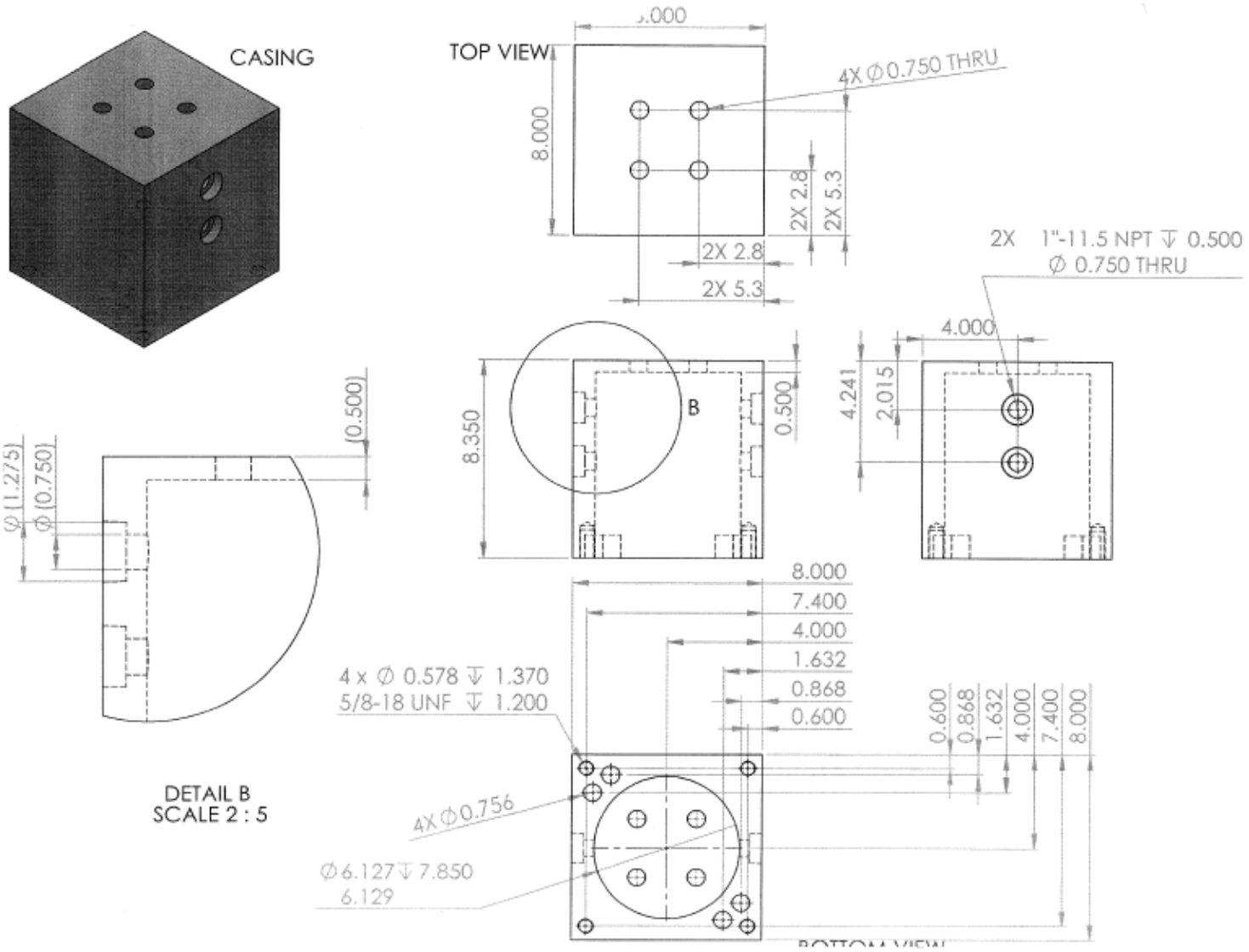
CASING
TOP VIEW
4X ∅0.750 THRU
8.000
2X 2.8
2X 5.3
2X 1"-11.5 NPT ↧ 0.500
∅ 0.750 THRU
4.000
4.241
2.015
8.350
0.500
B
(0.500)
∅(1.275)
∅(0.750)
8.000
7.400
4.000
1.632
0.868
0.600
4 x ∅ 0.578 ↧ 1.370
5/8-18 UNF ↧ 1.200
4X∅0.756
∅6.127↧7.850
6.129
DETAIL B
SCALE 2 : 5

FLANGE 4X

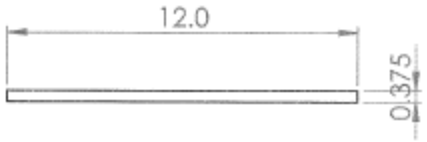

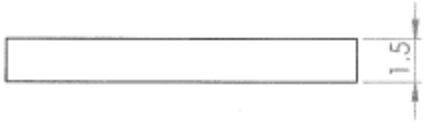

kendallberns@utexas.edu 9725339567

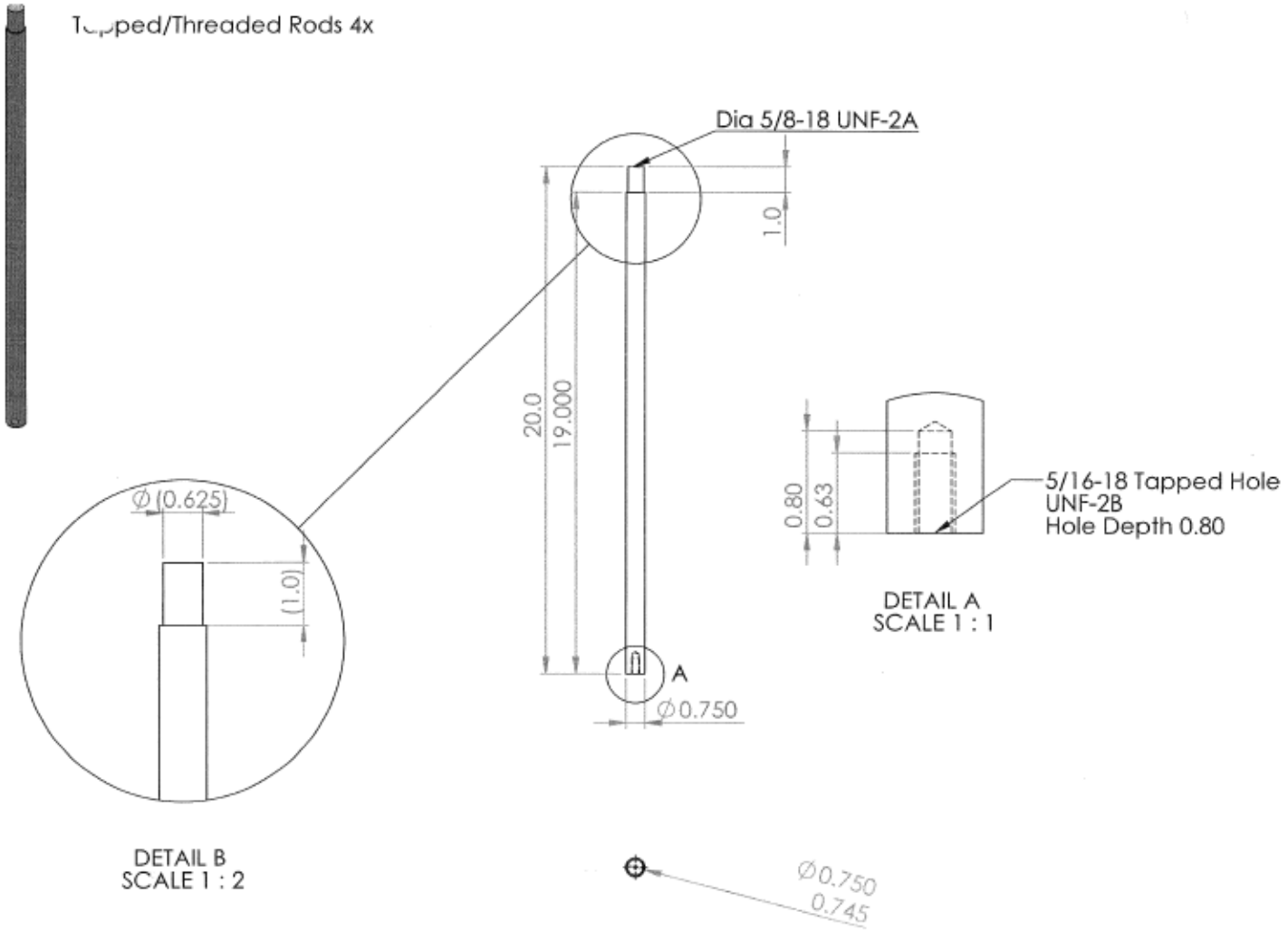

kendallberns@utexas.edu 9725339567

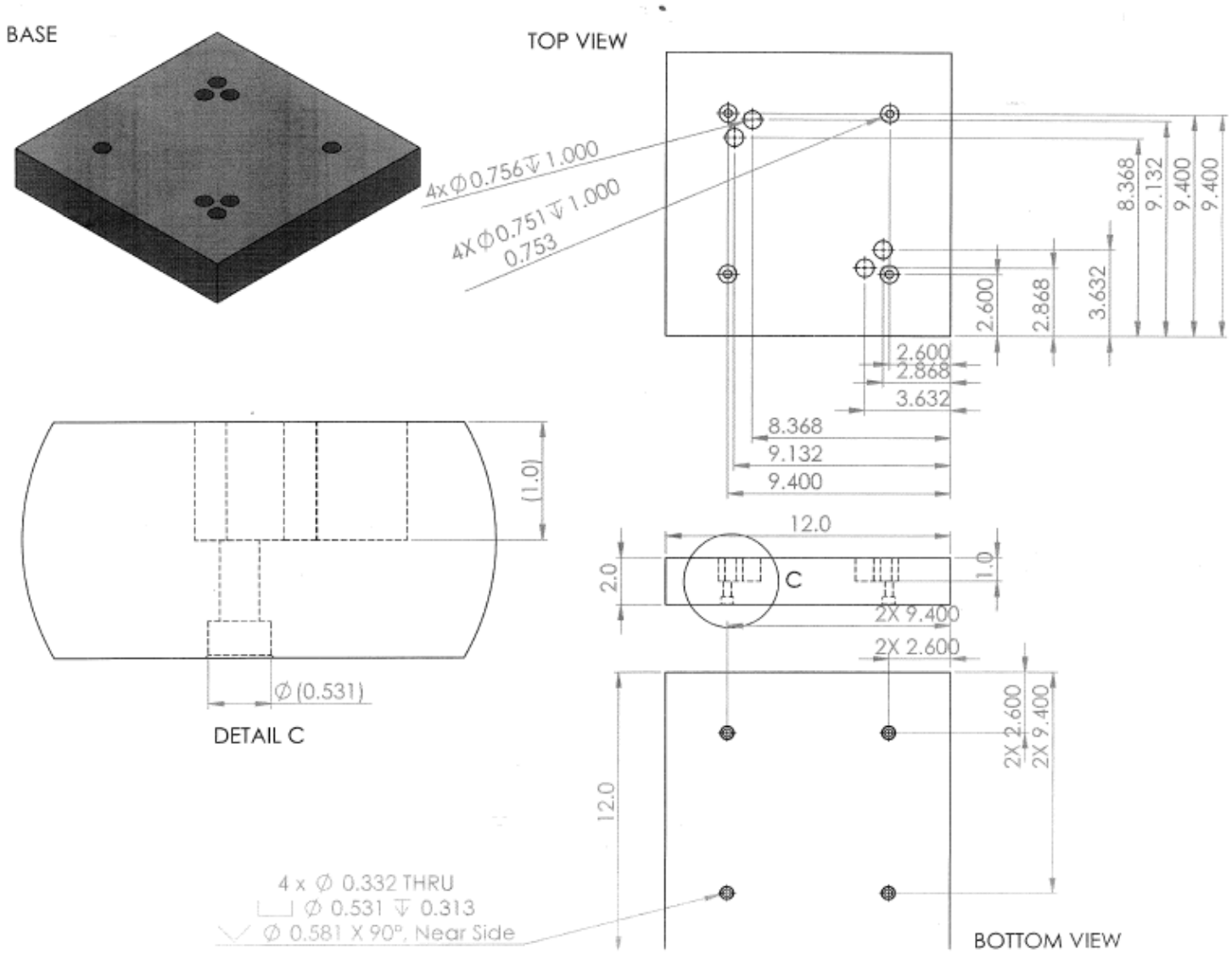
BASE
TOP VIEW
4xØ0.756↧1.000
4XØ0.751↧1.000
0.753
8.368
9.132
9.400
9.400
2.600
2.868
3.632
2.600
2.868
3.632
8.368
9.132
9.400
(1.0)
12.0
2.0
C
1.0
2X 9.400
2X 2.600
2X 2.600
2X 9.400
12.0
Ø (0.531)
DETAIL C
4 x Ø 0.332 THRU
⌴ Ø 0.531 ↧ 0.313
⌵ Ø 0.581 X 90°, Near Side
BOTTOM VIEW

Appendix C: Neutron Flux Characterization Scoping ORIGEN2.2 Input

The following is the raw input used with ORIGEN2.2 (as "tape5.inp"). The decay library & cross-section database would be concatenated into one file ('"tape9.inp"). Note the material specification being done within the input deck rather than a separate deck. This input deck takes 100g of elemental aluminum, irradiates it at a flux of 2×10^5 $ncm^{-2}s^{-1}$, allows it to decay for two minutes, and then punches the output for both the immediate & two-minute of decay depletion vectors.

```
-1
-1
-1
CUT -1
RDA Irradiation of a single foil for scoping.
RDA Change the elemental composition after END
RDA to reflect isotopic abundances of a foil.
RDA Currently, punches out the vector of activation
RDA products of a mass of elemental aluminum
RDA normalized to 100g.
RDA Utilizes a Fast XS set (AMORUUUR) & O2_Fast.exe.
LIP 0 0 0
RDA        DECAY LIB    XSECT LIB       VAR. XSECT
LIB 0        1 2 3       321 322 323      9 50 0 1    4
PHO 0 0 0 10
OPTL 6*8 7 19*8 7 8
OPTA 28*8
RDA OPTF 6*8 7 19*8 7 8
OPTF 28*8
INP -1 1 -1 -1 1 1
MOV -1 1 0 1.0
BUP
IRF 60 2E5 1 2 2 2
RDA allow for two minutes of decay
DEC 62 2 3 2 0
BUP
OUT 2 1 -1 0
OUT 3 1 -1 0
END
1 130270 100.0 0 0.0 0 0.0
0
```

Appendix D: NJOY99 ENDF Processing Input

Below is a sample NJOY99 input deck used to process the ENDF-B/VII.1 file for ^{24}Mg. The latest version of the time of this writing (NJOY99.362) was used by created by"UPD.EXE" with LANL's latest source corrections. Only three modules (RECONR, BROADR, and GROUPR) are used in order to convert the ^{24}Mg ENDF tape to a PENDF file, Doppler-broaden the (n,p) cross-section set to 25C (298K), and then recollapse the cross-section set to a group structure of 5 – 10 MeV, 10 – 12 MeV, and 12 – 14 MeV.

```
reconr
 20 22
 'pendf tape for MG-24 from endf/bvii'/
 1225 2/
 .005/
 'MG-24 n_1225_12-Mg-24.dat endf/bvii'/
 'processed by the njoy nuclear data processing system'/
 0/
 broadr
 20 22 23
 1225 1/
 .005/
 298
 0/
 groupr
 20 23 0 24
 1225 1 0 4 6 1 1 1 /
 'MG-24'/
 298
 1.e10
 3/
 5E6 10E6 12E6 14E6/
 .10 .025 820.3E3 1.4E6/
 3 103 'User-Requested MT 103'/
 0/
 0/
 stop
```

References

[1] England, T.R. and Rider, B.F. “Evaluation and Compilation of Fission Product Yields”. LA-UR-94-3106, ENDF-349. October, 1994.

[2] “Evaluated Nuclear Data File (ENDF)”. Hosted Online by the International Atomic Energy Agency. Current as of March 2014. Last Accessed April 23, 2014. < https://www-nds.iaea.org/exfor/endf.htm>

[3] ENDF-B/VII.1 ^{235}U Independent & Cumulative Fission Yield Data, stored in MT 8, MF 454 of file “nfpy_9228_92-U-235.dat”. Hosted Online by the International Atomic Energy Agency. Last Accessed April 23, 2014.
< https://www-nds.iaea.org/public/download-endf/ENDF-B-VII.1/nfpy/>

[4] “JEFF-3.2 evaluated data library – Neutron data”. Hosted Online by the Nuclear Energy Agency. Current as of February 28, 2014. Last Accessed April 23, 2014.
< http://www.oecd-nea.org/dbforms/data/eva/evatapes/jeff_32/>

[5] “JENDL: Japanese Evaluated Nuclear Data Library”. Hosted Online by the Japanese Atomic Energy Agency. Current as of September 10, 2013. Last Accessed April 23, 2014. < http://wwwndc.jaea.go.jp/jendl/jendl.html>

[6] Krane, Kenneth S. “Introductory Nuclear Physics”. John Wiley & Sons, Inc, Canada, 1988.

[7] Schneider, Erich. Lecture #1. Nuclear Reactor Theory. University of Texas, Austin, TX. January 14, 2014.

[8] Takahashi, A., Ohta, M., and Mizuno, T. “Production of Stable Isotopes by Selective Channel Photofission of Pd”. Jpn. J. Appl. Phys. Vol. 40 (2001). pp. 7031-7046. Part I, No. 12, December 2001.

[9] “Compilation and evaluation of fission yield nuclear data: Final report of a co-ordinated research project, 1991-1996.” IAEA-TECDOC-1168. International Atomic Agency, December 2000.

[10] “Thermo Scientific MP 320 Neutron Generator”. Thermo Scientific Product and Description Page Hosted Online. Last Accessed April 23, 2014.
< http://www.thermoscientific.com/en/product/mp-320-neutron-generators.html>

[11] “MP320 User Guide Rev 1.1”. Thermo Electron Corporation Proprietary & Confidential Information, April 18. 2005.

[12] “Neutron Generators Overview”. Thermo Scientific, 2006. Last Accessed April 23, 2014. <http://www.qsl.net/k/k0ff/7Manuals/Fusor/Thermo%20Scientific%20-%20Neutron%20Generators%20Overview.htm>

[13] Berns, K., Fuchs, J., Guidry, J., and Yoho, M. “Automatic Transfer System for Neutron Irradiation Test Bed”. Final Report Submitted to Dr. Sheldon Landsberger for Completion of Mechanical Engineering Design Project, Spring 2012.

[14] “SmartMotor SM17205D, Specification and Drawings”. Hosted Online by Moog Animatics, 2014. Last accessed April 23, 2014.

<http://www.animatics.com/products/smartmotor/animatics/nema-17-1700-series/sm17205d.html>
[15] "Serial Communication – Basic Serial Write and Read". Hosted Online by National Instruments. Current as of September 6, 2006. Last Accessed April 23, 2014.
< http://www.ni.com/example/27669/en/>
[16] "ETH Cylinders: High Force Electric Actuators". Product Catalog, Parker Hannafin Corporation, 2014. Last Accessed April 23, 2014.
<https://www.exoticautomation.com/exotic_pdfs/cat/Parker/EM/Parker%20-%20ETH%20Catalog.pdf>
[17] "SmartMotor SM23165D". Hosted Online by Moog Animatics. Inc. Last Accessed April 23, 2014.
< http://www.animatics.com/download/smartmotor/spec-sm23165d_cds.pdf>
[18] "C5 Series Stainless Steel Photoelectric Sensors". Hosted Online by Automation Direct. Last Accessed April 23, 2014.
< http://www.automationdirect.com/static/specs/pe5mmc5.pdf>
[19] "Banjo Liquid Handling Products". Banjo Corporation Product Specification Manual. Hosted Online by Cross Equipment LMC. Last Accessed April 23, 2014.
< http://www.crossequipmentlmc.com/banjo.pdf>
[20] "NTE R14 Series Relay Specifications". Hosted Online by NTE, Inc. Last Accessed April 23, 2014. < http://www.nteinc.com/relay_web/pdf/R14.pdf>
[21] "Ortec DSPEC Pro User's Manual". Hosted Online by Ortec, Inc. Last Accessed April 23, 2014.
< http://www.ortec-online.com/download/DSPEC-PRO-MNL.pdf>
[22] Simpson, R. "Introductory Electronics for Scientists and Engineers". Second Edition. Addison-Wesley, June 8, 1987.
[23] "Texas Instruments SN74LS76A Dual J-K Flip-Flops with Preset and Clear". Hosted Online by the University of California at Davis. Current as of March 1988. Last Accessed April 23, 2014.
< http://www.ece.ucdavis.edu/~bbaas/180a/Datasheets/sn74ls76.pdf>
[24] "Texas Instruments SN74LS04 Hex Inverster". Hosted Online by Texas Instruments. Current as of January 2004. Last Accessed April 23, 2014.
< http://www.ti.com/lit/ds/symlink/sn74ls04.pdf>
[25] "Texas Instruments SN74LS08 Quadruple 2-Input Positive-And Gates". Current as of March 1988. Last Accessed April 23, 2014.
< http://www.ti.com/lit/ds/symlink/sn74ls08.pdf>
[26] Travis, J. and Kring, J. "LabView for Everyone: Graphical Programming Made Easy and Fun". Third Edition. Prentice-Hall, 2007.
[27] "User Guide and Specifications NI USB-6509". Hosted Online by National Instruments. Last Accessed April 23, 2014.
< http://www.ni.com/pdf/manuals/372136a.pdf>

[28] Knoll, G.F. “Radiation Detection and Measurement”. Fourth Edition. John Wiley & Sons, 2010.
[29] Golub, G.H. and Van Loan, C.F. “Matrix Computations”. Fourth Edition. John Hopkins University Press, 2013.
[30] Croff, A.G. “ORIGEN2—A revised and Updated Version of the Oak Ridge Isotope Generation and Depletion Code”. ORNL-5621, Oak Ridge National Laboratory. July 1980.
[31] Croff, A.G. “A User’s Manual for the ORIGEN2 Computer Code”. ORNL/TM-7175, Oak Ridge National Laboratory. July 1980.
[32] “Korea Atomic Energy Research Institute Table of Nuclides”. Last Accessed April 23, 2014. < http://atom.kaeri.re.kr/>
[33] MacFarlane, R.E. and Kahler, A.C. “Methods for Processing ENDF/B-VII with NJOY”. LA-UR-10-04652, Los Alamos National Laboratory. July 2010.
[34] MacFarlane, R.E. “Understanding NJOY”. Lectures given at the Workshop on Nuclear Data and Nuclear Reactors: Physics, Design, and Safety. Trieste, March 13 – April 14, 2000. Accessed online on April 23, 2014.
< http://users.ictp.it/~pub_off/lectures/lns005/Number_1/MacFarlane_2.pdf>
[35] “MAESTRO-32 MCA Emulator for Microsoft Windows 2000 Professional and XP Professional A65-B32 Software User’s Manual”. Hosted Online by the Massachusetts Institute of Technology. Last Accessed April 23, 2014.
<http://web.mit.edu/8.13/8.13d/manuals/Ortec-MAESTRO-software-manual.pdf>
[36] “MATLAB Documentation Center: lsqnonneg”. Hosted Online by Mathworks, Inc. Last Accessed April 23, 2014.
< http://www.mathworks.com/help/matlab/ref/lsqnonneg.html>
[37] “NUDAT 2.6”. Hosted Online by the Brookhaven National Laboratory. Last Accessed April 23, 2014. < http://www.nndc.bnl.gov/nudat2/>